

Enhanced Hydrogen Dipole Physisorption

Final Report

For work performed in collaboration with the EERE Fuel Cell Technologies Program
Hydrogen Sorption Center of Excellence under award #DE-FC36-05GO15079

- by the -

California Institute of Technology

Technical POC: Dr. Channing Ahn

MS 138-78

1200 E. California Blvd

Pasadena, CA 90025

Tel.: (626) 395-2174 Fax: (626) 795-6132

e-mail: cca@caltech.edu

Introduction/Background

Mission/Scope

California Institute of Technology (Ahn)

A serious obstacle to realizing a hydrogen-based energy economy is compact storage¹. The problem is even more apparent for applications as a mobility fuel where volumetric energy density is of utmost importance. Numerous approaches for compact storage of hydrogen have been investigated. As a pure substance, hydrogen can be contained as a gas or liquid (solidifying hydrogen is not considered a realistic storage approach). A secondary material, while adding mass to the system, can also be used to increase the volumetric density of hydrogen. Some metal hydrides reversibly store large amounts of hydrogen, chemically bound (*absorbed*) within their crystal structure, but generally suffer from poor kinetics and practicality is only achieved at elevated temperatures. Light-element hydrides such as LiBH_4 contain among the highest gravimetric capacities of known materials, but hydrogen sorption is not fully reversible except under extreme conditions, and there are many complications to safety and practicality. There are many technologies being explored in these categories of storage materials and others such as complex hydrides. Hydrogen can also be effectively stored by *adsorption* on the surface of a material. For example, carbonaceous (i.e., predominantly carbon) sorbent materials are particularly attractive because they are lightweight, abundantly available, simple to produce, and can effectively increase the volumetric density of stored gases. Another possible class of materials for adsorptive hydrogen storage is coordination polymers, also known as metal-organic frameworks (MOFs), which can achieve extremely high surface area and contain exposed metal sites which act as preferential adsorption sites at low pressure.

A main challenge for carbon (and other) adsorbent materials is that room temperature reversible hydrogen storage capacities are generally too low for effective use in mobile vehicle applications. Total system gravimetric capacities are better for pure compression than adsorptive compression except at very low temperatures; hydrogen adsorption at 77 K is a more promising solution, but requires significant additional system complexity to maintain such a low temperature. As compression containers achieve high strength to weight ratios, pure compression is favored over adsorption, but compaction of the adsorbent is a potential avenue favoring adsorption and could impart significant improvement to volumetric capacities. The complications associated with cryogenic containment temperatures and thermal management are also under assessment, but appear to be acceptable compared to other storage solutions. High pressure hydrogen delivery is currently available to the public, for example from 35 to 70 MPa, favoring pure compression storage as well as physisorption over other solutions.

The hydrogen gas adsorption effort at Caltech was designed to probe and apply our understanding of known interactions between molecular hydrogen and adsorbent surfaces as part of a materials development effort to enable room temperature storage of hydrogen at nominal pressure. While these gas solid interactions have a long history that date back to before the time of the French chemist Lavoisier, with a concomitant expanse of literature on gas adsorption phenomena, far less clear at the beginning of this project was our ability to

¹ S. Satyapal, J. Petrovic, C. Read, G. Thomas, and G. Ordaz, The U.S. Department of Energy's National Hydrogen Storage Project: progress towards meeting hydrogen-powered vehicle requirements, *Catal Today* **120** (3–4), 246–256 (2007).

take advantage of this understanding and to engineer or alter, surface structures that would have site potentials suitable for enhancing hydrogen interaction.

Although physisorption has been recognized and used for over two centuries, the basis for our understanding has arisen for the most part from marginally understood, activated carbons, which contain a number of macroscopic and microscopic features that vary considerably, depending on the source of the carbon and the processing used to produce the high surface areas that provide the large number of adsorption sites that are necessary for physisorption. As a result, it has been necessary to invoke a combination of phenomenological and theoretical models to account for isotherm behavior in these morphologically mixed systems.

The physisorption process originates with the electron correlation energy, often depicted as rearrangements of charge distribution that occur in quantum mechanical fluctuations and is a weak interaction requiring cryogenic temperatures and/or high pressures. A more classical explanation is often provided, where induced dipole-dipole interactions are used to account for van der Waals bonding. Physisorption relies on van der Waals forces that arise from surface potentials of the adsorbent in order to yield an interaction with the ad-atom/molecule. The potential well associated with the interaction of a specific surface site has been described from the viewpoint of both kinetic and statistical mechanical approaches and can be expressed either as a macroscopic thermodynamic quantity, the adsorption enthalpy, or as a chemical potential (which expresses the free energy on a per molecule basis). The work we have performed over the past five years has been tailored to address the outstanding issues associated with weak hydrogen sorbent interactions in order to find an adequate solution for storage tank technology.

R&D

Approach:

Ideally, an adsorbent should have i) a large surface area so that as many hydrogen molecules can be accommodated on the surface as possible, ii) a large micropore volume in order to maximize the volumetric density, and iii) a constant isosteric enthalpy of adsorption in order to simplify the engineering requirements for a tank based on such a sorbent.

The necessity of criteria i) and ii), large surface area and large micropore volume can be appreciated by noting the early work of Chahine and Bose² as shown in Figure 1. Here we see that the mass percentage uptake of hydrogen in a number of activated carbons is highly correlated to each of these properties. We can best understand this by considering the geometric factors that should be considered with hydrogen adsorbents in relation to the size of molecular hydrogen. Relative to the sub-angstrom dimensions of hydrogen in atomic form, molecular hydrogen is large, with a kinetic diameter measured at about 2.9 Å² but with a size as determined by molecular sieve experiments of about 3.6 Å (or an actual prolate spheroid geometry of 3.44 to 3.85 Å)³. We can compare this value to the closest near-neighbor distance as measured by neutron scattering of molecular hydrogen adsorbed

² Chahine, R.; Bose, T. K. "Characterization and optimization of adsorbents for hydrogen storage," In 11th WHEC, 1996; Pergamon Press: Oxford, U.K., 1996; p 1259.

³ Koresh, J.; Soffer, A, Study of Molecular-Sieve Carbons .2. Estimation of Cross-Sectional Diameters of Non-Spherical Molecules, J. Chem. Soc-Faraday Transactions I Volume: 76 pp. 2472-2485 DOI: 10.1039/f19807602472 Part 12 (1980).

onto graphite, with a 3.51-Å distance⁴. We note also that solid hydrogen (*P63/mmc* structure) has a lattice parameter $a = 3.76$ Å and $c = 6.14$ Å⁵. Under the conditions where we expect normal dispersion forces to apply, the possibility of multilayer adsorption under the temperature and pressure regimes of interest will not result in conditions under which hydrogen would liquefy and a monolayer of hydrogen adsorbed onto a surface will represent, under most conditions, the maximum quantity of hydrogen that can be expected from the standpoint of gas adsorption phenomena. We can therefore apply simple geometric means in probing the upper limits of uptake that can be expected based on a simple surface packing density model⁶. We show this in Figure 2.

An estimate of the graphene SSA is obtained from the fact that a single hexagon contains a net total of two carbon atoms with an area of $1.5 \sqrt{3}a^2$. This gives an SSA of 2630 m²/gm when both surfaces of graphene are taken into account. Two possible configurations for a hydrogen monolayer on a graphene surface are illustrated in Figure 2. Commensurate structures as shown on the left side of Figure 2 are presumably energetically favorable since the hydrogen molecules sit in the hexagon centers, but this configuration naturally results in a lower gravimetric density than a close-packed, incommensurate structure, depicted on the right side of Figure 2. Provided both sides of a graphene surface are occupied, then the gravimetric density is about 5 wt% for the commensurate $\sqrt{3} \times \sqrt{3}$ R30° structure. The gravimetric density of a close-packed H₂ monolayer can be obtained by using the standard method of estimating the BET cross-sectional area (although we should note that standard BET analysis that uses N₂ with an effective diameter of 4.5 Å may underestimate slightly the surface area accessible to H₂).

For a hexagonal close-packed structure, the cross-sectional area of a hydrogen molecule is given by

$$\sigma = f \left(\frac{M}{\rho N_a} \right)^{2/3} \quad \text{Equation 1}$$

where the HCP packing factor f is 1.091, ρ is the density of liquid hydrogen, M is the molar mass, and N_a is Avogadro's number. Taking the liquid H₂ density as $\rho = 77.03$ kg m³, the cross-sectional area is $\sigma = 0.124$ nm². If the carbon SSA is $\alpha(\text{SSA})$, then the hydrogen monolayer adsorption in weight percentage is

$$\text{wt\%} = \left(\frac{\alpha(\text{SSA})}{\sigma} \right) \left(\frac{M}{N_a} \right) \times 100 \quad \text{Equation 2}$$

Using a similar hard sphere model approach, we can also gauge the overall volumetric density limits that a gas adsorption approach to storage can reach. This is shown in Figure 3 where we have assumed an a-a stacking sequence of a graphitic structure. We have not taken into account an actual van der Waals distance in this model but expect this to add ~ 3 Å to the inter-graphitic layer spacing. In recognition of the maximum density limitations imposed by these simple geometric models, the approach we adopted for the initial part of our research effort was to synthesize and evaluate high surface area materials. From then

⁴ M. Nielsen, J. P. McTague (*) and W. Ellenson (**), "Adsorbed Layers of D₂, H₂, O₂, and ³He on Graphite Studied by Neutron Scattering," *J. Physique Coll. C4, suppl.* 10, 38, 1977, C4-10

⁵ Landolt, H. (Hans), 1831-1910 "Electronic structure of solids, photoemission spectra and related data," T.C. Chiang [et al.] ; editors, A. Goldmann, E.-E. Koch, Berlin ; New York : Springer-Verlag, c1989.

⁶ S. D. M. Brown, G. Dresselhaus, and M. S. Dresselhaus, "Reversible hydrogen uptake in carbon-based materials," *Mater Res Soc Symp P* **497**, 157-163 (1998).

we considered materials that had idealized pore dimensions that might, at least within the actual pores, maximize the hydrogen packing density.

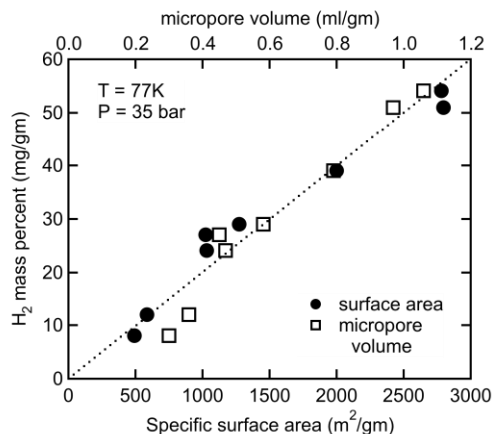
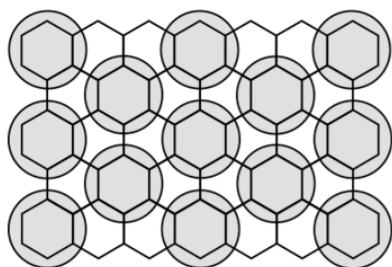


Figure 1. Mass percentage uptake as a function of surface area (bottom axis) and micropore volume (upper axis). (Data reproduced from R. Chahine and T. K. Bose²).

Commensurate $\sqrt{3} \times \sqrt{3}$ R30° structure



Configuration of solid H₂ on graphite

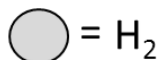
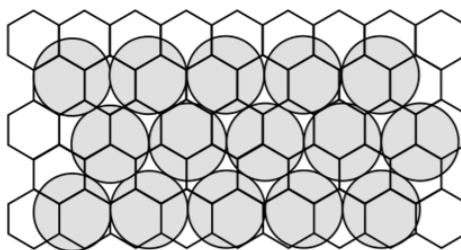


Figure 2. Two possible structures for a hydrogen monolayer on a graphene sheet. The diameters as depicted here for hydrogen molecules (shaded circles) are 3.51 Å and, for the incommensurate depiction on the right, 3.74 Å.

Double layer of H₂, x-z cross-section

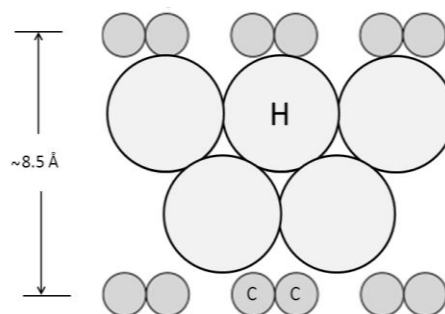


Figure 3. At right, schematic of hydrogen stacking required in graphite as an analog to adsorption on both surfaces of a grapheme sheet. No consideration of van der Waals distances is taken into account in this depiction.

Criterion iii), an adsorbent with a constant isosteric heat has been given little attention and itself still requires a level of understanding and development that is still an issue to this day. Ambient temperature operation of adsorbents will require a high

enthalpy. Unfortunately, many papers in the literature use a single quantity to describe the adsorption enthalpy. However, this single quantity or Henry's law⁷ value typically only applies to the initial molecule adsorbed onto a surface and is formally referred to as the *differential enthalpy of adsorption at zero coverage*. This is to be distinguished from the change of enthalpy as a function of coverage or pressure, known as the *isosteric enthalpy of adsorption*. This nomenclature provides an important distinction as the sorption enthalpy will typically decrease due to surface site heterogeneities and sorbate-sorbate interactions. From an engineering standpoint, a decreasing isosteric enthalpy of adsorption presents a number of complications from an engineering standpoint as a storage tank needs to be designed for the entire range of isosteric enthalpy values, a value that for many carbon-based materials is typically on the order of 4-5 kJ/mole H₂ necessitating the use of cryogenic temperatures (typically 77K) for effective high density storage. If such a material has a Henry's Law or low loading enthalpy of 14 kJ/mole that decreases to 4-5 kJ/mole, a tank designed around such a system would require increasing the storage tank temperature from the cryogenic base temperature, in order to maximize the quantity of useable hydrogen based on an adsorbent tank. Depending on the extent to which the isosteric enthalpy decreases, a storage tank based on such a material would be more complex from a tank engineering standpoint, given the additional heating requirements, than that of a tank based on a material with a low constant isosteric heat (that might only require insulation). On the other hand, a high constant isosteric heat enables storage tank operation at relatively high temperatures compared to 77 K.

All of the materials development and analysis work at Caltech was accomplished using standard synthesis and analytical procedures for adsorbents. The uptake measurements were accomplished using a 3rd generation volumetric Sieverts apparatus. Data collected from our Sieverts apparatus enabled us to determine the maximum value of the surface excess adsorption, but also to assess the thermodynamic parameters required for an engineering tank design, to see if improved material properties could be achieved.

What is being measured?

While the earlier discussion provides some basic geometric parameters laying the groundwork on the nature of adsorption as it pertains to surface area and to an extent, micropore volume, the empirical data collected from an experiment is not straightforward in the case of high pressure hydrogen adsorption. In fact this area of research has tested the limits of empirical work in a way that offers some clarity to the early work of Gibbs. Because of the overall misunderstanding on the part of many experimentalists, theoreticians and some equipment manufacturers as to the meaning of the experimental data that is collected from a volumetric experiment, we will now devote some discussion to this topic as virtually all of the data in the rest of this report requires an appreciation of the quantity that is actually measured. The true empirically determined quantity that is measured in any experiment is the Gibbs surface excess, which differs from textbook treatments that consider absolute absorption onto the surface. The difference in the two quantities arises due to the uncertainty of the adsorption layer that may also consist of a gas law component. A boundary layer needs to be considered and this construct is defined as the Gibbs dividing surface⁸. Several simplified treatments that reduce the original general multicomponent treatment of Gibbs to a single-component gas can be found in the

⁷ F. Rouquerol, J. Rouquerol, and K. S. W. Sing, "Adsorption by Powders and Porous Solids: Principles, Methodology, and Applications," (Academic Press, San Diego, CA, 1999).

⁸ O. Talu and A. L. Myers, Molecular simulation of adsorption: Gibbs dividing surface and comparison with experiment, *AIChE J* **47** (5), 1160–1168 (2001).

literature⁹. The surface excess can be depicted schematically as shown in **Figure 4**. Near the adsorbent surface, in the region labeled “adsorbed layer”, the local adsorptive density is considerably higher than in the bulk gas phase. It is assumed that at a suitably large distance from the adsorbent surface, the adsorptive density decays back to a constant bulk density (ρ_{bulk}). This region is labeled as the “bulk gas”. Important quantities for the adsorption model are defined in Table 1.

The standard practice is to express adsorption as a Gibbs surface excess quantity. This is the amount of adsorptive which is present in the adsorbed layer in excess of the bulk gas density, indicated in **Figure 4** by the dark gray region. Conveniently, the surface excess amount is the quantity which is measured in a standard volumetric measurement. The expression for the Gibbs surface excess amount is therefore

$$n^{\sigma} = n^{*} - \rho_{\text{bulk}} V_a \quad \text{Equation 3}$$

The surface excess amount n is an extensive quantity. Typically, however, data are presented as a specific surface excess amount

$$n = n^{\sigma} / m_s \quad \text{Equation 4}$$

where m_s is the sorbent mass.

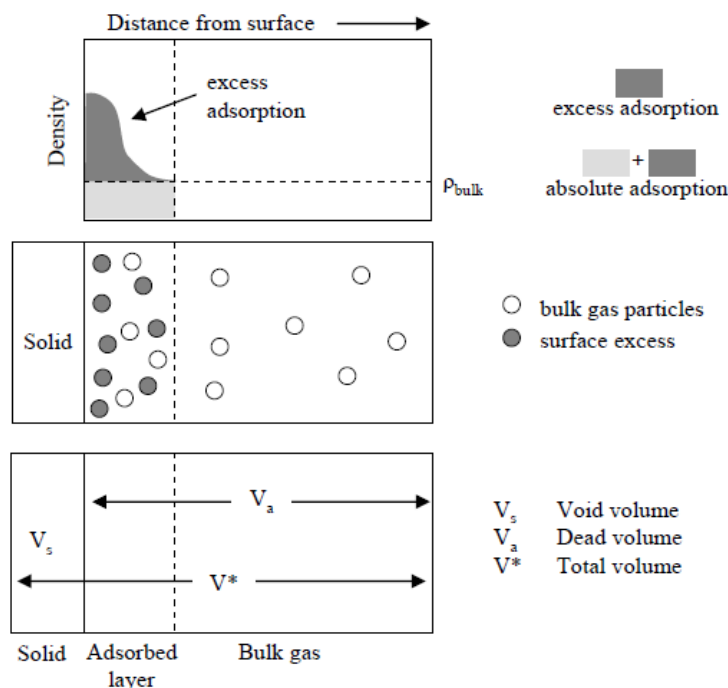


Figure 4. Illustration of surface excess adsorption and absolute adsorption. (Top) Density profile of the adsorptive gas as a function of distance from the adsorbent surface. Dark gray areas denote the adsorbed molecules, whereas light gray areas represent bulk gas amounts which are not counted towards adsorption in the surface excess scheme. (Middle) Illustration of the concept of bulk and adsorbed molecules. (Bottom) Important volumes of the adsorption.

⁹ S. Sircar, Gibbsian surface excess for gas adsorption—revisited, *Ind Eng Chem Res* **38** (10), 3670–3682 (1999).

Table 1. Important definitions for adsorption

Symbol	Description
n^*	The total amount of adsorptive in the system (both adsorbed and bulk)
V^*	The total volume of the system (including the volume occupied by the adsorbent). Determined by calibrating the instrument.
V_s	The “void volume.” This is the volume of the solid which is impenetrable for the adsorptive gas. It is typically measured by helium pycnometry.
m_s	Mass of the adsorbent.
V_a	The “dead volume.” It is the difference between the total system volume and the void volume, $V_a = V^* - V_s$.

$$n^\sigma = n^* - \rho_{\text{bulk}} V_a \quad \text{Equation 5}$$

The surface excess amount n^σ is an extensive quantity. Typically, however, data are presented as a specific surface excess amount

$$n = n^\sigma / m_s \quad \text{Equation 6}$$

where m_s is the sorbent mass.

Sieverts apparatus description

Having developed a description of the quantities that are measured, we now move to a discussion of the equipment used to take these measurements. At Caltech, we have an extensive amount of experience performing volumetric hydrogen uptake measurements and view our expertise in this area as a crucial aspect of the work performed through the HSCoE. Hydrogen adsorption data were collected with a custom-built, manually-operated Sieverts instrument¹⁰. This instrument is based on several previous designs. While the instrument is custom-built and information about it is not readily available, the principle of operation is generally similar to that of other instruments of this type as well as to that of commercially available instruments. We will however, offer here a detailed description as modifications to the design were modified somewhat from our earlier work.

The operating limits for the instrument are 100 bar and 600 °C. A schematic drawing of the Sieverts apparatus is shown in **Figure 5**. The instrument is equipped with both a high-resolution manometer (MKS-120, Baratron capacitance gauge, rated to 25,000 Torr maximum pressure) and a wide-range manometer (MKS-833, Baratron capacitance gauge, 3000 psi max). Note that while we generally use SI units, we will designate English units when the original instrument specifications were called out in that way. Temperature is monitored in a number of places on this system using platinum resistance thermometers (PRT) bonded to the exterior of the steel tubing. The vacuum system consists of a high-vacuum molecular drag pump (Alcatel MDP 5011) connected to an oil-free diaphragm backing pump (KNF, Model N880.3 AN22 E). Vacuum pressure is monitored with a cold cathode vacuum gauge. Base pressure is typically around 10^{-7} Torr. The instrument

¹⁰ Bowman, R. C., Jr.; Luo, C. H.; Ahn, C. C.; Witham, C. K.; Fultz, B. *J. Alloys Compd.* **1995**, 217, 185.

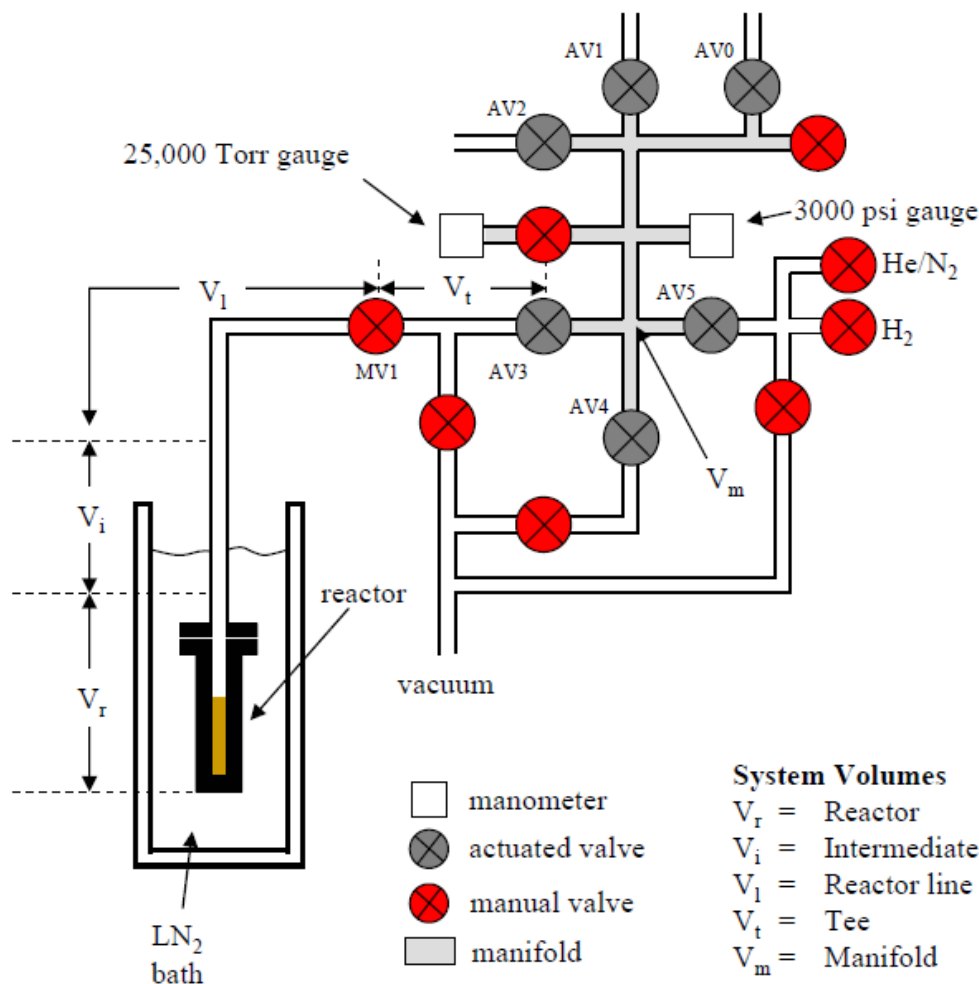


Figure 5. Sieverts apparatus with the valve and volume configuration denoted.

contains manual (DL-type) and air-actuated (HB-type) stainless steel Swagelok valves. All tubing and fittings are made from electro-polished 316L stainless steel. Leak-tight Swagelok VCR® fittings are used for connections between tubing and valves. The only exception is the reactor fitting, which uses a Conflat flange copper gasket (1.33 in.). To prevent fine powders from being sucked into the manifold, a 2 micron filter gasket assembly was designed to be seated in the reactor and secured by an internal retaining c-ring. All components are welded, except for valves and sensors. The accuracy of the high-resolution MKS120 manometer is approximately 0.08% of the readout, and was used with the factory calibration. The pressure gauges can exhibit hysteresis, particularly following high-pressure measurements. Therefore the zero point pressure is typically reset prior to each experiment. Research-grade H_2 (99.98 %) was used for all measurements, in conjunction with an in-line filter assembly (Millipore Corp., Inert II Reactive Micro Matrix). For air-sensitive samples, the entire reactor assembly can be brought into a glovebox and then sealed with valve MV1 after sample loading.

The volumetric method

Measurements are collected using an extremely simple volumetric method. As pictured in Fig. 5, the reactor volume is kept at a constant temperature using a liquid N_2 bath (77 K), a

liquid Ar bath (87 K) or a dry ice bath (195 K). An intermediate temperature region (V_i) is assumed to have a constant temperature gradient between the bath temperature and room temperature, and is assigned an average value of $T_{\text{int}} = (T_{\text{bath}} + T_{\text{room}}) = 2$. The remainder of the instrument volume remains at ambient room temperature, which is measured by a PRT bonded to the exterior of the manifold region. Hydrogen is first introduced into the manifold volume V_m by opening and then closing valve AV5. The gas is then expanded into the tee volume, V_t , by opening valve AV3. The pressure can be fine-tuned by opening valve AV4 and adjusting a manual needle valve which connects to the vacuum system. The initial pressure and manifold temperature are then recorded (p_1, T_{room}). Hydrogen is finally expanded into the reactor volume $V_i + V_t + V_r$ by opening manual valve MV1. After allowing the adsorption system to reach equilibration (typically 15 min), the final pressure and manifold temperature are recorded (p_2, T_{room}). Assuming negligible fluctuation during the course of the experiment, it is typically acceptable to use an average value of the room temperature. Gas densities, $\rho(p, T)$, are determined from the measured pressure and temperature using the NIST Reference Fluid Thermodynamics and Transport Properties (RefProp) database¹¹. The initial and final amounts of non-adsorbed, bulk hydrogen are given by

$$n_i = \rho(p_1, T_{\text{room}})[V_m + V_t] \quad \text{Equation 7}$$

$$n_f = \rho(p_2, T_{\text{room}})[V_m + V_t + V_i] + \rho(p_2, T_{\text{bath}})[V_r - V_{\text{sample}}] \quad \text{Equation 8}$$

where V_{sample} refers to the void volume displaced by the sample. The surface excess adsorption is simply given by the decrease in the mass of bulk hydrogen, $n^{\sigma} = n_i - n_f$. This procedure measures the excess adsorption that occurs with a single dose of hydrogen. To collect a complete isotherm, this step is performed repeatedly at incrementally higher pressures. In the incremental method the hydrogen is not desorbed between isotherm points. This results in considerable time savings, but can also lead to incrementally increasing errors if the measurements are not done carefully. At the end of an adsorption series we can begin a desorption series by essentially running the same procedure in reverse. With MV1 closed, the manifold + tee volume is opened to vacuum until a specific pressure is reached. Then MV1 is opened, the system is allowed to equilibrate, and the final pressure is recorded.

Errors in volumetric adsorption measurements

The volumetric method is a standard method for measuring gas adsorption and is very simple to implement. However, if adsorption measurements are collected in a cumulative fashion without desorbing between each point, errors in the data can accumulate linearly. Therefore it is important to identify all the major sources of error in a volumetric adsorption measurement.

For example, uncertainty in the void volume of the sample can lead to large errors in the measured hydrogen adsorption, particularly for low-density materials. The standard method we use to determine the void volume of the sample is to expand helium into the reactor (loaded with sample) at room temperature, essentially performing He pycnometry. We assume that the helium is not adsorbed and that the micropores impenetrable to helium

¹¹ E. W. Lemmon, M. L. Huber, and M. O. McLinden, 'NIST standard reference database 23: reference fluid thermodynamic and transport properties – REFPROP', Number Version 8.0 in Standard Reference Data Program (2007).

are also impenetrable to hydrogen. The accuracy of the helium volume technique on our Sieverts instrument was tested by measuring a non-porous aluminum blank of known dimension. Helium was expanded into the reactor from nine different initial pressures between 1000 Torr and 9000 Torr, and measurements were simultaneously recorded using both the 25,000 Torr gauge and the 3000 psi gauge. There was considerably more variation in the measurements made by the lower resolution 3000 psi gauge. Based on its physical dimensions, the volume of the aluminum spacer was 0.99 ml. This compares to the 1.01(2) ml obtained with the high-resolution gauge and 0.9(2) ml obtained with the lower resolution gauge. For many carbon adsorbents we find that it is sufficient to use a generic *skeletal density* of 2.1 g/ml (roughly the mass divided by the void volume) to calculate the void volume based on the sample mass. In cases where H₂ uptake amounts are large, we can use this approximation.

If single-point measurements are collected for long time periods (i.e., several hours), then daily fluctuations in the ambient temperature can affect the data in several ways. First, the hydrogen density in the manifold can change slightly, which can be significant at high pressures. Second, the signals from the capacitance pressure gauges themselves change with temperature. Leaks within the system can also cause problem for measurements that involve either long collection times or small adsorption amounts. To test these temperature effects, the instrument volume was filled with H₂ and all system temperatures logged and pressures measured for up to 80 hours. At 50 bar pressure, there were no detectable leaks in the system, and the pressure was well-correlated with the ambient temperature. There did appear to be a leak at 80 bar pressure, in which the pressure dropped substantially without any correlation with the ambient temperature. Therefore leaks can indeed be a major source of error on this instrument at high pressures. None of the adsorption measurements presented in this particular instrument exceed 50 bar pressure.

A useful way to determine the accuracy of the Sieverts instrument is to collect a hydrogen adsorption isotherm with an empty reactor. If the reactor is at 298 K, there should be no real adsorption. Any measured adsorption is due to experimental errors. If the reactor is at 77 K or 87 K, there may be a small amount of adsorption on the reactor walls or in the filter gasket mesh, but any substantial measured adsorption is indicative of cumulative error. We have performed numerous empty reactor measurements at the standard sample temperatures. An illustration of the effect of empty reactor adsorption is presented in Figure 6. In this case the total H₂ adsorption by the sample (a Cr₂O₃ aerogel) was very small, on the order of the empty reactor adsorption itself. To determine the true adsorption by the sample, the background adsorption by the empty reactor needs to be subtracted. Hysteresis is present for the empty reactor adsorption and desorption runs, so they need to be fit to separate linear equations. The corrected sample adsorption and desorption is obtained once the reactor background has been subtracted.

Nomenclature conventions

We introduced earlier the convention for defining heats of adsorption. We note that in this work we will use the Department of Energy (DOE) convention of expressing gravimetric uptake. This is an issue as the recent literature on hydrogen adsorption has resulted in some ambiguity over the description of the quantities that are measured. This is due in part to the use of technical targets established by the DOE¹² that are expressed in

¹² S. Satyapal, J. Petrovic, C. Read, G. Thomas, and G. Ordaz, The U.S. Department of Energy's National Hydrogen Storage Project: progress towards meeting hydrogen-powered vehicle requirements, *Catal Today* **120** (3–4), 246–256 (2007).

percentages that are different from the values that are measured in the traditional literature on gas adsorption¹³.

In this work, we will generally use weight percentages as opposed to mass fractions (with typical units of milligrams/gram or moles/gram). Ambiguity has arisen due to the use of “weight percentage” as a figure of merit. The traditional literature on adsorption generally expresses the quantity of adsorbed gas as

$$\frac{m_{\text{gas}}}{m_{\text{sorbent}}} \quad \text{Equation 9}$$

where m_{gas} is the surface excess value of the mass of adsorbed gas per mass of sorbent m_{sorbent} . We denote this quantity as the mass fraction. We understand weight percentage (wt%) as

$$\frac{m_{\text{gas}}}{m_{\text{sorbent}} + m_{\text{gas}}} \quad \text{Equation 10}$$

As noted earlier, the quantity of adsorbed gas is expressed as the “surface excess” value as originally denoted by Gibbs¹⁴, and that is the only quantity that is determined empirically either gravimetrically or volumetrically. Simply put, the surface excess is the quantity of gas that the surface adsorbs beyond the quantity that the real gas law would normally indicate exists at the surface. This quantity is distinguished from “absolute” adsorption as initially envisioned by Langmuir¹⁵ (and which is the quantity that is generally expressed in the computational/model-based literature) and is the net amount of gas adsorbed onto a surface. We elaborate on the difference between the two below.

Experimental procedures

Real Gas Adsorption Measurements

To characterize a potential hydrogen storage material, we must measure the amount of hydrogen it adsorbs at various temperatures and pressures. The adsorption amount is typically measured as a function of pressure while the temperature is held constant. These isothermal pressure-composition curves are called isotherms. Two important quantities can be derived from the isotherm: (a) the maximum surface excess adsorption capacity, and (b) the isosteric heat of adsorption. The heat of adsorption is particularly significant as an indicator of the interaction strength between the hydrogen molecules and the adsorbent.

Isosteric heat of adsorption

A complete thermodynamic theory can be developed for a surface excess phase in equilibrium with a bulk gas phase, and a brief summary is provided here. The surface excess layer can be considered as a distinct phase, with a thermodynamic state that is completely characterized by an area A , a spreading pressure Π , and a surface excess concentration $\Gamma = n^\sigma / A$. The differential energy of adsorption is the change in internal energy of the entire adsorption system upon the addition of an infinitesimal surface excess amount dn^σ . In principle this can be measured directly by calorimetry. A more useful quantity is the differential enthalpy of adsorption ($\Delta h_{T,\Gamma}$), which can be measured indirectly

¹³ K. S. W. Sing, D. H. Everett, R. A. W. Haul, L. Moscou, R. A. Pierotti, J. Rouquerol, and T. Siemieniowska, Reporting physisorption data for gas solid systems with special reference to the determination of surface-area and porosity (recommendations 1984), *Pure Appl Chem* **57** (4), 603–619 (1985).

¹⁴ J. W. Gibbs, *The Scientific Papers of J. Willard Gibbs: In Two Volumes* (Ox Bow Press, Woodbridge, CT, 1993).

¹⁵ I. Langmuir, The adsorption of gases on plane surfaces of glass, mica and platinum, *J Am Chem Soc* **40**, 1361–1403 (1918).

by the isosteric method. From the equilibrium condition between the surface excess phase and the bulk gas phase (i.e., $\mu^\sigma = \mu^g$), the following expression can be derived,

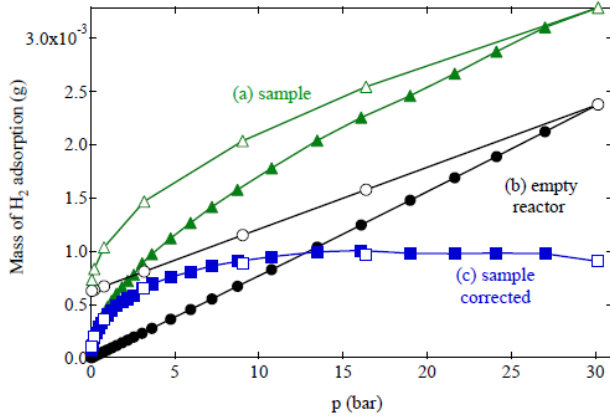


Figure 6. Illustration of the effect of empty reactor adsorption. (a) Hydrogen adsorption by reactor containing a sample (Cr_2O_3 aerogel). (b) Adsorption by the empty reactor. (c) Corrected sample adsorption after subtracting the empty reactor background. Sample temperature was 77 K and pressure was measured on the high-resolution gauge. Solid symbols are adsorption points and open symbols are desorption points. Total H_2 adsorption amount is presented rather than the specific adsorption amount.

$$\ln\left(\frac{p}{p_0}\right) = \frac{u_{T,\Gamma}^\sigma - u_T^g - RT}{RT} - \frac{s_{T,\Gamma}^\sigma - s_T^{g,0}}{R}$$

$$= \frac{\Delta h_{T,\Gamma}}{RT} - \frac{\Delta s_{T,\Gamma}}{R}$$

Equation 11

where the differential enthalpy and entropy of adsorption are implicitly defined. The term $s_T^{g,0}$ is the standard molar entropy of the ideal gas at the standard pressure $p^0 = 1$ bar. The quantity u_T^g is the internal energy of an ideal gas particle, and $u_{T,\Gamma}^\sigma$ is the differential surface excess internal energy (i.e., the derivative of the total surface excess internal energy with respect to n^σ).

We would now like to calculate the differential enthalpy of adsorption from the experimental quantities n^σ , p , and T . This is done using the isosteric method where a series of isotherms are measured at different temperatures. Differentiating Equation 11 with respect to temperature while holding Γ constant and assuming that $\Delta h_{T,\Gamma}$ and $\Delta s_{T,\Gamma}$ are not dependent on temperature, then

$$\left(\frac{\partial}{\partial T} \ln[p]\right)_\Gamma = -\frac{\Delta h_{T,\Gamma}}{RT^2}$$

Equation 12

and we obtain

$$\Delta h_{T,\Gamma} = R \left(\frac{\partial \ln[p]}{\partial (1/T)}\right)_\Gamma$$

Equation 13

where p is the pressure corresponding to the surface excess concentration. When Equation 13 is used to determine the differential enthalpy, at least two isotherms need to be measured at different temperatures which are not too far apart (a separation of 10 K is good). The quantity obtained by this method is sometimes called the *isosteric heat*, to indicate that it has been determined by the isosteric method.

Experimental isotherms are not measured at perfectly spaced n intervals. Therefore it is necessary to either fit the isotherm to some function, or to interpolate the appropriate n from the isotherm data points. Because the isosteric method is very sensitive to errors in the equilibrium pressure, interpolation can sometimes introduce significant artifacts into the calculated isosteric heat. Our standard approach is to fit the 77 and 87 K isotherms individually to an empirical function, $n = f(p)$. The isosteric heat can now be estimated from the inverse of the fitting function Equation 13 which is,

$$\begin{aligned} &\approx \left(\frac{\ln[f_{77}^{-1}(n)] - \ln[f_{87}^{-1}(n)]}{(77 \text{ K})^{-1} - (87 \text{ K})^{-1}} \right) \times (8.314 \text{ J mol}^{-1} \text{ K}^{-1}) \\ &= \ln \left[\frac{f_{77}^{-1}(n)}{f_{87}^{-1}(n)} \right] \times (5.57 \text{ kJ mol}^{-1}) \end{aligned} \quad \text{Equation 14}$$

The units of the fitting function cancel out in the last expression as long as they are used consistently. One problem with this method is that it is often difficult to fit the experimental isotherms in the low pressure region. This is especially true for the steep isotherms that are typical of microporous adsorbents. An example of the problems with fits to empirical equations at low pressures is illustrated in Figure 7. The 77 K and 87 K hydrogen adsorption isotherms collected on an activated carbon (CNS-201) were individually fitted to the Hill equation¹⁶. The isosteric heat was calculated from the fits (using Equation 14). It is clear that there is an artificial drop in the isosteric heat as n approaches zero.

Our initial work found that a better method for calculating isosteric heats is to fit all the hydrogen adsorption isotherms to a single model-independent virial-type thermal equation¹⁷. This equation is given by

$$\ln p = \frac{1}{T} \sum_{i=0}^l a_i n^i + \sum_{i=0}^m b_i n^i + \ln n \quad \text{Equation 15}$$

Eq. 11 is fit simultaneously to the 77, 87, and 195 K data. Fitting parameters $\{a_i, b_i\}$ are temperature independent, and the sum limits l and m are increased until a sufficient goodness-of-fit is reached. The isosteric heat can be easily calculated from Eq. 11 by taking the derivative with respect to T ,

$$\Delta h_{T,\Gamma} = R \left(\frac{\partial \ln[p]}{\partial (1/T)} \right)_{\Gamma} = -R \sum_{i=0}^l a_i n^i \quad \text{Equation 16}$$

In the zero-coverage limit the enthalpy equals $\Delta h_{T,G} = -R(a_0)$. An example of the model independent virial equation for the same CNS-201 sample is displayed in **Figure 8**. The adsorption data is presented in terms of $\ln(p/n)$ versus n and is fit simultaneously to the virial-type thermal equation. Values of $l = m = 5$ were sufficient for the fit. The isosteric heat now has the correct shape in the low pressure region, without the artificial drop obtained from the individual fits to the empirical Equation 14. All of the isosteric heats

¹⁶ The Hill equation utilized here is actually equivalent to the Langmuir equation. It is given by $f(p) = n_{\max} = [1 + (a/p)^r]^{-1}$, where r sets rate at which the function grows, and a sets the p -value at which the function is at half-maximum.

¹⁷ L. Czepirski and J. Jagiello, "Virial-type thermal equation of gas-solid adsorption," Chem. Eng. Sci., 44:797-801, 1989.

presented in this thesis were calculated using the model-independent virial equation method, unless otherwise specified.

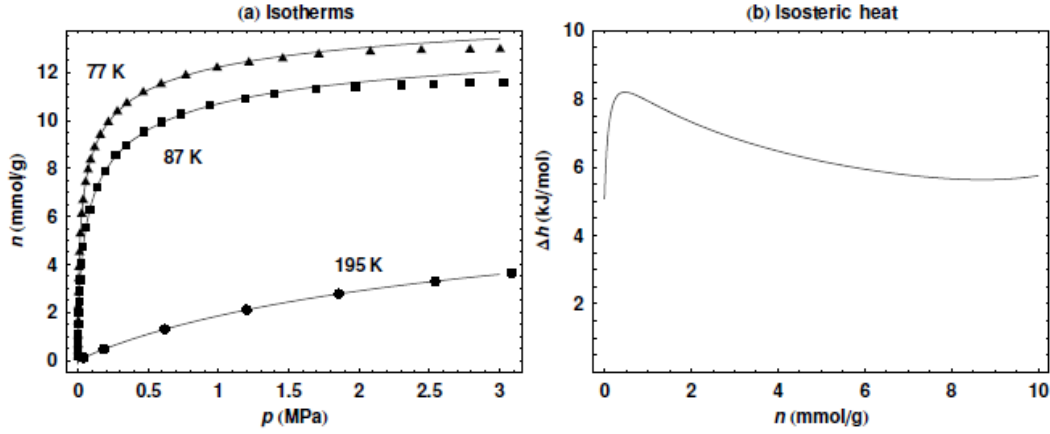


Figure 7. Isosteric heat derived from empirical functions fitted independently to each isotherm. (Left) Hydrogen adsorption isotherms of activated carbon CNS-201, each fitted to a Hill equation. (Right) Isosteric heat calculated from the fits (using Equation 14).

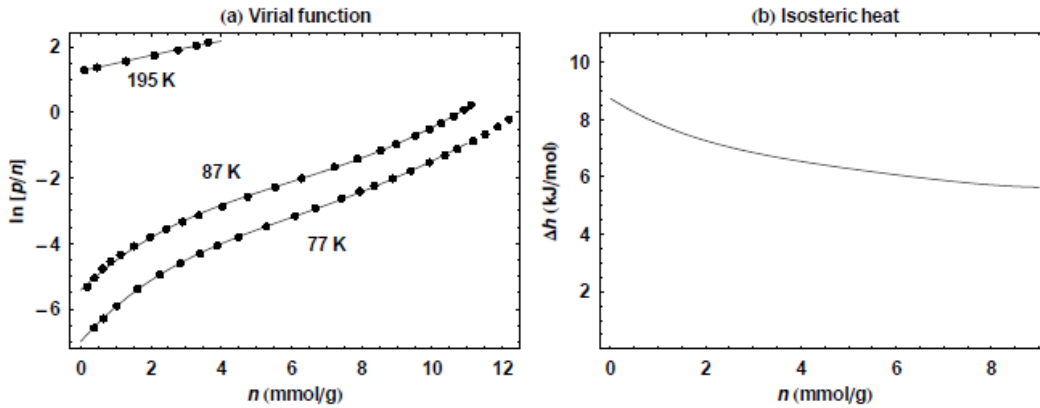


Figure 8. (a) Hydrogen adsorption isotherms of CNS-201 fitted to a single model-independent virial equation given by Equation 15. The data is plotted as $\ln [p/n]$ versus n . (b) Isosteric heat calculated from Equation 16.

Henry's law

In the low pressure region, surface excess adsorption is proportional to the equilibrium pressure (Henry's law). This is basically a consequence of the dilute adsorbed phase behaving like a two dimensional ideal gas. The relation is given by

$$n = k_h p \quad \text{Equation 17}$$

Where k_h is known as the Henry's Law constant. To calculate Henry's law constants, adsorption in the low-pressure region can be accurately modeled by a virial-type equation to take into account small deviations from linearity.

$$\ln(n/p) = K_0 + K_1 n + K_2 n^2 + \dots \quad \text{Equation 18}$$

Since $k_H = \lim_{n \rightarrow 0}(n/p)$, the Henry's law constant can be obtained from the zero-order virial coefficient $K_0 = \ln(k_H)$. By carefully measuring adsorption amounts in the low-pressure region using a high resolution gauge, we can therefore obtain accurate Henry's law constants at 77 K, 87 K, 195 K, and 298 K. An example for the CNS-201 sample is provided in Fig. 3.4. The y-intercepts of the fitted lines are used to calculate the Henry's law constant at each temperature. The differential enthalpy of adsorption in the limit of zero coverage (Δh_0) can be calculated from the van't Hoff equation

$$\Delta h_0 = R \left(\frac{\partial \ln[k_H]}{\partial (1/T)} \right)_n \quad \text{Equation 19}$$

Therefore, the zero coverage enthalpy is simply equal to the slope of the line in **Figure 9b** multiplied by the ideal gas constant $R = 8.314 \text{ J mol}^{-1} \text{ K}^{-1}$. What makes the zero coverage enthalpy so interesting is that it represents the pure sorbent-hydrogen interaction with little contribution from the hydrogen-hydrogen interactions. It can therefore be used to probe systematic trends, for example, in a series of chemically-modified carbon sorbents. However, because of the inaccuracy of low-pressure measurements the Henry's law analysis needs to be done carefully.

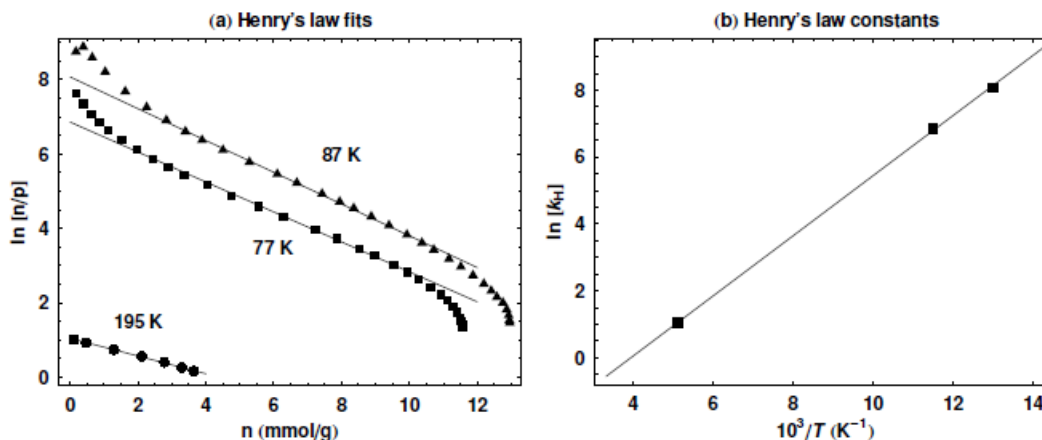


Figure 9. Differential enthalpy of adsorption in the zero-coverage limit calculated from Henry's law. (a) Adsorption isotherm points from CNS-201 presented in the $\ln[n=p]$ versus n format. Henry's law constant for each temperature is equal to y-intercept of the fitted line. (b) Henry's law constants at 77, 87 and 195 K are plotted against $1/T$.

Finally, before continuing with a discussion on our initial work on carbons, we should also make use of the standard convention for defining pore dimensions in high surface area materials. This convention is depicted in Fig. 10. below where micropores are defined as having dimensions below 2 nm, mesopores are in the range of 2 to 50 nm and macropores are greater than 50 nm¹⁸.

¹⁸ K.S.W. Sing, D.H. Everett, R.A.W. Haul, L. Moscou, R.A. Pierotti, J. Rouquerol, T. Siemieniewska, "Reporting Physisorption Data for Gas Solid Systems with Special Reference to the Determination of Surface-Area and Porosity (Recommendations 1984)," Pure and Applied Chemistry, Volume: 57 Issue: 4 Pages: 603-619 DOI: 10.1351/pac198557040603 (1985).

Initial work on carbon aerogels and metal-modified carbon aerogels

At the outset of this program, we recognized that a number of research reports claiming high hydrogen uptake consisted of ambiguous or questionable data. Given the level of

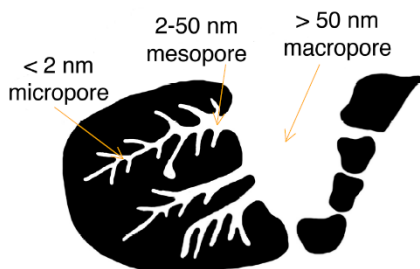


Figure 10. Pore designations by the IUPAC.

analysis that we described above, this is not surprising. We can perhaps attribute the inexperience of investigators involved primarily with synthesis of materials, in performing adsorption measurements at high pressures to the failure to recognize and consider the subtleties of sorption measurements. Unlike the adsorption measurements and analyses of traditional metal hydrides, adsorption measurements themselves require a high level of experience in appreciating the subtleties of possible measurement errors as noted in the previous section. To this end, we initiated a round robin involving several laboratories engaged in adsorption work using two samples for which we alone had surface area data but for which a skeletal density of 2.1 gm/cc could be assumed. The initial results of this round robin (four of the nine labs that we requested data from performed the measurements) are shown in the Figure 11 for both 77 and 298 K. The labs that had submitted data included the NETL in Pittsburgh, HRL Laboratories, Max Planck Institute in Germany and Caltech. The results of the round robin were subsequently submitted to Dr. George Thomas, who at the time was consulting to the DOE. This initial set of results were made part of Caltech's initial Annual Merit Review presentation in 2005 as part of its effort on behalf of what was then known as the Carbon Center of Excellence (subsequently designated the Hydrogen Sorption Center of Excellence).

As noted earlier an important criterion for effective physisorption is a high surface area that exposes a large number of sorption sites to adatom or admolecule interaction¹⁹. Moreover, these sites need to have potential wells that are sufficiently deeper than kT if physisorbents are to operate at engineering temperatures. The dependence of gravimetric density on surface area was noted earlier in the work of Chahine and Bose² who, in their survey of studies of activated carbons, noted that that the amount of surface excess hydrogen adsorbed at 77 K varies linearly with surface area at pressures of ~ 35 bar. We can generally expect a gravimetric density of 1 mass% for every 500 m²/g of surface area in activated carbons, a rule of thumb that has become known as the "Chahine rule". This value in fact corresponds to the adsorption of molecular hydrogen onto the graphitic hexagon structure in the $\sqrt{3}$ structure.

¹⁹ Denbigh, K. *The Principles of Chemical Equilibrium*; Cambridge University Press: Cambridge, U.K., 1971.

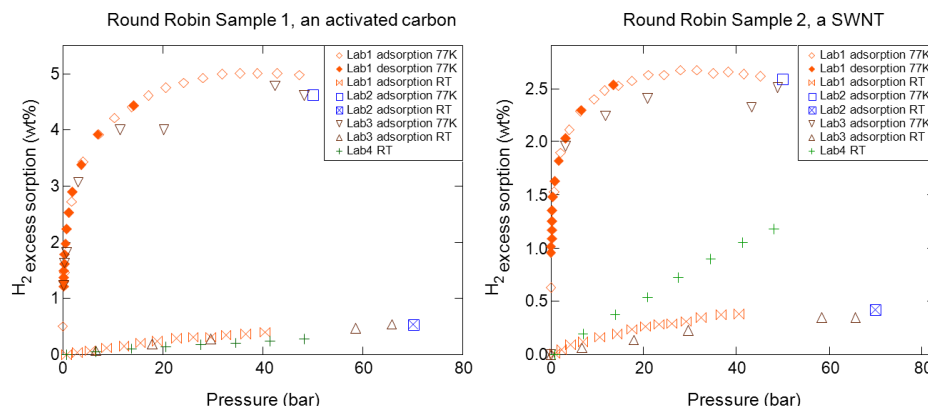


Figure 11. Round robin results from four different laboratories showing 298 and 77 K data for a high surface area activated carbon and for a compacted single walled carbon nanotube sample.

Carbon Aerogels

At our urging, Dr. Theodore Baumann of Lawrence Livermore National Laboratory initiated an effort at synthesizing carbon aerogels with high surface area²⁰. Carbon aerogels (CA's) represent another class of carbons that can serve as effective physisorbents. CA's are mesoporous materials with a range of properties, such as controllable mass densities, continuous porosities, and high surface areas.^{21,22} While mesoporous carbons are not optimized for volumetric density as the pore dimensions are defined to be from 2 to 5 nm and an adsorbent that is optimized for volumetric density would consist of micropores only, the effort at microstructural pore dimension optimization would follow in subsequent synthesis efforts.

The typical physical properties of CA's are derived from the aerogel microstructure which is typically envisioned as a network of interconnected primary particles with characteristic diameters between 3 and 25 nm. Unlike activated carbons, CA's can be prepared in a variety of forms, including monoliths with a high degree of conformability, of possible importance for the incorporation of materials of this type into storage tanks. The hydrogen sorption properties of CAs, however, had not been studied previously. Our understanding of the surface area dependence of sorption behavior in activated carbons motivated us to prepare a range of high-surface-area carbon aerogels in order to understand how sorption behavior in these materials might scale with surface area. As part of this collaboration 77 K isotherm data and sorption enthalpies for activated CAs (ACAs) with BET surface areas up to 3200 m²/g as well as metal-doped CAs were measured. The BET surface area of 3200 m²/g is the highest value that we are aware of for a CA. The CA materials used in this study, both the undoped and metal-doped materials, were synthesized through the sol-gel polymerization of resorcinol with formaldehyde in aqueous solution to produce organic gels that are supercritically dried and subsequently pyrolyzed in an inert atmosphere. The undoped CA's were activated with CO₂ at 950°C.

²⁰ H. Kabbour, T. F. Baumann, J. H. Satcher, Jr., A. Saulnier, and C. C. Ahn, "Toward New Candidates for Hydrogen Storage: High-Surface-Area Carbon Aerogels," *Chem. Mater.*, Vol. 18, No. 26, 2006

²¹ Pekala, R. W. *J. Mater. Sci.* **1989**, 24, 3221.

²² Kong, F. M.; LeMay, J. D.; Hulsey, S. S.; Alvise, C. T.; Pekala, R.W. *J. Mater. Sci.* **1993**, 8, 3100.

Hydrogen adsorption/desorption excess sorption measurements were performed with a volumetric Sieverts apparatus at Caltech. The 77 K adsorption isotherm traces from a low-surface area (330 m²/g) organic aerogel prior to carbonization and from ACA samples with higher surface areas (1460 to 3200 m²/g) are shown in **Figure 12**. For clarity, only adsorption isotherm traces are shown. In all instances, the adsorption and desorption data were identical and no hysteresis could be observed. The sample with the surface area of 330 m²/g adsorbs 0.8 wt % at 20 bar, whereas the 3200 m²/g sample adsorbs 5.3 wt % hydrogen at 30 bar pressure. The ACA's with surface areas of 1460, 2000, and 2550 m²/g show maximum values taken from the surface excess adsorption isotherms that are intermediate to these values, as expected. Of interest in this work was the fact that an ACA could be prepared with a surface area of 3200 m²/g, greater than the surface area of a single graphene sheet (2630 m²/g, if both graphene surfaces are taken into account) and comparable to high-surface-area activated carbons. Presumably, edge terminations make up a substantial fraction of the surface area of the ACAs, as can be the case for activated carbons.

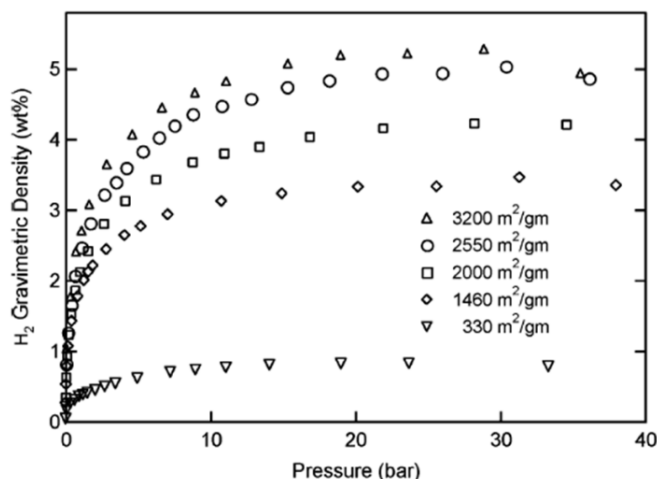


Figure 12. Adsorption isotherms at 77 K for the undoped ACAs. The organic aerogel with a surface area of 330 m²/g was not carbonized.

We also studied the sorption dependence of nickel and cobalt incorporation into the carbon aerogel framework (Figure 14). Previous work had shown the metal nanoparticle content in these CA's to be ~ 9-10 wt % using elemental analysis. Nanoparticles are distributed homogeneously in the CA network, and the accessible surface area of these nanoparticles is related to the carbonization temperature. For example, when carbonization is performed at 1050 °C, the metal nanoparticles are typically encased in graphitic carbon, whereas at 800 °C, this effect is less pronounced and, as a result, the metal nanoparticles still possess accessible surface area. The adsorption isotherms at 77 K for the Co-modified CAs carbonized at 800 and 1050 °C are similar, with maximum values of ~2.1 wt % for each sample. The effect of carbonization temperature on sorption behavior for the Ni-modified CAs is more pronounced, with the material carbonized at 800 °C showing ~10% enhancement in the maximum value (2.3 vs 2.0 wt %) over the material carbonized at 1050 °C despite having a lower BET surface area (970 m²/g vs 1100 m²/g). Moreover, the value of the sorption capacity is decreased by the nickel mass contribution. Thus, the increase would be higher only if the carbon mass was taken in account. The observed enhancement may be attributable to H₂ interaction with accessible Ni particles, consistent with behavior previously described as metal-assisted cold-storage¹⁰ or "spillover", and is the dissociation of molecular hydrogen at the surface of the metal followed by migration

and adsorption on the carbon surface. Recently, this technique has been used to enhance hydrogen storage in nanostructured carbons. We cannot, however, discount the possibility that the metal dopants influence the textural properties of the CA during carbonization. For instance, the Ni may be altering the CA structure during pyrolysis, making available pores that are not adequately measured by N₂ BET measurements but are accessible to H₂.

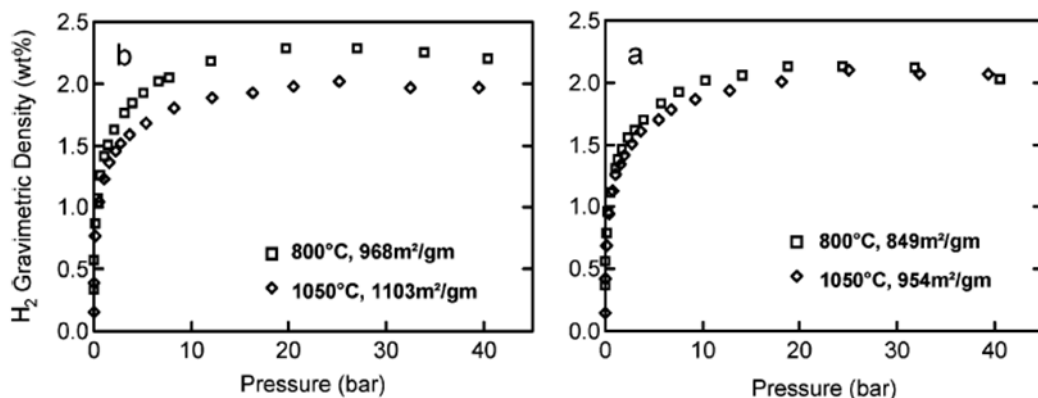


Figure 14. Comparison of the adsorption isotherms at 77 K for the (a) Co and (b) Ni-modified CAs that have been carbonized at 800 or 1050 °C.

In order to evaluate the similarity of surface area dependence of adsorption in carbon aerogels to that of activated carbons, we plotted the maximum amount of hydrogen adsorbed in the surface excess isotherm trace versus the BET surface area. We note that this approach varies somewhat from the original analyses of Chahine, as the maximum surface excess quantity of sorbed hydrogen can occur at pressures other than 35 bar. In our aerogels, the maximum occurs typically at ~30 bar for higher-surface area materials. We also note that we express the maximum value in wt%, which yields a slightly lower quantity than values expressed in milligrams of sorbed hydrogen per gram of sorbent. At 77 K, hydrogen surface excess sorption of CAs scales with BET surface area up to 2550 m²/g, yielding up to 5 wt% gravimetric density. The surface area dependence for the aerogel with a surface area of 3200 m²/g is somewhat weaker, with a gravimetric density of 5.3 wt%. The absolute value of 5.3 wt % is comparable to the highest value we have measured in an activated carbon; however, aspects of the structure of the aerogel with a surface area of 3200 m²/g might promote H₂-H₂ gas interactions that would weaken the surface area dependence. We are presently investigating this behavior. Whereas adiabatic calorimetry provides the most direct measure of thermodynamic behavior during hydrogen uptake, we can rely on other approaches to evaluate sorption enthalpies. The easiest means is to evaluate the differential enthalpy of adsorption at zero coverage from the isotherm, as defined by an analysis of the Henry's law region (low pressure, linear regime slope). While we now recognize that a Henry's law analysis falls short of the complete isosteric enthalpy as a function of hydrogen loading, this initial analysis helped enable us to probe the role of metal additions during the onset of adsorption, minimizing interactions between adsorbed hydrogen molecules. To this end, high-resolution isotherm measurements at low pressure (in the range 0-2.5 bar) were performed. The analysis of Cole^{23,24} enabled us to use a region

²³ Cole, J. H.; Everett, D. H.; Marshall, C. T.; Paniego, A. R.; Powl, J. C.; Rodriguez Reinoso, F. *J. Chem. Soc., Faraday Trans. 1974*, 1 70, 2154.

²⁴ Rouquerol, F.; Rouquerol, J.; Sing, K. *Adsorption by Powders and Porous Solids*; Academic Press: New York, 1999.

of the isotherm beyond the linear portion to obtain the relevant enthalpies, as summarized in Table 2.

As with values reported in the literature for activated carbons, we found a linear dependence of H₂ surface excess maximum values with the surface area as seen in other types of carbons. In addition, we noted an increase in the H₂ excess gravimetric density for a CA that has been doped with Ni nanoparticles. The differential enthalpy of adsorption at zero coverage for the metal modified materials was measured to be >7 kJ/mol, slightly higher than for unmodified aerogels.

Microporous Carbons

Before proceeding with a discussion of the role of Platinum group metals (PGM) that are known to dissociate hydrogen in heterogeneous catalysts and that have been suggested as a solution to ambient temperature hydrogen adsorption via “spillover”, we will describe some of the work we performed in probing the role of micropore geometry in activated carbon fibers. The interest in this aspect of our work arose from computational efforts that suggest an enhancement in enthalpy due purely to wave function overlap of two closely spaced slit-pore walls. Our previously described picture of what might be an idealized slit pore might represent the optimal geometry for an adsorbent.

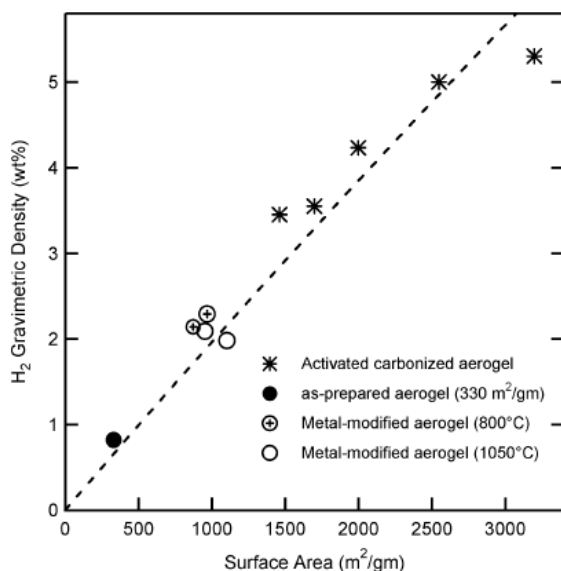


Figure 15. Excess gravimetric density (H₂ wt %) saturation value at 77 K as a function of BET surface area. The line is 1 mass% sorption per 500 m²/g, converted to wt %.

Table 2. Differential enthalpy of adsorption at zero coverage and maximum values at 77 K for activated and metal-modified CA's.

CA material	ΔH (kJ/mol)	H ₂ (wt %)
ACA (1460 m ² /g)	6.7	3.5
ACA (1700 m ² /g)	6.5	3.6
ACA (2000 m ² /g)	6.4	4.2
ACA (2550 m ² /g)	6.4	5.0
ACA (3200 m ² /g)	6.2	5.3
Co-CA-800 °C (1050°C)	7.5 (7.2)	2.1 (2.1)
Ni-CA-800 °C (1050°C)	7.0 (7.1)	2.3 (2.0)

One of the dilemmas of sorption-based hydrogen (H₂) storage in microporous carbons is the trade-off between adsorption capacity and adsorption enthalpy²⁵. Conceptually, this problem is best illustrated in terms of the ideal slit pore formed from two parallel, semi-infinite graphite slabs as we discussed earlier. Packing density (and adsorption capacity) is maximized when the pore width is several times larger than the diameter of the H₂ molecule, since it permits the formation of several hydrogen monolayers within the pore²⁶. At supercritical temperatures (i.e. above $T_c = 33$ K) the H₂-pore

²⁵ Bhatia S K and Myers A L 2006 Optimum conditions for adsorptive storage *Langmuir* **22** 1688

²⁶ Wang Q and Johnson J K 1999 Molecular simulation of hydrogen adsorption in single-walled carbon nanotubes and idealized carbon slit pores *J. Chem. Phys.* **110** 577

interactions are more dominant than the H₂–H₂ interactions and condensation within pores does not occur. Characteristic H₂ adsorption enthalpies associated with large slit pores therefore approach the enthalpy of H₂ adsorption on carbon, typically measured between 4 and 6 kJ/mol²⁷. With smaller pores, the adsorption enthalpy increases due to the overlap of potentials fields from each face of the pore. The packing density begins to decrease, though, when the pore is no longer wide enough to accommodate two H₂ monolayers. *ab initio* calculations of hydrogen adsorption in ideal slit pore carbons are largely consistent with this picture²⁸. Experimental work on the fundamental limitations of hydrogen delivery from carbon sorbents is rare, however, because uniform slit pore structures do not occur in nature. To extend the slit pore concept to more realistic carbon adsorbents, the distribution of pore sizes must be understood.

Activated carbon fibers (ACFs), due to their microporosity, are an excellent material for a fundamental study of H₂ adsorption capacity and enthalpy. Synthesized from polymeric carbon precursors, ACFs contain narrow and uniform pore size distributions with widths on the order of 1 nm²⁹. Images of ACFs from scanning tunneling microscopy have revealed networks of elongated slit-shaped and ellipsoid shaped pores^{30,31}. Edge terminations in graphitic layers are thought to be the most reactive sites during the steam/carbon dioxide activation process, resulting in a gradual lengthening of slit-shaped pores as a function of burn-off³². ACFs subjected to less burn-off will have smaller pore volumes and a greater abundance of narrow pores widths. With longer activation times, the pore volume increases and the pores grow wider. This offers a convenient control for an experimental study of the correlation between pore structure and hydrogen adsorption. In our study of ACF's³³, the pore size distribution (PSD) of activated carbon fibers is used to interpret the enthalpy and the capacity of supercritical H₂ adsorption. Two ACF samples subjected to different degrees of activation were characterized. First, the microstructure of the activated carbon samples was investigated with high resolution transmission electron microscopy (HRTEM). Next, the PSD is obtained from argon adsorption measurements and modeling with the density functional theory (DFT) method. Supercritical hydrogen adsorption isotherms are then measured, from which the adsorption enthalpy and adsorption capacities are obtained. Similar measurements are made for a microporous, coconut derived activated carbon to determine whether self-consistent interpretations of hydrogen adsorption properties in terms of the PSD can be extended to other carbon sorbents.

The Kynol™ activated carbon fiber samples ACF-1603-10 (ACF10) and ACF-1603-20 (ACF20) were obtained from Kynol Inc. These ACFs are produced by carbonization and steam/carbon dioxide gasification of a phenolic resin precursor. The last two digits in the labels are an approximate indication of surface area in hundreds of m²/g. The commercial,

²⁷ Pace E L and Siebert A R 1959 Heat of adsorption of parahydrogen and orthodeuterium on graphon *J. Phys. Chem.* **63** 1398–400

²⁸ Gigas A, Bhatia S K, Anil Kumar A V and Myers A L 2007, Feasibility of tailoring for high isosteric heat to improve effectiveness of hydrogen storage in carbons *Carbon* **45** 1043

²⁹ Stoeckli F, Centeno T A, Fuertes A B and Muniz J 1996 Porous structure of polyarylamide-based activated carbon fibres *Carbon* **34** 1201

³⁰ Daley M A, Tandon D, Economy J and Hippo E J 1996 Elucidating the porous structure of activated carbon fibers using direct and indirect methods *Carbon* **34** 1191–1200

³¹ Paredes J I, Mart'inez-Alonso A and Tasc'on J M D 2001 Characterization of microporosity and mesoporosity in carbonaceous materials by scanning tunneling microscopy *Langmuir* **17** 474

³² Yang R T 2003 *Adsorbents: Fundamental and Applications* (Hoboken, New Jersey: Wiley Interscience)

³³ J J Purewal, H Kabbour, J J Vajo, C C Ahn and B Fultz, Pore size distribution and supercritical hydrogen adsorption in activated carbon fibers, *Nanotechnology* 20 (2009) 204012 (6pp) doi:10.1088/0957-4484/20/20/204012

coconut-shell-derived activated carbon CNS-201 (CNS201) was purchased from A.C. Carbon Canada Inc. Because CNS201 is known to be highly microporous, containing 90% of slit pores smaller than 1.3 nm, it is a useful reference material for the microporous ACFs³⁴. Argon isotherms were measured at 87 K for ACF10 (0.2811 g) and ACF20 (0.3222 g). A nitrogen isotherm was measured at 77 K for CNS201 (0.1019 g). These measurements were made with a Micromeritics ASAP 2020. Surface areas and saturation pore volumes were calculated from the BET method and the Dubinin–Radushkevich (DR) method³⁵, respectively, as implemented in Micromeritics ASAP 2020 Version 3.01 software. Pore size distributions from the original DFT method were calculated using Micromeritics ASAP 2020 Version 3.01 software with DFT Plus4.

High resolution TEM micrographs were acquired on a Tecnai F30 UT operated at 300 keV. Sample preparation consisted of grinding about 10 mg of the ACF10 sample in isopropanol and dispersing it on a carbon grid. High-pressure H₂ isotherms were measured with a custom-built Sieverts apparatus at temperatures of 77, 87, and 195 K. The sample masses used for the hydrogen adsorption measurements were 0.1782 g (ACF10), 0.2114 g (ACF20) and 0.903 g (CNS201). Prior to adsorption measurements, samples were degassed by heating at 200 °C under vacuum for 12 h. Sample masses were measured again after the adsorption experiment to check for changes in mass due to removal of residual water. The total volume of the Sieverts instrument, including both the reference volume and the reactor volume, is less than 68 cm³, permitting accurate measurements using the volumetric method. The true sample volume was subtracted by assuming a skeletal density of 2.1 g/ml, which is known to be accurate for carbon samples. To account for real gas behavior, normal H₂ gas densities were determined from measured temperatures and pressures using the RefProp Standard Reference Database³⁶.

A high resolution TEM micrograph of ACF10 is presented in Figure 16. Activated carbon fibers are known to be more graphitic than typical activated carbons³⁷, but this is not obvious from the HRTEM image. The microstructure appears to be random rather than showing well-ordered, regularly spaced graphitic planes. It appears similar to the highly disordered microstructures typically observed for activated carbon³⁸. Micropore or mesopore structures were not visible with the HRTEM analysis. Since the HRTEM image is based on the exit electron wavefunction, however, the combination of finite sample thickness and non-periodicity tends to conceal micropore structures.

The BET surface areas and total pore volumes for ACF10, ACF20, and CNS201 are listed in **Table 3**. As expected, ACF10 (subject to less burn-off than ACF20) has a smaller pore volume and smaller BET surface area than ACF20. The activated coconut carbon CNS201 appears to have a BET surface area and pore volume which is intermediate between the two ACFs (since this is the N₂ BET surface area, direct comparisons with the Ar BET surface areas of ACF10 and ACF20 should be considered approximate). Calculated surface areas of activated carbons are often unrealistically high, since the micropore

³⁴ Benard P and Chahine R 1997 Modeling of high-pressure adsorption isotherms above the critical temperature on microporous adsorbents: application to methane *Langmuir* **13** 808

³⁵ Dubinin M M 1967 *J. Colloid Interface Sci.* **23** 487

³⁶ Lemmon E W, Huber M L and McLinden M O 2007 *NIST Standard Reference Database 23: Reference Fluid Thermodynamic and Transport Properties-REFPROP* Number Version 8.0 in Standard Reference Data Program. National Institute of Standards and Technology, Gaithersburg

³⁷ Yang R T 2003 *Adsorbents: Fundamental and Applications* (Hoboken, New Jersey: Wiley Interscience)

³⁸ Baker F S, Miller C E, Repik A J and Tolles E D 2003 Activated carbon *Kirk-Othmer Encyclopedia of Chemical Technology* vol 4 (New York: Wiley) p 741

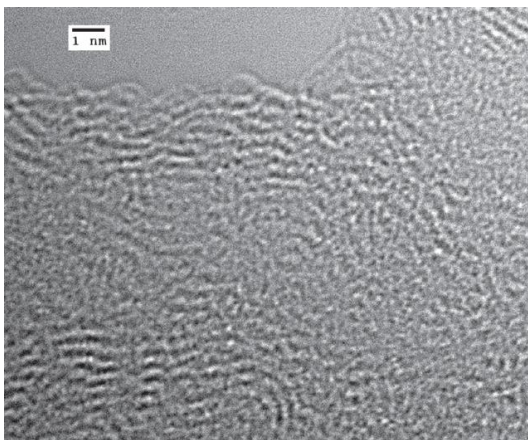


Figure 16. High resolution TEM image of ACF10. Length scale is indicated in the figure.

adsorption mechanism is not equivalent to the multilayer process assumed in the BET model. Nevertheless, the BET method is useful for comparisons between different materials.

Pore size distributions obtained from the DFT method are displayed in Figure 17. The pore width is defined as $L-d$, where L is the internuclear spacing between the walls of the slit pore and d is the van der Waals diameter of carbon (0.34 nm). Since graphite has an interlayer spacing of $L = 0.335$ nm, a slit pore formed from a single missing graphene plane has a width of 0.33 nm. A slit pore formed from two missing graphite planes has a width of 0.67 nm, and a pore formed from three missing graphene planes has a width of 1.0 nm. Taking into account the finite diameter of Ar (0.28 nm) and N₂ (0.30 nm), the cutoff in the pore spectrum must be above 0.3 nm. (Smaller probe molecules, such as helium could measure pore widths below this cutoff.)

The pore size distributions displayed in Figure 17 all show a sharp increase in intensity just below 0.50 nm, which corresponds to a width that is between the predicted pore widths for one or two removed graphene planes. This may simply reflect the smallest pore width which is measurable by the specific probe molecule. Another possibility is that after the removal of two layer planes, the slit pore structure relaxes to the observed 0.5 nm spacing. The pore distribution of ACF10 is narrow, consisting of the single large peak at 0.5 nm. Since burn-off in ACF10 was minimized, larger pore structures did not develop fully, and are present only as a small tail in the PSD. In the pore size distribution of ACF20, there is a broad distribution of pore widths between 0.5 and 2.0 nm with a small positive skew. Since ACF20 was subject to a greater degree of burn-off, larger pores were formed during the activation process. The minima near 0.6 and 1.0 nm are likely to be model-induced artifacts which are independent of the actual sorbent material³⁹. The coconut-derived activated carbon CNS201 also appears to have a distribution of pore widths between 0.5 and 2.0 nm with a positive skew. This broad distribution of pore widths in ACF20 and CNS201 may reflect the presence of slit pores formed from the removal of up to 6 graphene planes.

Supercritical H₂ isotherms of ACF10, ACF20, and CNS201 are displayed in Figure 17. Gibbs excess adsorption is the physical quantity that is measured experimentally. Therefore, supercritical isotherms often have a maximum at high pressures where the bulk

³⁹ Olivier J P 1998 Improving the models used for calculating the size distribution of micropore volume of activated carbons from adsorption data *Carbon* **36** 1469

gas density begins to increase faster than the adsorbate surface density^{40,41}. This behavior is visible in the isotherms of both ACF10 and ACF20. As shown in Table 4, the 77 K adsorption capacities of ACF10, ACF20, and CNS201 are 2.1 wt%, 3.5 wt%, and 2.5 wt%, respectively. Comprehensive studies of H₂ adsorption in activated carbons report a linear dependence of storage capacity at 77 K with specific surface area^{2,42,43,44}. When the H₂ adsorption capacity is expressed as a mass%, an increase of approximately 1 wt% hydrogen is observed for every 500 m² g⁻¹ of surface area. As shown in the inset of Figure 18, the H₂ adsorption capacity of ACF10, ACF20, and CNS201 at 77 K roughly follows this linear relation.

Table 3. The BET specific surface areas (SSA) in m²/gm and total specific pore volumes (V) in cm³/gm from the Dubinin–Radushkevich equation are listed. The textural parameters of ACF10 and ACF20 were obtained from argon measurements at 87 K while those of CNS201 were obtained from N₂ measurements at 77 K.

	SSA (m ² g ⁻¹)	V(cm ³ g ⁻¹)
ACF1603-10	801	0.296
ACF1603-20	1817	0.706
CNS-201	1158	0.452

At low surface excess concentration, Henry’s law gives a linear relationship between the amount of adsorption and the equilibrium pressure, $n = k_H \times p$. Adsorption in the ‘Henry’s law’ region can be even more accurately modeled by a virial-type equation (Equation 13) to take into account small deviations from linearity²⁴,

Accurate adsorption amounts were measured in the low pressure region using a high resolution pressure gauge. Henry’s law constants were then calculated at 77, 87 and 195 K from the zero-order virial coefficient, $C_1 = \ln(k_H)$. The differential enthalpy of adsorption was calculated from the temperature variation of k_H calculated using the van’t Hoff expression (Equation 19).

Metal Modified Carbons

As a follow on to the aerogel work and motivated by previous efforts of J Schwarz⁴⁵ at the Syracuse University in defining what was at the time referred to as metal assisted cold storage, Ted Baumann at LLNL was kind enough to continue to provide robust aerogels that we might use in an attempt to incorporate Group VIII metals. The original work of Schwarz used Ni metal and our interest in other Group VIII’s was motivated by the use of these metals in their use as dissociation catalysts in other systems. Over the course of 2006-2007, a Ni modified aerogel with a 1650 m²/gm surface area was synthesized with a 77K isotherm

⁴⁰ Benard P and Chahine R 2001 Determination of the adsorption isotherms of hydrogen on activated carbons above the critical temperature of the adsorbate over wide temperature and pressure ranges *Langmuir* **17** 1950–5

⁴¹ Dillon A C and Heben M J 2001 Hydrogen storage using carbon adsorbents: past, present and future *Appl. Phys. A* **72** 133

⁴² Kabbour H, Baumann T F, Satcher J H Jr, Saulnier A and Ahn C C 2006 Toward new candidates for hydrogen storage: high-surface-area carbon aerogels *Chem Mater.* **18** 6085

⁴³ Panella B, Hirscher M and Roth S 2005 Hydrogen adsorption in different carbon nanostructures *Carbon* **43** 2209–14

⁴⁴ Nijkamp M G, Raaymakers J E M J, van Dillen A J and de Jong K P 2001 Hydrogen storage using physisorption — materials demands *Appl. Phys. A* **72** 619–23

⁴⁵ Effect related to work of J. Schwarz of Syracuse, “Metal assisted cold storage of hydrogen,” U.S. patent 4,716,736.

with a Ni catalyst distribution as shown in **Figure 19**. The isotherms from this material are shown in **Figure 20** for the as analyzed isotherm.

Effective storage of hydrogen by physisorbent materials has remained limited to cryogenic temperatures since hydrogen binding interactions are not significantly larger than the average thermal energy at 298 K, typically $4\text{--}6\text{ kJ (mol H}_2\text{)}^{-1}$. The excess adsorption capacities of known materials are less than 10 mmol g^{-1} (2 wt%), and less than 5 mmol g^{-1} in all but a few select cases. These figures do not include the added mass of the storage vessel and delivery apparatus, and are far from the targets suggested by the DOE for mobile vehicle applications. The volumetric density enhancement from hydrogen adsorption

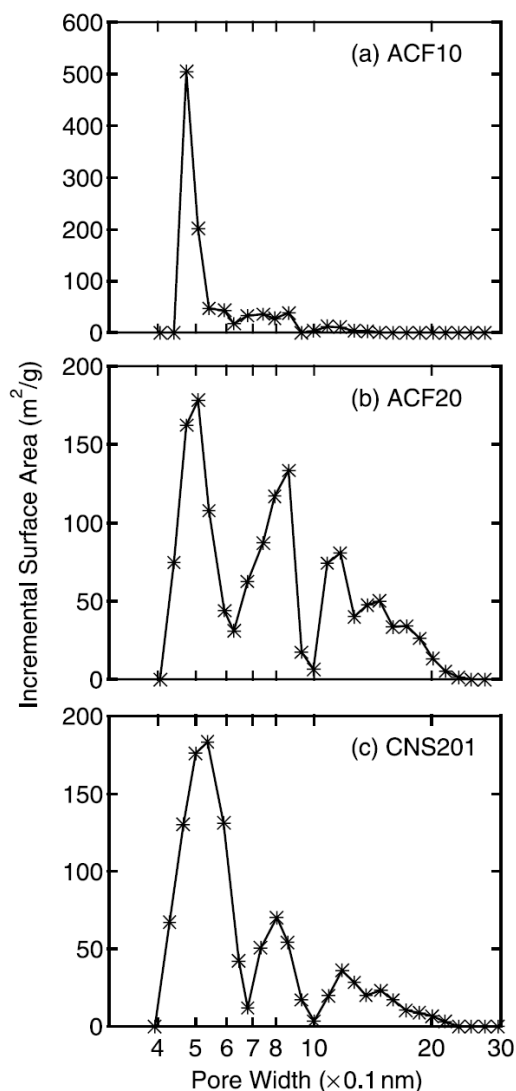


Figure 17. (a) Pore size distributions determined by the DFT method for (a) ACF10, (b) ACF20 and (c) CNS201. The bottom axis is shown in logarithmic scale.

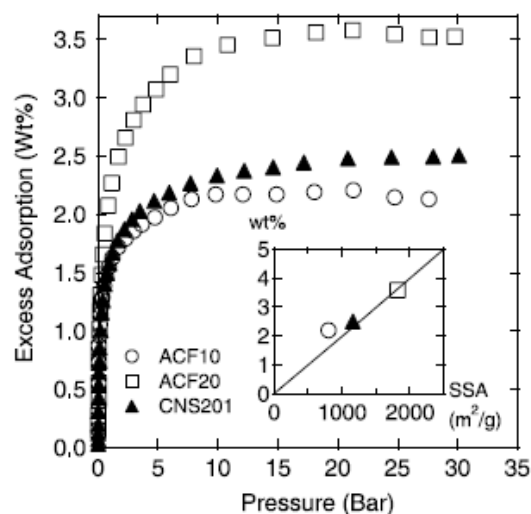


Figure 18. Above, hydrogen adsorption isotherms at 77 K of (open circle) ACF10, (open square) ACF20 and (solid triangle) CNS201. Inset: excess gravimetric density ($\text{H}_2\text{ wt}\%$) maximum value at 77 K as a function of BET specific surface area ($\text{m}^2\text{ g}^{-1}$), with the solid line signifying a 1 wt% per $500\text{ m}^2\text{ g}^{-1}$ linear relationship.

Table 4. Adsorption enthalpy at zero coverage and saturation H₂ adsorption amounts at 77 K. For clarity, positive enthalpies are displayed even though adsorption is exothermic.

Material	ΔH_0 (kJ mol ⁻¹)	H ₂ (wt%)
ACF1603-10	8.92	2.1
ACF1603-20	7.63	3.5
CNS-201	8.59	2.5

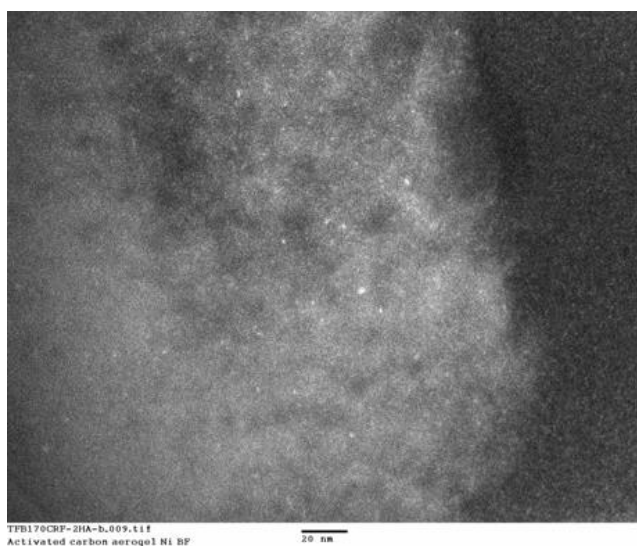


Figure 19. A high angle annular dark field image showing Ni catalyst particles (light dots) incorporated into a carbon aerogel.

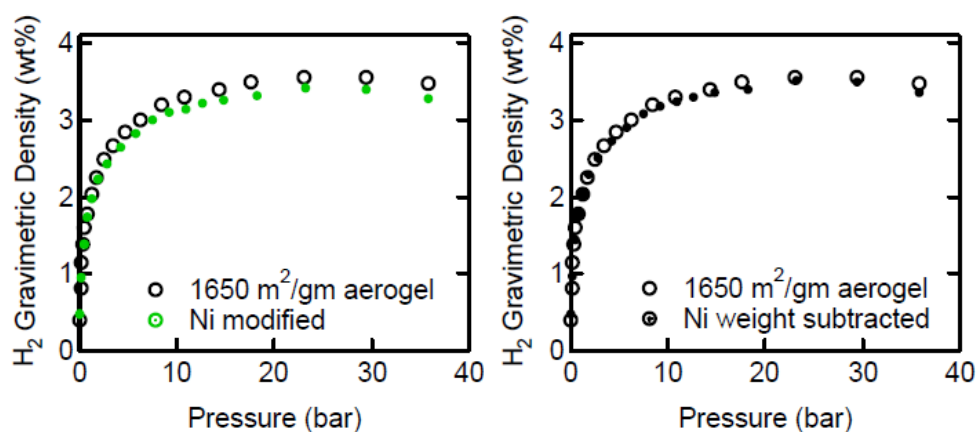


Figure 20. 77 K isotherms for a Ni modified aerogel on the left. The figure on the right shows an almost identical set of isotherm traces when the mass of the Ni is normalized out of the analysis, indicating that no role of Ni can be discerned in enhancing hydrogen uptake.

room temperature has also not been shown to be significant enough to overcome the penalty in mass of including the sorbent.

Continuing an effort to further explore the possibility of a dissociation reaction that is more typical of intermetallic hydrides, where Group VIII metals are used to convert gaseous hydrogen to the atomic form, we continued to explore the possibility of this phenomenon in light of literature reports in this area. It was proposed that an enhancement of the hydrogen storage capacities of physisorptive materials can be gained by hydrogen spillover from a metal catalyst onto the adsorbing surface.^{46,47,48,49,50,51} Hydrogen spillover is dissociative chemisorption of dihydrogen onto a metal particle followed by migration of hydrogen atoms onto the surface of the bulk material and subsequent diffusion away from the receptor site^{52,53,54} as shown in Figure 21.

The spillover concept is well documented in heterogeneous catalysis⁵⁴ but has only recently been studied as a hydrogen storage mechanism. Reports of remarkable increases in hydrogen uptake for these systems have generated much further research, even toward enhancing contact between the metal sites and the substrate surface via carbonized “bridges”.⁴⁸ However, the details of hydrogen spillover are not understood. This is partly because of the challenging task of detecting atomic hydrogen in spillover systems and partly because of the inherent difficulties in accurately measuring small changes in hydrogen uptake at room temperature. Although direct observation of atomic hydrogen has been recently demonstrated by transmission electron microscopy on a single graphene sheet⁵⁵, volumetric measurements of hydrogen uptake are never this sensitive. Investigations using inelastic neutron scattering also recently yielded evidence of the formation of new C-H bonds on the surface of activated carbon fibers after spillover from palladium clusters; however, reversibility was unclear and enhancement attributed to spillover was not tested at high pressures⁴⁹. Interestingly, theoretical models cannot account for the remarkable enhancement of hydrogen uptake capacity in carbon materials due to spillover reported by experimental investigation^{49,56,57,58}. Platinum, palladium, and nickel have been studied as metal catalysts for spillover, while materials including zeolites, metal-organic frameworks (MOFs), and carbons were used as host materials.

⁴⁶ A. D. Lueking and R. T. Yang, 'Hydrogen spillover to enhance hydrogen storage – study of the effect of carbon physicochemical properties', *Appl. Catal., A*, **265**, 259-68 (2004).

⁴⁷ Y. Li and R. T. Yang, 'Hydrogen storage on platinum nanoparticles doped on superactivated carbon', *J. Phys. Chem. C*, **111**, 11086-94 (2007).

⁴⁸ Y. Li and R. T. Yang, 'Hydrogen storage in metal-organic frameworks by bridged hydrogen spillover', *J. Am. Chem. Soc.*, **128**, 8136-37 (2006).

⁴⁹ C. I. Contescu, C. M. Brown, Y. Liu, V. V. Bhat, and N. C. Gallego, 'Detection of hydrogen spillover in palladium-modified activated carbon fibers during hydrogen adsorption', *J. Phys. Chem. C*, **113**, 5886-90 (2009).

⁵⁰ D. Saha and S. Deng, 'Hydrogen adsorption on ordered mesoporous carbons doped with Pd, Pt, Ni, and Ru', *Langmuir*, **25**, 12550-60 (2009).

⁵¹ M. Zieliński, R. Wojcieszak, S. Monteverdi, M. Mercy, and M. M. Bettahar, 'Hydrogen storage in nickel catalysts supported on activated carbon', *Int. J. Hydrogen Energy*, **32**, 1024-32 (2007).

⁵² A. J. Robell, E. V. Ballou, and M. Boudart, 'Surface diffusion of hydrogen on carbon', *J. Phys. Chem.*, **68**, 2748-53 (1964).

⁵³ S. T. Srinivas and P. K. Rao, 'Direct observation of hydrogen spillover on carbon-supported platinum and its influence on the hydrogenation of benzene', *J. Catal.*, **148**, 470-77 (1994).

⁵⁴ W. C. Conner and J. L. Falconer, 'Spillover in heterogeneous catalysis', *Chem. Rev.*, **95**, 759-88 (1995).

⁵⁵ J. C. Meyer, C. O. Girit, M. F. Crommie, and A. Zettl, 'Imaging and dynamics of light atoms and molecules on graphene', *Nature*, **454**, 319-22 (2008).

⁵⁶ L. Chen, A. C. Cooper, G. P. Pez, and H. Cheng, 'Mechanistic study on hydrogen spillover onto graphitic carbon materials', *J. Phys. Chem. C*, **111**, 18995-9000 (2007).

⁵⁷ A. K. Singh, M. A. Ribas, and B. I. Yakobson, 'H-spillover through the catalyst saturation: an ab initio thermodynamics study', *ACS Nano*, **3**, 1657-62 (2009).

⁵⁸ G. M. Psogiannakis and G. E. Froudakis, 'DFT study of the hydrogen spillover mechanism on Pt-doped graphite', *J. Phys. Chem. C*, **113**, 14908-15 (2009).

In our studies, the hydrogen spillover effect was tested in the simplest experimental systems. Results from both Ni and Pt nanoparticles directly dispersed on high surface area carbons were used as the metal receptor sites for hydrogen dissociation. Platinized carbon was the standard system studied in the discovery of the spillover phenomenon⁵², the benzene hydrogenation experiments that later confirmed the spillover mechanism⁵³, and in the first reports of spillover enhancement to hydrogen storage capacity.**Error! Bookmark not defined.**⁴⁶

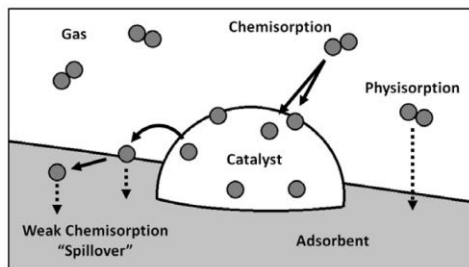


Figure 21. Spillover of the dissociated atoms of a diatomic molecule following chemisorption at the site of a catalyst particle, onto the surface of the support material.

Platinum metal does not form a bulk hydride phase and therefore only surface chemisorption is expected (unlike palladium where absorbed hydrogen complicates data analysis). While “bridging” is reported to increase hydrogen uptake by spillover⁴⁸, this phenomenon is not essential for spillover to occur and was not the topic of the work that we pursued. In addition to carbon aerogels, a commercially available superactivated carbon (Maxsorb MSC-30) was selected for its close similarity to AX-21, a high surface area carbon material previously used in spillover experiments. Hydrogen uptake isotherms of the platinum containing samples (Pt-MSC-30) were measured at room temperature (296 K), where spillover was expected. Synthesis and adsorption experiments were carried out in the most straightforward and standard way for corroborating the effect, following the steps reported by Li and Yang⁴⁷.

Materials Processing and Synthesis

MSC-30 and AX-21

In addition to work performed on LLNL aerogels, we invested most of our effort in a material with large availability, Maxsorb MSC-30, a superactivated carbon that was obtained from Kansai Coke & Chemicals Company, since it is a suitable support material for catalyst nanoparticles, essentially equivalent to AX-21 (from Anderson Development Co.) previously used in spillover experiments⁴⁷. Both MSC-30 and AX-21 are produced by activation of petroleum coke with molten KOH, using a process patented by Standard Oil Company (later, Amoco Corporation)⁵⁹. Both have a surface area near 3000 m²g⁻¹, exhibit similar chemical character and textural morphology, and are classified as “superactivated” or “AX-21 type” carbon³⁷. The oxygen content of superactivated carbon, a characteristic which may be important to the hydrogen spillover mechanism⁶⁰, is proportional to the BET surface area and is expected to be similar for both materials⁶¹.

⁵⁹ A. N. Wennerberg and T. M. O'Grady, U.S. Patent 4,082,694 (1978).

⁶⁰ L. Wang, F. H. Yang, R. T. Yang, and M. A. Miller, 'Effect of surface oxygen groups in carbons on hydrogen storage by spillover', *Ind. Eng. Chem. Res.*, **48**, 2920-26 (2009).

⁶¹ T. Otowa, Y. Nojima, and T. Miyazaki, 'Development of KOH activated high surface area carbon and its application to drinking water purification', *Carbon*, **35**, 1315-19 (1997).

Synthesis Methods

Maxsorb MSC-30 superactivated carbon (obtained from Kansai Coke & Chemicals Company, Ltd.) was stored at 393 K under vacuum in a Buchi glass oven. The Pt-MSC-30 samples were prepared by incipient wetness impregnation, in an analogous method as for Pt/AX-21⁴⁷. For each sample, 200 mg of dried MSC-30 was dispersed in acetone and magnetically stirred for 30 min at room temperature. A 2 mL solution consisting of 50 mg H₂PtCl₆ in acetone was then added dropwise to the stirring MSC-30 solution over 5 min. The slurry was removed and placed in an ultrasonic bath (50 W, 42 kHz, 1.9 L capacity) for 60 min and then magnetically stirred at room temperature for 24 h. The acetone was evaporated by heating the sample at 333 K for 12 h. The dry mixture was transferred to a ceramic boat and immediately placed in He flow inside a horizontal quartz tube furnace to prevent moisture uptake. The furnace was pre-heated to 393 K and held for 2 h under constant He flow. For reduction, the gas flow was switched to H₂ and the furnace was heated to 573 K and held for 2 h. The flow was again returned to He and the furnace allowed to cool to room temperature over 30 min. Each sample (~0.2 g) was sealed in a glass vial in Ar atmosphere and stored in a glovebox. A large number of 0.2 g Pt-MSC-30 samples (~40) were prepared and then combined to achieve sample sizes up to 3.2 g. Adapting the synthesis procedures of Pt/AX-21⁴⁷ to make large sample sizes required the use of multiple ceramic boats placed in a large diameter (5 cm) tube furnace. Sample characterization was undertaken to assure that individual syntheses yielded consistent products before combining them. Prior to hydrogen adsorption, the samples were degassed in vacuum at 623 K for 12 h. Sample mass that measured in the degassed state was varied from 0.2-3.4 g for isotherm experiments of Pt-MSC-30 and pure MSC-30.

Materials Characterization

Nitrogen Adsorption

Nitrogen isotherms were measured at 77 K for MSC-30 and Pt-MSC-30. These measurements were made with a Micromeritics ASAP 2420 and surface areas were calculated using the BET method as implemented by Micromeritics ASAP 2420 version 2.02 software. The BET surface areas of MSC-30 and Pt-MSC-30 were measured to be 3420 m²g⁻¹ and 2810 m²g⁻¹, respectively. The surface area of MSC-30 is larger than that of Anderson AX-21, reported as 2880 m²g⁻¹.⁴⁷ The decrease in surface area of MSC-30 upon adding Pt nanoparticles is consistent with the reported data for AX-21. This can be explained by Pt particles blocking or filling pores in the superactivated carbon.

X-Ray Diffraction

X-ray diffraction (XRD) experiments were performed using a PANalytical X'Pert Pro powder diffractometer with Cu K α _{1,2} radiation. Diffraction patterns of MSC-30 and Pt-MSC-30 are shown in Figure 22. The broad peak centered at $2\theta = 43^\circ$ for pure MSC-30 is consistent with that reported for AX-21. The peaks in the Pt-MSC-30 pattern at $2\theta = 39.9^\circ$ and 46.4° are the (111) and (200) reflections of the cubic platinum crystal structure. No platinum oxide peaks were detected, suggesting fully reduced Pt metal nanoparticles in the sample. From the widths of the diffraction peaks, the mean crystallite diameter was calculated with the Scherrer equation to be 3.6 nm (using the Scherrer constant $K = 0.83$ for spherical particles)⁶².

⁶² J. I. Langford and A. J. C. Wilson, 'Scherrer after sixty years: a survey and some new results in the determination of crystallite size', *J. Appl. Crystallogr.*, **11**, 102-13 (1978).

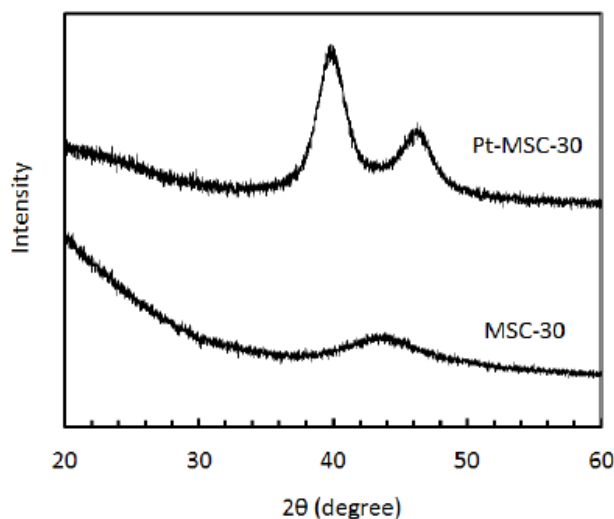


Figure 22. XRD patterns of Pt-MSC-30 and unmodified MSC-30.

Transmission Electron Microscopy

High resolution transmission electron microscopy (TEM) images were collected on a Tecnai TF30 operated at 300 keV. Scanning transmission electron microscopy (STEM) images were acquired with a high angle annular dark field (HAADF) detector. Samples were prepared for TEM by dispersing a finely ground mixture of Pt-MSC-30 and isopropanol on a holey carbon grid. TEM studies on Pt-MSC-30 showed a distribution in size of Pt particles from 2-10 nm in diameter, consistent with the 7 nm size determined from the Scherrer equation. TEM images at three magnifications are shown in Figure 24. The nanoparticles were highly dispersed on the surface of the activated carbon in all areas examined. This was further verified by HAADF microscopy, where intensity is proportional to Z^2 (Z is atomic number); platinum scatters electrons much more strongly than the carbon support and was readily observed in the form of small nanoparticles throughout the material.

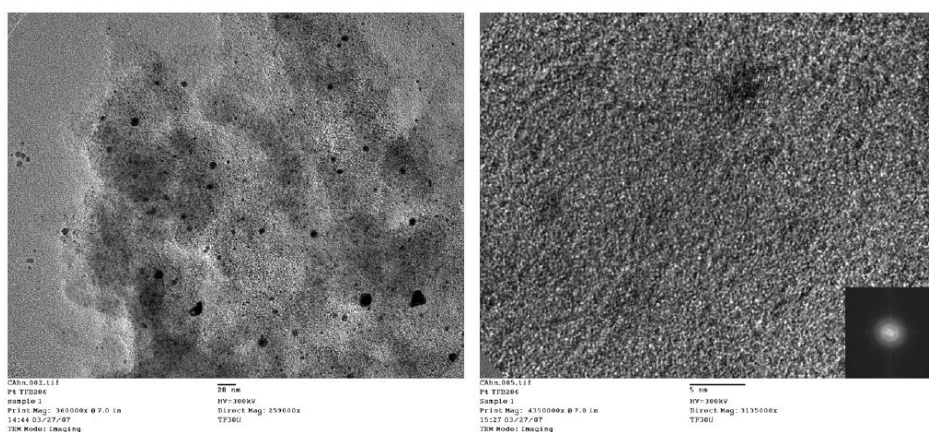


Figure 23. Bright field (left) and high resolution TEM images of as LLNL prepared aerogels with Pt catalysts incorporated at Caltech.

Thermal Gravimetric Analysis

Thermogravimetric analysis (TGA) was performed using a TA Instruments Q500 analyzer with a purge mixture of Ar/air in low flow (20 mL min⁻¹) and normal flow (70 mL min⁻¹) conditions, respectively. The temperature ramp was 10 °C min⁻¹ to 100 °C, held at 100 °C for 30 min, then increased 10 °C min⁻¹ to 1000 °C and held for 10 min. EDX data was not consistent from region to region and was not a reliable method to determine the Pt content in Pt-MS-30. Rather, platinum content was resolved from TGA data which showed a marked loss of mass between 375-415 °C, presumably oxidation of the organic components. The remaining mass at 1000 °C was attributed entirely to platinum and was 7.4% of the total. This value is less than the value of 12% predicted by stoichiometry for the synthesis.

Hydrogen Sorption

Hydrogen uptake isotherms were measured using our volumetric Sieverts apparatus. The system was leak tested over 1-20 h steps up to 7 MPa and showed a maximum leak rate of 1.4×10^{-5} mol h⁻¹ of H₂. If fitted to an exponential decay function,

$$n(t) = n_0 e^{-kt}$$

where k is the leak rate, this corresponds to a maximum leak of $k \sim 10^{-8}$ s⁻¹ which is negligible for short time measurement⁶³. The total volume of the apparatus, depending on the pressure gauge and sample holder selected, was 50-80 mL. The true volume of the sample was subtracted from the empty volume of the sample holder using a skeletal density of 2.1 g mL⁻¹ measured by helium expansion. Hydrogen was exposed to the sample at incrementally higher pressures over the course of each isotherm in uniform equilibration steps, ranging from 0.5-24 h per step in different experiments. The system was not returned to vacuum in between steps and the measured hydrogen uptake was cumulative from step to step. Hydrogen desorption was measured by an analogous method. The sample was evacuated to <1 mPa at room temperature between cycles.

Long-Duration Experiments

To measure the magnitude of the spillover effect at room temperature, unusually long measurements were necessary, sometimes exceeding 1 week in total duration. Even modest pressure (0.1-3 MPa) adsorption measurements of over 12 h duration showed significant scatter in all samples smaller than 0.5 g. Leakage, pressure history, and background adsorption were investigated. It was found that background adsorption in the empty sample holder at room temperature over long steps was comparable to the total uptake measured in 0.2 g samples. Equilibration time between isotherm steps and number of steps were varied to analyze these effects. Increasing the number of adsorption points and the duration of time for equilibration at each point significantly affected measured uptake, for measurements both with and without sample. The most effective approach to minimizing effects of background adsorption was to increase sample mass. It has been recommended that to avoid numerous pitfalls of hydrogen sorption experiments on carbon materials^{63,64} a sample mass >1 g is best. A custom-designed 20 mL sample holder was

⁶³ T. Kiyobayashi, H. T. Takeshita, H. Tanaka, N. Takeichi, A. Züttel, L. Schlapbach, and N. Kuriyama, 'Hydrogen adsorption in carbonaceous materials – how to determine the storage capacity accurately', *J. Alloys Compd.*, **330-332**, 666-69 (2002).

⁶⁴ G. G. Tibbetts, G. P. Meisner, and C. H. Olk, 'Hydrogen storage capacity of carbon nanotubes, filaments, and vapor-grown fibers', *Carbon*, **39**, 2291-301 (2001).

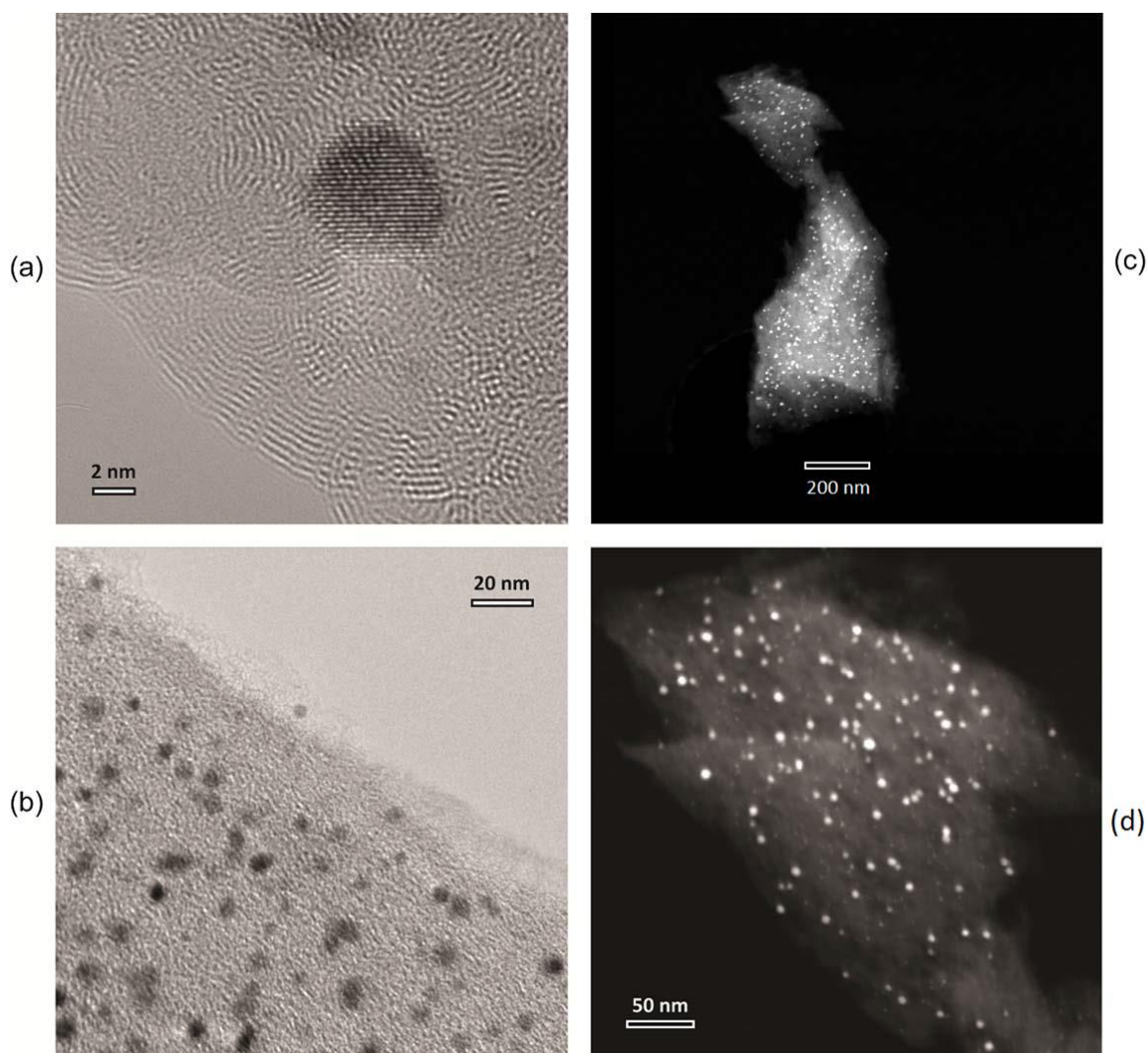


Figure 24. TEM micrographs of Pt-MSC-30 at (a) 4753000 \times and (b) 676600 \times magnifications. (c) STEM image obtained using a HAADF detector, verifying the successful dispersion of Pt nanoparticles throughout sample. (d) Higher magnification STEM image of an area in (c).

obtained for spillover measurements, accommodating approximately 3 g of sample. This allowed for significant increase in signal due to larger samples, but only a small increase in background. Of course, it is always necessary to subtract a unique background of empty sample holder adsorption from each isotherm measurement of a sample using the same number of isotherm points at roughly the same pressures and with identical technique.

Hydrogen Cycling

High-pressure hydrogen adsorption/desorption cycles were performed for multiple gram quantities of both MSC-30 and Pt-MSC-30, and are shown in Figure 25 and Figure 26.

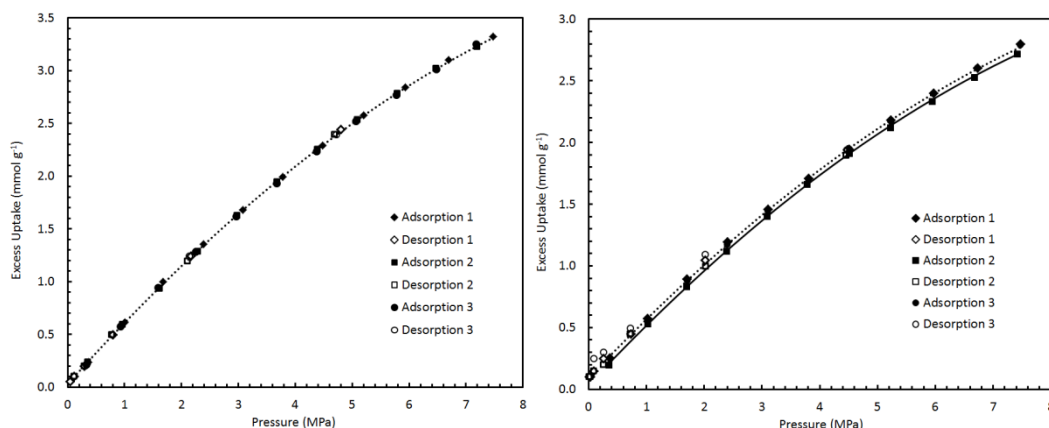


Figure 25. On left. Equilibrium adsorption/desorption isotherms of H₂ on MSC-30 at 296 K during three consecutive cycles between 0-8 MPa.

Figure 26. On right. Equilibrium adsorption/desorption isotherms of H₂ on Pt-MSC-30 at 296 K during three consecutive cycles between 0-8 MPa.

Hydrogen uptake and delivery were identical after many cycles for MSC-30. Hydrogen uptake capacity for MSC-30 at room temperature and 7 MPa was 3.2 mmol g⁻¹ (0.64 wt%). Using the same sample and degassing under vacuum at room temperature for 20 min between cycles, the standard deviation in this value was 0.0003 wt%. Complete desorption to 0.00 wt% at 0 MPa was achieved, with a standard deviation of 0.0006 wt%. Reloading the sample and performing the same adsorption/desorption cycles resulted in combined data which had a standard deviation of 0.003 wt%. This suggests that errors in determining the mass of the dried sample after cycling contributed to a small scatter in the data of different samples, a value within the bounds of usual experimental error.

Hydrogen uptake capacity in Pt-MSC30 was found to change on cycling. It was greatest during the first cycle (after degassing at 623 K under vacuum): 2.6 mmol g⁻¹ (0.53 wt%) at 7 MPa and room temperature. Upon desorption, hysteresis was observed. The desorption curve was extrapolated to 0 MPa, yielding a value of 0.02 wt% which could not be desorbed at room temperature for the first cycle. Using the same sample and degassing under vacuum at room temperature for 20 min between cycles, the uptake capacity at 7 MPa decreased to 0.52 wt% for subsequent cycles. Desorption under these conditions was possible to 0.02 wt% at 0 MPa in all cycles. If the sample is instead degassed for 8 h between cycles, uptake at 7 MPa is again 0.53 wt%. The amount remaining after desorption is approximately equal to the amount chemisorbed by Pt-MSC-30 at low pressure (0-0.1 MPa). This implies that some hydrogen remains chemisorbed on the surface of the Pt nanoparticles during degassing after short times, but can be removed by evacuating the sample under vacuum overnight.

In the low-pressure regime hydrogen uptake data are collected by a high resolution pressure manometer that is then blocked off for measurements above 0.1 MPa. It can be seen that the high resolution data are consistent with the high-pressure data for large (~3 g) samples in Figure 27. Together, the data are used to interpolate the point of intersection of the two isotherm curves.

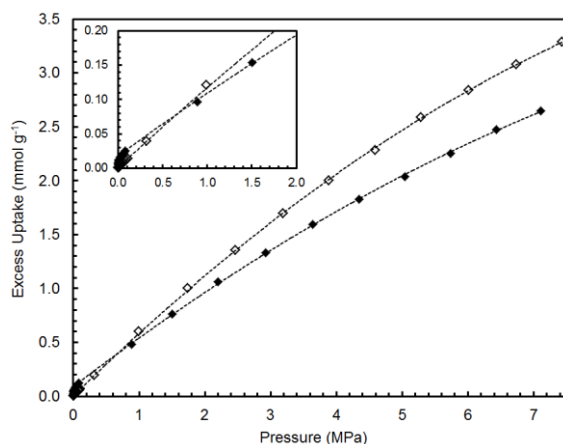


Figure 27. Fitted equilibrium adsorption isotherms for MSC-30 and Pt-MSC-30 at 296 K. The data is interpolated to intersect at 0.7 MPa and 0.08 wt%.

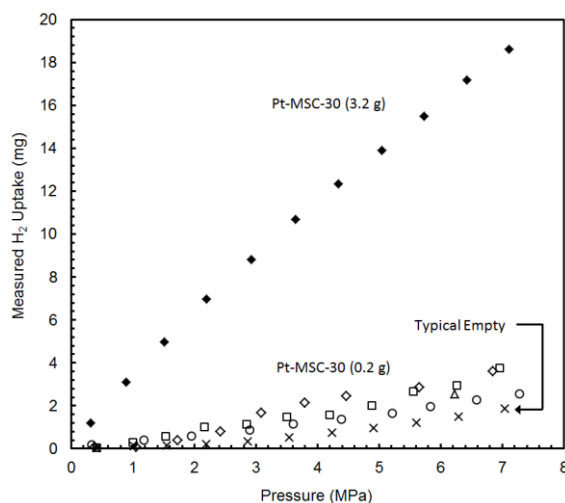


Figure 28. Equilibrium adsorption isotherms of H_2 on Pt-MSC-30 samples of varying mass compared to background adsorption by the empty sample holder (containing an aluminum blank) at 296 K. Uptake is shown in units of mass of H_2 detected as missing from the gaseous state, or “adsorbed” by the system.

Hydrogen Sorption Results

Hydrogen uptake isotherms were measured for MSC-30 and Pt-MSC-30 at room temperature, varying the sample size from 0.2–3.4 g. Similar isotherm measurements for aluminum blanks of comparable volume (0.1–1.5 mL) were used to determine the background adsorption of the empty sample holder. A comparison of measured hydrogen uptake (in mg H_2) as a function of pressure is shown for Pt-MSC-30 and an empty sample holder in Figure 28. In measurements with small samples (0.2 g), adsorption equilibrium was difficult to determine as room temperature fluctuations continued to slowly change pressure readings even after 60 minutes. Therefore, equilibration step durations between 0.5–24 h were performed, and results compared. The room temperature isotherm data for small samples of Pt-MSC-30 showed uptake varying from 2.5–3.7 mg H_2 at 7 MPa with larger apparent uptake for longer time of measurement. Temperature changes of even 1°C over the course of an isotherm step were also found to be highly correlated with large apparent uptake during that step. The problem may originate with the small temperature dependence of the pressure readings. This becomes a very important error for small samples at room temperature where the resolution of the pressure measurement has an important effect on the very small amount of uptake calculated. Hydrogen uptake in 0.2 g samples was a factor of 2 greater than the empty sample holder (background), but variations were also of this order (see Figure 28). In samples of mass >3 g, uptake was a factor of 10 greater than background and showed smooth curvature over the course of the experiment despite fluctuations in temperature.

Hydrogen uptake isotherms for large samples (>3 g) of Pt-MSC-30 and unmodified MSC-30 at room temperature, corrected for empty sample holder adsorption, are shown in Figure 28. Equilibrium was reached in less than 60 min between each isotherm step and was easily distinguished from continued adsorption. In pure MSC-30, the isotherm showed constant uptake as a function of pressure between 0–2 MPa. At pressures above 2 MPa, the slope decreased. At 6.7 MPa, hydrogen uptake in MSC-30 was 3.1 mmol g^{-1} , consistent with

reported values for MSC-30 to within 0.3 mmol g⁻¹.^{65,66} This value was reproducible upon cycling to well within experimental error, to which we assign an upper bound of ± 0.05 mmol g⁻¹. In Pt-MSC-30, low-pressure data showed a steep initial uptake of hydrogen between 0-0.01 MPa and then a similar constant slope region to MSC-30 between 0.04-2 MPa. The slope of the isotherm in Pt-MSC-30 also decreased slowly at pressures above 2 MPa. Hydrogen uptake at 7.1 MPa was 2.7 mmol g⁻¹ in the Pt containing sample on the first adsorption cycle, lower than for the unmodified MSC-30. This value decreased by up to 0.05 mmol g⁻¹ in subsequent adsorption cycles.

Discussion of “Spillover”

In pure MSC-30 at room temperature, the uptake of hydrogen showed Henry’s law behavior in the low-pressure region as expected for low coverage physisorption on activated carbon. The Henry’s law constant was 0.1 kg kg⁻¹ MPa⁻¹ at 296 K. The steep hydrogen uptake between 0-0.01 MPa in Pt-MSC-30 indicated very favorable initial chemisorption of hydrogen onto Pt nanoparticle surface sites. After these sites were filled, Henry’s law physisorption of H₂ on the carbon surface occurred in Pt-MSC-30 as in unmodified MSC-30. The Henry’s law constant for this physisorptive region was also found to be 0.1 kg kg⁻¹ MPa⁻¹ at 296 K, suggesting that the same adsorption mechanism is responsible for uptake in both the Pt-containing and unmodified samples at pressures above 0.01 MPa. As pressure increased, the slopes of both isotherms decreased from the Henry’s law value due to increased interactions between adsorbed molecules. In Pt-MSC-30, this effect was more apparent because of the additional mass of the platinum.

At 0.7 MPa, the H₂ uptake isotherms intersected at 0.4 mmol g⁻¹. Similar results were also reported for Pd particles on a lower surface area Maxsorb variant⁶⁷. The addition of Pt nanoparticles to MSC-30 affects only the initial chemisorption at low pressure. The reduced uptake for the room temperature Pt-MSC-30 system at 7 MPa can be readily estimated by making the assumption that the individual contributions of the heavier Pt particle mass (7.4% of the sample) and reduced surface area carbon support (linearly rescaled) were simply additive. In this way, the H₂ uptake was calculated to be 2.5 mmol g⁻¹, close to the measured value. The difference between these values is attributed to a small amount of hydrogen chemisorbed on the surface of the Pt particles.

Spillover has been reported to dramatically enhance H₂ uptake in a similar system, Pt/AX-21, at room temperature, high pressure, and for 0.2 g samples over long (~1 h) equilibration steps between isotherm points⁴⁷. All of these conditions risk substantial error accumulation using a standard Sieverts apparatus. Importantly, the sources of this error (leaks, temperature fluctuations, pressure hysteresis, and empty sample holder adsorption) are expected to cause an apparent *increase* in measured uptake, as opposed to a decrease. Small samples (0.2 g) of Pt-MSC-30 used in this study showed varying hydrogen uptake capacities in different experiments depending on the time allowed for equilibration, up to ± 0.6 mg H₂ at 7 MPa and 296 K. Error of this magnitude may normally not be encountered at low (cryogenic) temperature and short equilibration time, or simply ignored when

⁶⁵ H. Nishihara, P. X. Hou, L. X. Li, M. Ito, M. Uchiyama, T. Kaburagi, A. Ikura, J. Katamura, T. Kawarada, K. Mizuuchi, and T. Kyotani, 'High-pressure hydrogen storage in zeolite-templated carbon', *J. Phys. Chem. C*, **113**, 3189-96 (2009).

⁶⁶ Y. Kojima, Y. Kawai, A. Koiwai, N. Suzuki, T. Haga, T. Hioki, and K. Tange, 'Hydrogen adsorption and desorption by carbon materials', *J. Alloys Compd.*, **421**, 204-08 (2006).

⁶⁷ A. Ansón, E. Lafuente, E. Urriolabeitia, R. Navarro, A. M. Benito, W. K. Maser, and M. T. Martínez, 'Hydrogen capacity of palladium-loaded carbon materials', *J. Phys. Chem. B*, **110**, 6643-48 (2006).

overall uptake mass is much higher in the material. However, for 0.2 g samples of Pt-MSC-30, this contributed an error in reported uptake of $\pm 1.5 \text{ mmol g}^{-1}$ at 7 MPa and 296 K; this error is unacceptably high when the total uptake is 3.0 mmol g^{-1} . Experiments that require adsorption measurements of carbonaceous materials at room temperature over relatively long equilibration steps must utilize large sample masses to remedy these errors. The same error of $\pm 0.6 \text{ mg H}_2$ at 7 MPa and 296 K observed for a 3.2 g sample of Pt-MSC-30 is a factor of ten smaller in specific uptake (mmol g^{-1}), contributing a possible increase in measured uptake of up to 0.1 mmol g^{-1} . In large sample experiments, after an initial chemisorption at low pressure, platinum served only to increase the total mass of the sample and decrease available surface area for physisorption, thereby effecting a lower specific uptake of H_2 at high pressures.

Conclusions on spillover in carbons

If spillover occurred during hydrogen uptake in Pt-MSC-30, it was below the detection limit of volumetric gas adsorption experiments. The upper bound on the amount of hydrogen that participates in spillover is $0.005 \text{ mmol g}^{-1}$ which is outside of the accuracy of storage capacity measurements and is not a substantial enhancement for practical applications. The presence of Pt particles on superactivated carbon proved ineffective for increasing hydrogen uptake by spillover. After a small chemisorption at pressures below approximately 0.1 MPa, the platinum served to increase the overall mass of the material and decrease the available surface area, thereby decreasing the overall capacity.

Coordination polymers (MOF's), edge terminations, coordinatively unsaturated metal centers and uptake

The initial criterion we had discussed in attaining high gravimetric density relied on the observation that effective sorbents require a large number of sites on which adatoms (molecules) can adsorb. Given our understanding that multilayer adsorption under conditions where we expect phases to consist of a normal gas or supercritical gas is unlikely, we can assume that maximizing the number of potential adsorption sites by maximizing the specific surface area of a prospective adsorbent is the initial strategy that needs to be pursued in developing an effective adsorbent for hydrogen. We have already seen schematically how an idealized carbon in graphitic form like activated carbon might be suitable to this end and how other carbons like aerogels behave similarly. Another class of materials that have been under consideration for gas adsorption technologies, initially for methane, are what have traditionally been referred to as coordination polymers⁶⁸ but what have recently come to be known as metal organic frameworks (or MOF's).

Given the varying nature of "surfaces" in MOF's, application of the type of "Chahine rule" behavior that we have seen in pure carbons where we might expect uptake to go as surface area was less certain. In graphitic carbons, we can take advantage of the center of graphitic hexagons as local potential sites for adsorbing molecular hydrogen, but MOF linkers tend to have a somewhat proportionally smaller number of hexagons per unit surface area. Because edge terminations in materials make up a large percentage of the surface area, we might expect slightly different dependencies insofar as surface area is concerned.

⁶⁸ R. Robson, Design and its limitations in the construction of bi- and poly-nuclear coordination complexes and coordination polymers (aka MOFs): a personal view, *Dalton Trans* (38), 5113–5131 (2008).

To this end, we did synthesize and investigate several coordination polymers in order to clarify our understanding of this class of materials. These included so-called MIL⁶⁹ structures, MIL-100 and MIL-101b and MOF-74⁷⁰. These materials were synthesized using recipes from the literature and isotherms from these materials are shown in Figure 29.

Our initial interest in MOF-74 came about as this material was reported to fall into the category of coordinatively unsaturated metal center (CUMC) materials where the Zn metal is essentially exposed. A strong correlation was suspected between this attribute and the sharp initial isotherm behavior. In collaboration with the group at NIST, we reported the first neutron scattering results from MOF-74, which demonstrated the largest surface density of adsorbed H₂ at 77 K in any framework structure studied to date at that time. Our results revealed the shortest intermolecular D₂-D₂ distance observed in a physisorption-based material, which we were aware of, without the application of pressure.

We will describe some of the synthesis procedure here as the procedures that were outlined in the references we used in an attempt to make the structure, have incorrect temperatures as part of their recipes.

MOF-74 samples were synthesized using previously published procedures^{70,71}. Typically, 1 g of Zn(NO₃)₂·6H₂O was mixed with 0.25 g of the organic linker (2,5 dihydroxyterephthalic acid) in 50 mL of dimethylformamide (DMF) and 2.5 mL of water. The mixture was stirred to dissolve the solid reactants, and the solution was sealed in a 100 mL autoclave and heated to 100 °C for 20 h. At the end of this heating cycle, the mixture was allowed to cool to 40 °C and was opened in air. Yellow crystals of MOF-74 were formed on the autoclave walls and base. If the solution is allowed to cool to room temperature over several hours, large orange crystals of an unidentified phase are formed. To minimize the formation of this unwanted secondary phase, the solution is filtered while the solution temperature is still 40 °C. After filtration, the remaining crystals were rinsed several times, first with DMF and then with methanol. In order to activate the MOF-74 crystals, the DMF guests within the porous structure must be exchanged with methanol molecules, which are more easily removed. This activation consists of immersing the crystals in methanol for approximately 5 to 6 days, over which time the methanol solution is changed two or three times. After this immersion step, the sample was filtered and washed with methanol and then heated to 200 °C under vacuum for at least 20 h to remove the remaining methanol from the pores. This procedure completed the activation process. The powder product was characterized using X-ray powder diffraction. The experimental pattern was compared to a simulated pattern using a previously published structure, and the experimental data matched the theoretical patterns.

Of particular note in this comparison is the fact that the MOF-74 material shows uptakes that are substantially higher than we would expect on the basis of surface area alone, while the MIL samples show a somewhat weaker dependence on surface area than expected. We have defined a new parameter of relevance to the Hydrogen program, the surface packing density or SPD which we define as where “mass fraction(*T*)” is the excess mass adsorption of H₂ saturated at temperature *T* and *S* is the nitrogen BET surface area. At 77 K, hydrogen molecules are typically adsorbed as a monolayer on the material surface⁷².

⁶⁹ Material Institut Lavoisier

⁷⁰ Rosi, N. L.; Kim, J.; Eddaoudi, M.; Chen, B., O' Keeffe, M.; Yaghi, O. M. *J. Am. Chem. Soc.* **2005**, *127*, 1504-1518.

⁷¹ Rowsell, J. L. C.; Yaghi, O. M. *J. Am. Chem. Soc.* **2006**, *128*, 1304-1315.

⁷² Schlögl, L.; Züttel, A. *Nature* **2001**, *414*, 353-358.

Although the surface excess adsorption is the additional hydrogen adsorbed on the surface over what the real gas law would yield for the volume displaced by the adsorbate, given the low density of hydrogen in the gas phase, our definition of SPD at 77 K should be a good approximation to the monolayer surface density

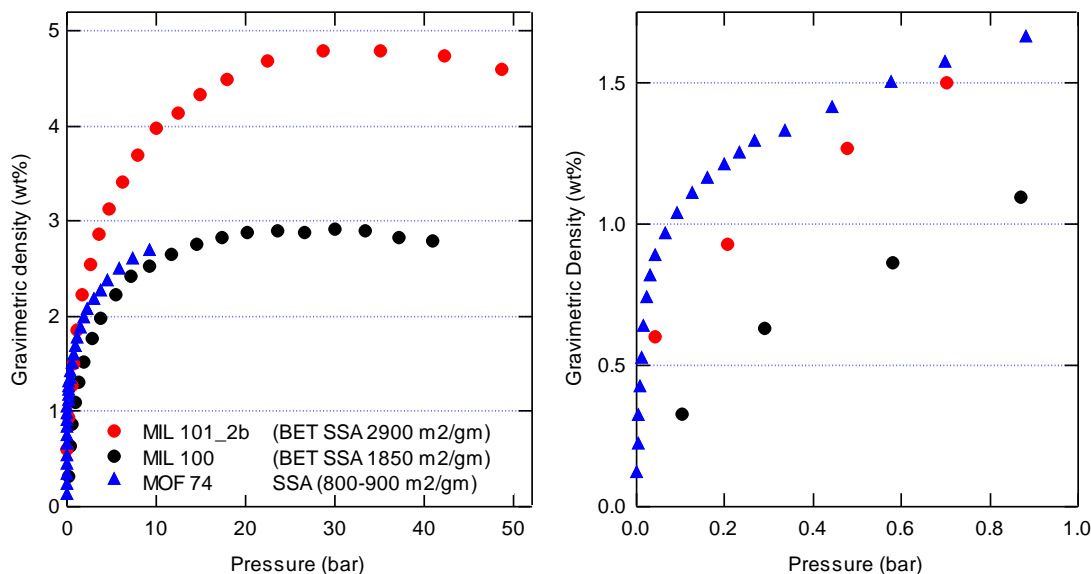


Figure 29. Complete(left) and low pressure(right) isotherms for MIL 100, MIL 101 and a MOF-74. The low pressure data reveals differences in the initial slope indicating differences in the Henry's law adsorption enthalpy.

$$\text{SPD}(T) = \frac{\text{mass fraction}(T)}{S}$$

of adsorbed H₂. Therefore, the SPD approximates the mass of hydrogen adsorbed per unit area, and is not a function of the mass of host materials. Thus, it is an indicator of surface adsorption properties. Because the maximum gravimetric adsorption is the product of SPD and S , ideally both quantities should be large. According to the above definition, the experimental surface packing density of activated carbons at 77 K, SPD_{AC} , is $2.0 \times 10^{-5} \text{ g/m}^2$. By use of the nearest neighbor distance of solid H₂ (3.8 Å), the calculated surface packing density for triangular packing in a plane, $\text{SPD}_{\text{H}_2}(Th)$, is $2.8 \times 10^{-5} \text{ g/m}^2$.

High-resolution hydrogen adsorption/desorption measurements were performed with a volumetric Sieverts apparatus¹⁰ to pressures up to 30 bar. Samples were outgassed prior to measurements. A pretreatment was used that consisted of heating the sample under vacuum to 120 °C until outgassing was completed and a vacuum pressure of $\sim 10^{-4} \text{ Pa}$ was attained. After this treatment, the sample reactor was immersed in liquid nitrogen or liquid argon for data acquisition. The evolution of the isosteric heat of adsorption versus mass coverage was determined from Equation 13, using two adsorption isotherms at temperatures of 77 and 87 K.

Neutron diffraction studies were performed at NIST and presumably are detailed in their report. We will cover some of the relevant points here however.

Neutron powder diffraction experiments were performed to identify the D₂ adsorption sites (which closely reflect the adsorption sites of H₂^{73,74,75,76,77}). All diffraction data were obtained at 4 K and analyzed using standard Rietveld refinement techniques in conjunction with Fourier difference maps^{73,74,75,76,77}. **Figure 31** shows the superposition of the Fourier difference map and the crystal structure of MOF-74 with the red-yellow (gray-white) regions indicating the locations of D₂ sites 1 and 2. On the right side of **Figure 31** shows the projection of the four observed hydrogen adsorption sites along the *c*-axis. The adsorption sites are numbered 1-4, according to the order they are occupied. A decrease of binding strength results in adsorption sites that are further from the adsorbent surface.

The first three adsorption sites can be fully occupied at T ~ 30 K and zero pressure. By decreasing the temperature slowly to 15 K, the fourth site is fully populated. Both the direct metal interaction and the van der Waals attraction from the other atoms of the framework contribute to the overall binding strength and affect the adsorption enthalpy. Since the typical van der Waals attraction is not negligible compared to the binding strength at each metal site, if there is a correlation with the interaction distance, it could only be obtained after removing the contributions from the typical van der Waals attraction.

The second adsorption site is located above a triangle of oxygen atoms with a closest sorbate-sorbent distance of 3.1 Å. The third site is near the benzene ring with a closest distance to the framework atoms of 3.3 Å. The larger distances suggest that the H₂ binding of sites 2 and 3 are likely dominated by dispersive interactions. Although the diffraction measurements were performed at 4 K, the D₂-D₂ intermolecular spacings between the first three adsorption sites shed light on the relatively large SPD in MOF-74 at 77 K. The first three sites cover the entire surface without applying any vapor pressure at 30 K. Additional adsorbed D₂ begins to form a second layer below the condensation temperature.

Comparing the maximum value of the surface excess adsorption of 2.8 wt % at 77 K to the maximum of 3.6 wt % H₂ achievable with the complete population of the first three adsorption sites, we should expect sites 1-3 to dominate the adsorption/desorption properties at 77 K. The sequence of adsorption site occupation shows that the first site has a relatively large binding energy due to the direct interaction of H₂ with the CUMCs.

Temperature dependent inelastic neutron scattering (INS) experiments further indicate that this binding energy difference is very large and consistent with the sharp decrease of the adsorption enthalpy curve at around 1 wt % (**Figure 30b**). We may reasonably conclude that ΔH for site 1 is ~8.8 kJ/mol and ΔH for site 2 is ~5 kJ/mol. ΔH for site 3 cannot be estimated using our current data.

⁷³ Dinca, M.; Dailly, A.; Liu, Y.; Brown, C. M.; Neumann, D. A.; Long, J. R. *J. Am. Chem. Soc.* **2006**, *128*, 16876-16883.

⁷⁴ Dinca, M.; Han, W. S.; Liu, Y.; Dailly, A.; Brown, C. M.; Long, J. R. *Angew. Chem., Int. Ed.* **2007**, *46*, 1419-1422.

⁷⁵ Peterson, V. K.; Liu, Y.; Brown, C. M.; Kepert, C. J. *J. Am. Chem. Soc.* **2006**, *128*, 15578-15579.

⁷⁶ Yildirim, T.; Hartman, M. R. *Phys. Rev. Lett.* **2005**, *95*, 215504.

⁷⁷ Hartman, R. M.; Peterson, V. K.; Liu, Y.; Kaye, S. S.; Long, J. R. *Chem. Mater.* **2006**, *18*, 3221-3224.

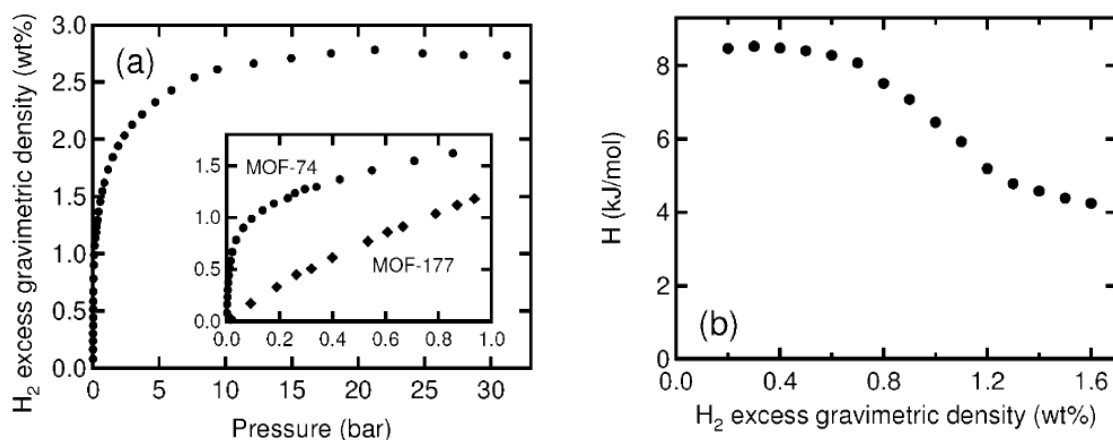


Figure 30. H_2 Isotherm measurements of MOF-74. (a) The H_2 adsorption/desorption isotherms at 77 K. The inset shows the comparison of H_2 adsorption isotherms for MOF-74 and MOF-177. (b) The H_2 adsorption enthalpy of MOF-74 is shown with the initial H_2 adsorption enthalpy of 8.8 kJ/mol.

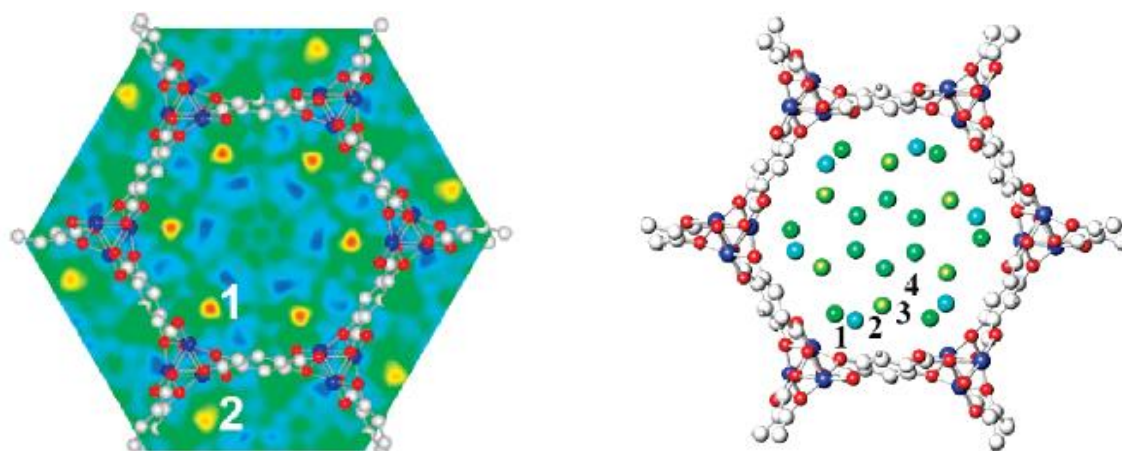


Figure 31. D_2 adsorption sites in MOF-74 at 4.2 D_2 :Zn. On left are suppositions of Fourier difference map together with the crystal structure of MOF-74 projected down the c axis. The red-yellow regions (gray with white halo indicated by 1 and 2) indicate the high scattering regions of the first two adsorption sites. On the right are the four D_2 adsorption sites identified by neutron powder diffraction (labeled 1-4, spheres of green (gray) and light blue (light gray)).

The D_2 - D_2 intermolecular distances in the first layer vary from ~ 2.85 to 4.2 Å with an average of 3.4 Å⁷⁸, which is shorter than the 3.6 Å distance found for solid D_2 . The shortest distance from the site 1 to site 3 is 2.85 Å and from site 1 to site 2 is 2.9 Å. These close distances between adsorption sites explain the large SPD of MOF-74 at 77 K. The two shortest distances occur from site 1, directly above the Zn^{2+} ion, to sites 2 and 3,

⁷⁸ Due to interactions among D_2 molecules, the D_2 - D_2 distances vary slightly depending upon the amount of loaded gas. The average distance among D_2 molecules for the first three adsorption sites are calculated based on the refined data of the 4.2 D_2 :Zn case. The mean distance is calculated as the total average over the four nearest-neighbor distances of the first three adsorption sites.

respectively. Given the high density of Zn^{2+} , it is reasonable to conclude that the large SPD for hydrogen in MOF-74 is at least partly induced by the Zn^{2+} CUMCs though additional contributions may come from favorable geometrical considerations. The adsorbed D_2 molecules form a one-dimensional network as shown in Figure 32. The one-dimensional nanoscale tubelike structure of D_2/H_2 molecules may present a model system for studies of low-dimensional quantum objects.

In order to assess the value of this analysis more completely, the experimental SPD's of different framework structures⁷⁹, including our results for MOF-74, are summarized as a function of BET surface area in Figure 33. While S measured by the N_2 BET method at 77 K is not a true surface area, a recent Monte Carlo simulation has indicated that the BET surface is a good estimation of the real surface area for at least a few MOFs. For many framework structures, hydrogen packs less efficiently than it does when adsorbed on typical carbons, while each of Mn-BTT, Cu-BTT, MOF-74, Cu_2 (bptc), Cu_2 (tptc), and Cu_2 (qptc) has a larger experimental SPD than SPD_{AC} , with the present results for MOF-74 showing the highest SPD. Previous work has demonstrated that Mn-BTT and Cu-BTT have CUMCs that strongly bind H_2 ^{73,74}. Similarly, the hydrogen adsorption sites in HKUST-1 have been carefully investigated by neutron powder diffraction⁷⁵ and the strongest binding site is found to be due to coordinatively unsaturated Cu^{2+} . While there are no reports of hydrogen adsorption sites yet in Cu_2 (bptc), Cu_2 (tptc), and Cu_2 (qptc), these three materials have Cu^{2+} sites with bound solvent molecules⁸⁰ before activation. Thus, it is likely that if the solvent molecules are removed by sample activation, the open Cu^{2+} centers would have high adsorption enthalpies for H_2 similar to HKUST-1. Therefore, all seven MOFs displaying a SPD larger than SPD_{AC} in Figure 33 have, or likely have, CUMCs⁸¹. This strong correlation between exposed CUMCs and the large SPD in framework structures shows that CUMC's not only enhance the H_2 binding energy but also increase the SPD. A plot of SPD as a function of Langmuir surface area demonstrates a similar correlation.

Summary of MOF analysis

There is a strong correlation between exposed CUMCs in framework structures and larger associated SPDs. These observations provide an avenue to improve the gravimetric H_2 uptake by increasing the SPD. The study of MOF-74 with neutron powder diffraction alongside isotherm measurements show that H_2 adsorbed on the MOF-74 surface has a higher surface density at 77 K than that of solid H_2 at ~ 4 K and zero pressure. In fact, the intermolecular hydrogen distances between sites 1 and 2 as well as between sites 1 and 3 in MOF-74 approach the expected minimum *mean hydrogen distance*. This offers the prospect that a material with a larger surface area can be synthesized with a similarly large SPD that meets engineering requirements for a hydrogen storage system.

⁷⁹ Except for the MOF-74 data presented here, data for other materials were taken from literature results. The data for IRMOF-1, MOF-177, IRMOF-20, IRMOF-11, IRMOF-6, and HKUST-1 are from Wong-Foy, A. G.; Matzger, A. J.; Yaghi, O. M. *J. Am. Chem. Soc.* **2006**, *128*, 3494-3495. The data for Cu-BTT and Mn-BTT are from refs 73 and 74. The data for Cu_2 (bptc), Cu_2 (tptc), and Cu_2 (qptc) are from 80. (Ligand nomenclature: HKUST-1, $\text{Cu}_3(1,3,5\text{-benzenetricarboxylate})_2$; BTT, 1,3,5-benzenetristetrazolate; Cu-BTT, $\text{HCu}[(\text{Cu}_4\text{Cl})_3(\text{BTT})_8] \cdot 3.5\text{HCl}$; Mn-BTT, $\text{Mn}_3[(\text{Mn}_4\text{Cl})_3(\text{BTT})_8(\text{CH}_3\text{OH})_{10}]_2$; bptc, biphenyl-3,3':5,5'-tetracarboxylate; tptc, terphenyl-3,3':5,5''-tetracarboxylate; qptc, quaterphenyl-3,3'':5,5'''-tetracarboxylate.)

⁸⁰ Lin, X.; Jia, J.; Zhao, X.; Thomas, K. M.; Blake, A. J.; Walker, G. S.; Champness, N. R.; Hubberstey, P.; Schroder, M. *Angew. Chem.* **2006**, *118*, 1-7.

⁸¹ It should be noted that HKUST-1 also has CUMCs, yet the SPD is only comparable to other MOFs without CUMCs. Detailed study of the H_2 adsorption sites (ref 75) shows that the volume of the small cage in HKUST-1 is not efficiently used because the small pore can accommodate only one H_2 . The wasted volume in the small cage largely explains the low SPD.

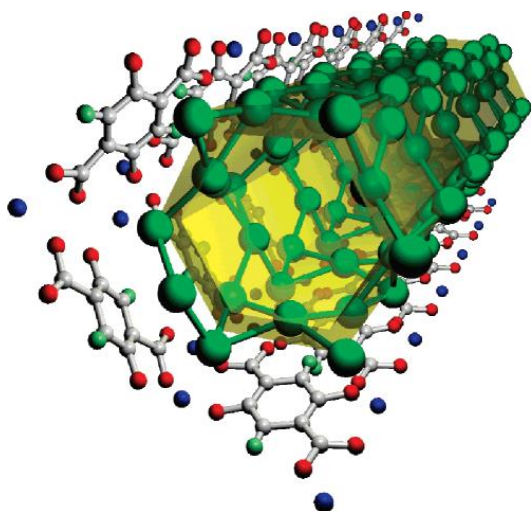


Figure 32. One-dimensional nanoscale tubelike structure formed from adsorbed D_2 . D_2 molecules (large green (gray) balls) adsorbed in MOF-74 form a one-dimensional nanoscale tubelike structure. (Only the first three adsorption sites are shown.) Molecules of deuterium are connected if the distance between D_2 molecules is less than 3.65 Å.

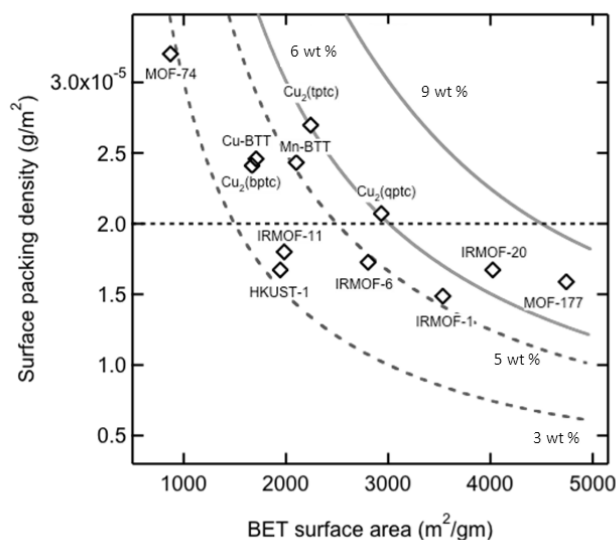


Figure 33. The H_2 surface packing density (SPD) as a function of N_2 BET surface area. The MOFs with CUMCs, in general, show larger SPD compared to those without CUMCs. The horizontal dashed line shows the SPD for typical carbon material, where every 500 m^2/g of N_2 BET surface area can adsorb 1 wt% of H_2 . Solid green curves show the lines for gravimetric uptake of 6 and 9 wt%.

Constant isosteric heats and Intercalated Graphites

The paradigms for desired isotherm behavior are still intercalated graphites. These materials show typical Type I or Langmuir behavior. Unlike virtually every other adsorbent we have studied or gathered data, we had suspected that intercalated graphites would reach the same maximum uptake value at any temperature, given a high enough pressure. While we recognized from the outset that materials of this type might fall short of DOE gravimetric density requirements, the need to develop a higher temperature adsorbent with a high constant isosteric heat would rely on strategies learned from initial work on these systems.

Graphite intercalation compounds (GICs) are a unique class of lamellar materials formed by the insertion of atomic or molecular guests between the layer planes of the host graphite. Electrical, thermal and magnetic properties can be varied by intercalation, making these materials interesting technologically. Graphite intercalation compounds exist for all alkali metals, but only the K, Rb, and Cs compounds are known to adsorb hydrogen. The maximum adsorption capacity of these materials is typically only around 1 wt%, but their high degree of structural ordering makes them a model system for studying hydrogen adsorption in a carbon nanostructure. They share many structural and chemical similarities to chemically-modified carbon slit-pore structures, but are more readily synthesized. Due to the attractiveness of potassium as a lightweight dopant for carbon adsorbents, potassium intercalated graphite was the focus of our initial work.

Alkali metal GICs were first prepared by Fredenhagen and co-workers in the 1920's with the compositions C_8M and $C_{16}M$ ⁸². Further studies were carried out on the potassium compound in the 1950's by Herold, who developed a two-zone, vapor-phase synthesis technique where the potassium melt was kept at a constant temperature (250 °C) while the graphite temperature was varied (250 °C to 600 °C)⁸³. Stoichiometric compounds of KC_8 and KC_{24} are visible as plateaus in the potassium-graphite isobar illustrated in Figure 34.

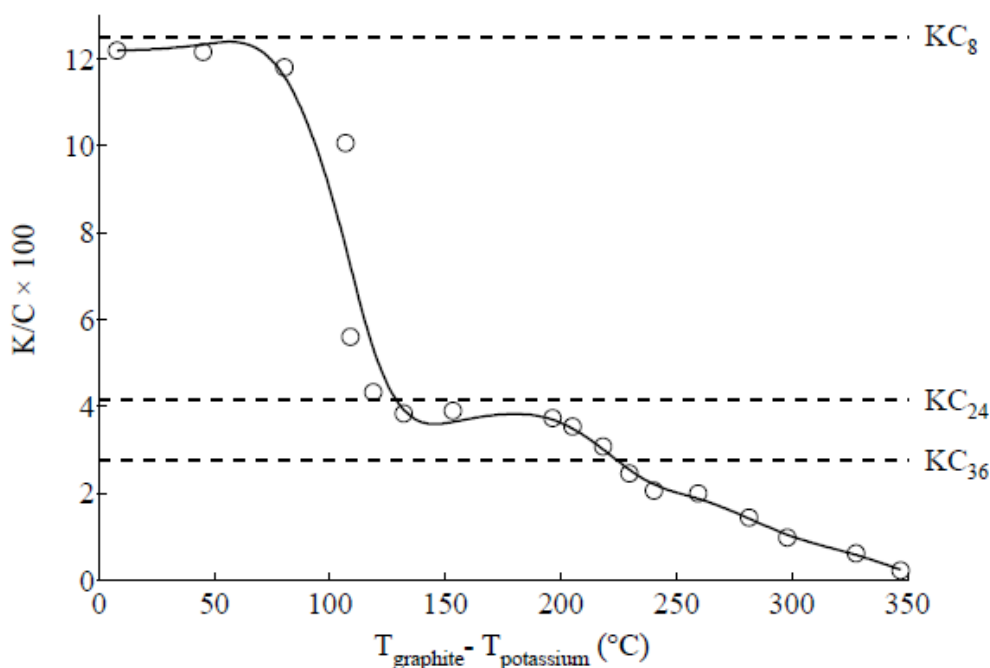


Figure 34. Composition of the potassium-graphite system based on the temperature difference between the graphite host and potassium vapor.

Structural studies of staging in potassium GICs were performed by Rudorff and Schulze⁸⁴. Discrete compositions of MC_8 , MC_{24} , and MC_{36} were linked to the formation of stage 1, stage

⁸² K. Fredenhagen and G. Cadenbach. Die Bindung von Kalium durch Kohlensto_. Z. anorg. Chem., 158(1):249-263, 1926.

⁸³ A. Herold. Recherches sur les composés d'insertion du graphite. Bull. Soc. Chim. Fr, 187:999-1004, 1955.

⁸⁴ W. Rudorff and E. Schulze. Über Alkaligraphitverbindungen. Z. anorg. Chem., 277(3-4):156-171, 1954.

2, and stage 3 intercalation compounds, respectively. The staging index, n , of the GIC indicates that the intercalant layer is found between every n th pair of host graphite planes. The stacking sequences in the alkali-metal GIC's were further characterized by Perry and Nixon in the 1960's⁸⁵. In the early 1960's, Saehr and Herold discovered that KC_8 chemisorbs hydrogen at elevated temperatures up to maximum values of about $\text{KC}_8\text{H}_{0.67}$ ⁸⁶. Chemisorption was also noted for RbC_8 and KC_{24} , but not for CsC_8 . Physisorption of H_2 by the stage 2 compounds of K, Rb, and Cs at low temperatures was discovered by Tamaru and co-workers in the early 1970's⁸⁷. These measurements were reproduced by a number of subsequent studies^{88,89}. The first inelastic neutron scattering studies of H_2 adsorbed in the stage-2 alkali metals compounds were performed by White and co-workers in the early 1980's⁹⁰. Low-energy "rotational tunneling" peaks observed in the spectra indicated that the adsorbed hydrogen was in a strong anisotropic field. They were explained in terms of a one-dimensional hindered diatomic rotor model^{91,92}. By the late 1980's, a substantial body of research existed on hydrogen-alkali-metal graphite intercalation systems^{93,94}. Interest in the area dwindled during the 1990's, as reflected in the small number of publications during the period. However with the emergence of hydrogen storage materials as a major topic of research, there has been a resurgence of interest in the hydrogen adsorption properties of the alkali-metal GICs.

Stacking sequence

Potassium GICs are formed by inserting potassium atoms into the galleries between the host graphitic layers. There are two competing forces in this system. First, the K atoms want to sit at the hexagon centers due to the strong graphite corrugation potential. This would cause the opposing basal planes to overlap exactly in an A|A sequence, where the vertical bar refers to the potassium layer. Second, the host graphite planes want to form a staggered sequence, ABAB, where half the carbon atoms in a given plane sit over the hexagon centers of the adjacent planes. It is the competition between these two driving forces that leads to the formation of discrete GIC stages. At low metal concentrations like KC_{24} and KC_{36} , it is apparently energetically favorable for metal layers to only occupy every 2nd and 3rd graphite gallery, respectively. For this reason, KC_{24} and KC_{36} are called the stage-2 and stage-3 compounds. The non-intercalated layers can maintain a staggered AB sequence, while the intercalated layers have an A|A sequence. If the potassium concentration is increased further, the system will eventually adopt a KC_8 stoichiometry, where the potassium atoms occupy every interlayer gallery in a close-packed 2×2 registered structure. The actual concentration of potassium within the GIC is determined by

⁸⁵ D. E. Nixon and G. S. Parry. Formation and structure of the potassium graphites. *Brit. J. Appl. Phys. (J. Phys. D.)*, 1:291-299, 1968.

⁸⁶ A. Herold and D. Saehr. Effects of hydrogen on insertion compounds of graphite with alkali metals. *Compt. rend.*, 250:545, 1960.

⁸⁷ K. Watanabe, T. Kondow, M. Soma, T. Onishi, and K. Tamaru. Molecular-sieve type sorption on alkali graphite intercalation compounds. *Proc. R. Soc. London, Ser. A*, 333:51-67, 1973.

⁸⁸ P. Lagrange, D. Guerard, J. F. Mareche, and A. Herold. Hydrogen storage and isotopic protium-deuterium exchange in graphite-potassium intercalation compounds. *Journal of the Less-Common Metals*, 131:371-378, 1987.

⁸⁹ T. Terai and Y. Takahashi. Formulation of isotherms for low-temperature absorption of H_2 and D_2 on KC_{24} prepared from natural graphite. *Synth. Met.*, 34:329-334, 1989.

⁹⁰ J. P. Beau-Is, T. Crowley, T. Rayment, R. K. Thomas, and J. W. White. Tunnelling of hydrogen in alkali metal intercalation compounds. *Molecular Physics*, 44(6):1257-1269, 1981.

⁹¹ L. Pauling. The rotational motion of molecules in crystals. *Physical Review*, 36(3):430-443, 1930.

⁹² T. E. Stern. The symmetric spherical oscillator, and the rotational motion of homopolar molecules in crystals. *Proc. R. Soc. London, Ser. A*, 130(815):551-557, 1931.

⁹³ S. A. Solin and H. Zabel. The physics of ternary graphite intercalation compounds. *Advances in Physics*, 37(2):87-254, 1988.

⁹⁴ T. Enoki, S. Miyajima, M. Sano, and H. Inokuchi. Hydrogen-alkali-metal-graphite ternary intercalation compounds. *J. Mater. Res.*, 5(2):435-466, 1990.

its relative chemical potential in the intercalated phase and in the vapor phase. By controlling the graphite temperature and the potassium vapor pressure (via the temperature of the melt), different potassium GIC stages can be synthesized (see **Figure 34**). The stage-1 compound has an orthorhombic symmetry with a known stacking sequence of $A\alpha A\beta A\gamma A\delta A$ ⁸⁴. Unfortunately, the long-range stacking sequences for the stage-2 (and higher) GICs are not as well characterized. Nixon and Perry suggested the following⁸⁵:

stage 4 ABAB|BCBC|CACA|
stage 3 ABA|ACA|A
stage 2 AB|BC|CA|A

An *in situ* X-ray diffraction study of the potassium GIC was actually able to identify stages 1 to 7, observing no evidence of microscopic mixing of the different stages⁹⁵. The nominal stacking sequence of KC_{24} is illustrated in Figure 35b, where the arrow from A to B indicates how the plane “A” is shifted with respect to the plane “B”. When potassium is inserted into the host graphite, the interlayer spacing expands from 3.35 Å to 5.40 Å in the potassium-containing galleries, as indicated in Figure 35a. The unintercalated galleries remain at 3.35 Å.

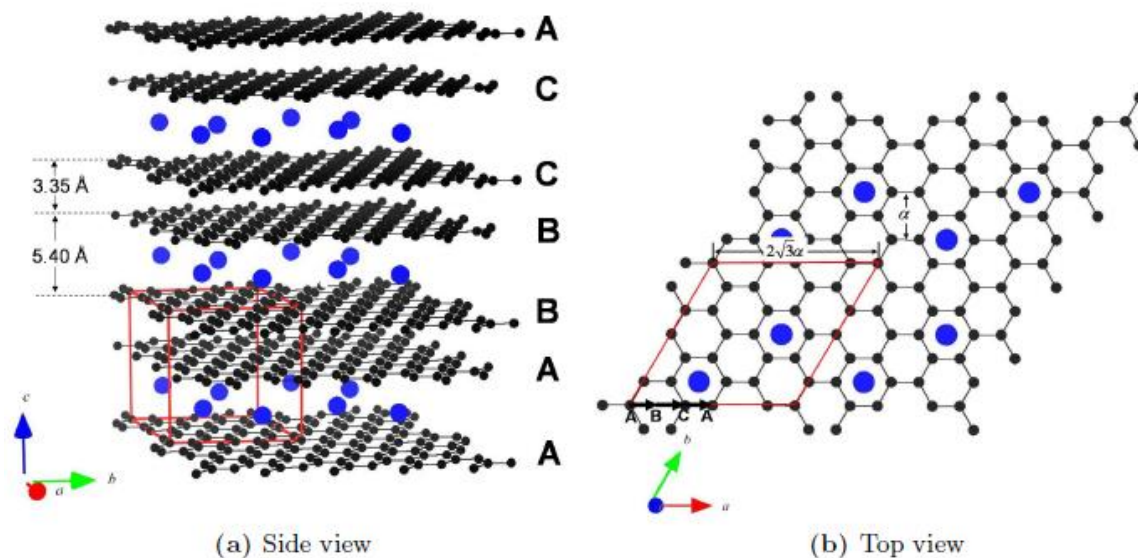


Figure 35. Structure of KC_{24} . (a) The A|AB|BC|CA stacking sequence. (b) Possible in-plane potassium structure. Arrows from A→B→C describe the relative positions of the layer planes in the stacking sequence.

In-plane potassium structure

At room temperature, the potassium atoms are disordered within the graphite galleries and are often described in terms of a two-dimensional liquid⁹⁶. A series of low-temperature

⁹⁵ R. Nishitani, Y. Uno, and H. Suematsu. In situ observation of staging in potassium graphite intercalation compounds. *Phys. Rev. B*, 27:6572, 1983.

⁹⁶ Y. Arai, Y. Shirikawa, and S. Tamaki. Structural properties of low dimensional potassium metal in intercalated graphite. *Journal of Non-Crystalline Solids*, 205-207:803-806, 1996.

phase transformations are known to occur in KC_{24} in which both the in-plane structure and stacking sequence assume long-range order^{97,98}. Unfortunately, the in-plane potassium structure has not been conclusively determined. While the stage-1 compound KC_8 has a commensurate (2×2) $R0^\circ$ in-plane structure, stage- n compounds (KC_{12n} for $n > 1$) have a lower potassium density in each layer. The potassium atoms are likely to be commensurate with the host graphite at low temperatures, but simple periodic registered structures are not consistent with X-ray data^{99,100}. Graphite has a honeycomb lattice structure, so the minimum-energy sites at the hexagon centers form a triangular lattice. It would make sense to populate this triangular lattice in a periodic fashion to give the correct KC_{24} stoichiometry. The $(\sqrt{12} \times \sqrt{12})$ $R30^\circ$ structure depicted in Figure 36a gives the correct 24:1 stoichiometry, but it is not consistent with X-ray diffraction patterns¹⁰⁰. Another idea is to take an incommensurate close-packed potassium monolayer with a liquid-like separation of roughly 6 Å, rotate the layer around the c-axis by an arbitrary angle, and then relax the potassium atoms into the nearest hexagon centers⁹⁹. This relaxed close-packed structure contains nearest-neighbor distances of $2a$, $\sqrt{7}a$ and $3a$ and has reasonable agreement with single-crystal X-ray data¹⁰⁰. An example is illustrated in Figure 36c. Unlike KC_{24} , the low-temperature in-planes structures of RbC_{24} and CsC_{24} are well described by a domain model^{101,102}. As illustrated in Figure 37, they contain locally commensurate $\sqrt{7} \times \sqrt{7}$ $R19.11^\circ$ patches surrounded by domain walls. The idealized $\sqrt{7} \times \sqrt{7}$ structure (see Figure 36b) has been the basis of most *ab initio* studies of the $\text{H}_2/\text{KC}_{24}$ system^{103,104}. Unfortunately the $\sqrt{7} \times \sqrt{7}$ structure has a KC_{28} stoichiometry. In the domain model the boundary regions have a greater alkali metal density, causing the total stoichiometry to even out at about 24 to 1. However, the domain model with discommensurations has not been consistent with single-crystal diff structure, an analogue of the random lattice-gas model, is the most compelling structural model for the in-plane potassium arrangement.

Properties of potassium-intercalated graphite

Graphite is a semi-metal with a complex band structure. It has only about 10^{-4} charge carriers per carbon atom. Alkali metal GICs, like KC_{24} , are classified as donor compounds because the metal atoms donate charge to the graphite conduction band. This results in a large increase in both the in-plane conductivity (σ_a) and c-axis conductivity (σ_c). Due to the layered structure of GICs, there is also considerable anisotropy in the charge transport properties. For KC_{24} , the c-axis conductivity is about 24 times larger than for pristine graphite, and the anisotropy factor σ_a/σ_c is about 860¹⁰⁵. Partial charge transfer from potassium to the empty graphite bands appears to be experimentally established¹⁰⁶.

⁹⁷ J. B. Hastings, W. D. Ellenson, and J. E. Fischer. Phase transitions in potassium intercalated graphite: KC_{24} . *Physical Review Letters*, 42(23):1552, 1979.

⁹⁸ D. E. Nixon and G. S. Parry. Order-disorder transformation in potassium graphite. *Nature*, 216:909-910, 1967.

⁹⁹ S. B. DiCenzo. Relaxed incommensurate structure of the intercalant layer in higherstage graphite intercalation compounds. *Phys. Rev. B*, 26(10):5878-5881, 1982.

¹⁰⁰ F. Rousseaux, R. Moret, D. Guerard, and P. Lagrange. X-ray study of the liquid and solid phases of the alkali metals in KC_{24} and CsC_{24} -intercalated graphite single crystals. *Phys. Rev. B*, 42(1):725, 1990.

¹⁰¹ R. Clarke, J. N. Gray, H. Homma, and M. J. Winokur. Evidence for discommensurations in graphite intercalation compounds. *Phys. Rev. Lett.*, 47(19):1407, 1981.

¹⁰² G. R. S. Naylor and J. W. White. Structure of second-stage graphite-rubidium, C_{24}Rb . *J. Chem. Soc., Faraday Trans.*, 83:3447-3458, 1987.

¹⁰³ A. Lovell, F. Fernandez-Alonso, N. T. Skipper, K. Refson, S. M. Bennington, and S. F. Parker. Quantum delocalization of molecular hydrogen in alkali-graphite intercalates. *Phys. Rev. Lett.*, 101:126101, 2008.

¹⁰⁴ A. P. Smith, R. Benedek, F. R. Trouw, and L. H. Yang M. Minko. Quasi-twodimensional quantum states of H_2 in stage-2 Rb-intercalated graphite. *Phys. Rev. B*, 53(15):10187, 1996.

¹⁰⁵ J. J. Murray and A. R. Ubbelohde. Electronic properties of some synthetic metals derived from graphite. *Proc. Roy. Soc. A.*, 312:371-380, 1969.

¹⁰⁶ M. S. Dresselhaus and G. Dresselhaus. Intercalation compounds of graphite. *Advances in Physics*, 51(1):1-186, 2002.

Hydrogen physisorption in KC_{24} , RbC_{24} , and CsC_{24} has been previously investigated⁸⁷. The Li and Na compounds do not physisorb hydrogen because the widths of the metal-containing galleries are too small. Notably, KC_{24} has molecular sieving properties in which it adsorbs smaller molecules (e.g., hydrogen), but does not adsorb larger molecules (e.g. methane). Quantum sieving effects are also present in KC_{24} , in which D_2 is adsorbed preferentially over H_2 ⁸⁹. The hydrogen adsorption characteristics depend on the quality of the starting graphite. The best adsorption is obtained for high purity, natural flake crystalline graphite. As the amount of amorphous impurities in the starting graphite increases, the H_2 adsorption amount decreases¹⁰⁷. Hydrogen is adsorbed into the metal-containing layers of KC_{24} , forming a quasi-two dimensional binary solution with potassium. There is no evidence for anything other than a monolayer structure in which the potassium and H_2 are mixed. The potassium-containing layer expands from 5.4 Å to 5.6 Å following hydrogen adsorption. This is an interlayer expansion of almost 5 %, which is surprisingly

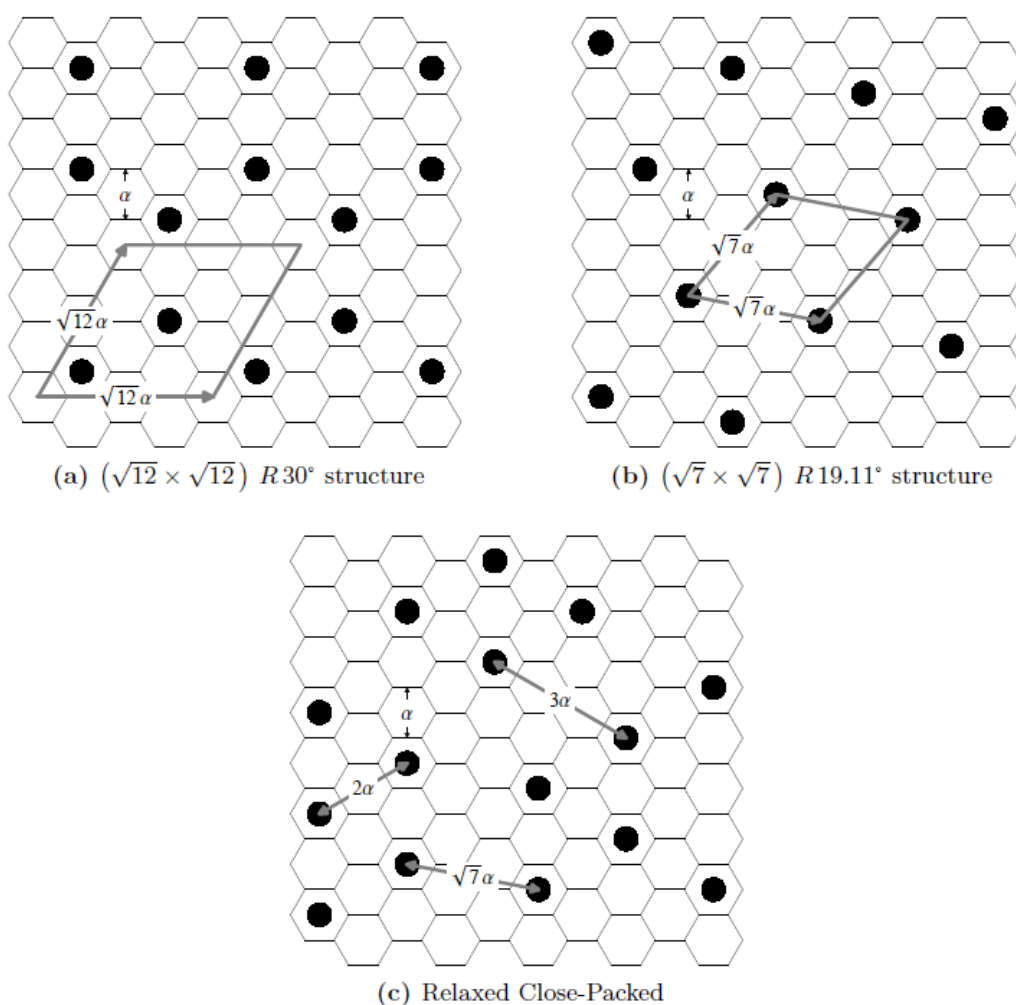


Figure 36. In-plane potassium structures in registry with the graphite host. The $(\sqrt{12} \times \sqrt{12})$ structure corresponds to a KC_{24} stoichiometry. The $(\sqrt{7} \times \sqrt{7})$ structure has a KC_{28} stoichiometry. The relaxed close-packed structure (adapted from Ref. [99]) consists of

¹⁰⁷ T. Terai and Y. Takahashi. Sorption of hydrogen isotopes on potassium-carbon intercalation compounds at low temperatures. *Synthetic metals*, 7:46-55, 1983.

a close-packed potassium layer which has been rotated in-plane and relaxed into the nearest hexagon centers.

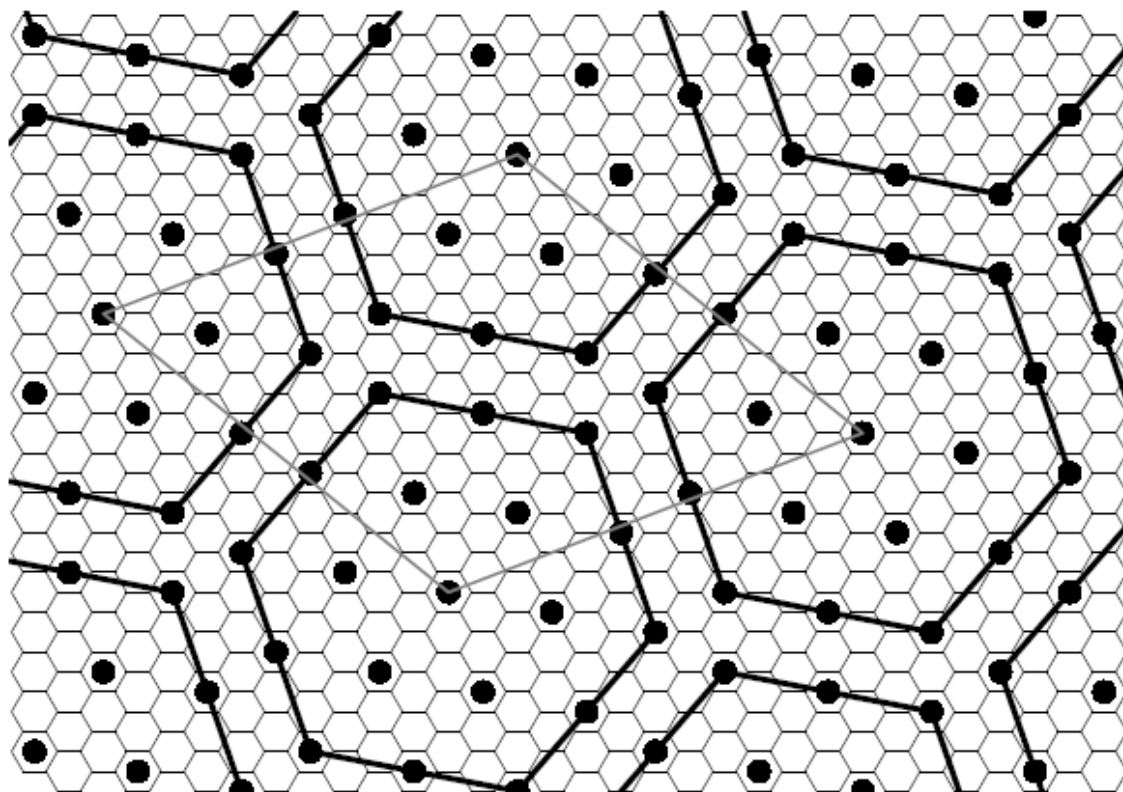


Figure 37. Domain model for CsC₂₄ in which $\sqrt{7} \times \sqrt{7}$ islands are separated by domain walls, or discommensurations. Adapted from Ref. [101].

large, but is still too small to support a bilayer or 30 tri-layer H₂-K-H₂ structure. There is also no evidence for H₂ dissociation during physisorption, as verified by a chromatographic analysis of an H₂/D₂ mixture⁸⁷. It is unclear whether the potassium superstructure is rigid, or whether it undergoes rearrangement after the introduction of hydrogen.

Interactions between hydrogen and KC₂₄ are likely to have both dispersion and electrostatic components. Charge transfer from potassium to graphite results in a strongly polarized potential field which can have significant charge-quadrupole and charge-induced dipole interactions with the adsorbed H₂ molecules. However, charge density surrounding the potassium atoms, and present in the bounding graphite layers, can also lead to an enhanced dispersion interaction with the H₂ molecule. Computational studies report an enhancement of the energy for the H₂ interaction with an alkali-doped graphene surface, due largely to the increased electron density on the surface surrounding the alkali impurity^{108,109}. The reported H₂ isosteric heat on KC₂₄ is 8.4 kJ mol⁻¹, about twice as large as for adsorption on bare graphite⁸⁷. It is also known that the in-plane resistivity in KC₂₄(H₂)_x is larger than in KC₂₄⁹⁴. This is explained by the observed *c*-axis expansion, which

¹⁰⁸ W.-Q. Deng, X. Xu, and W. A. Goddard. New alkali doped pillared carbon materials designed to achieve practical reversible hydrogen storage for transportation. *Phys. Rev. Lett.*, 92(16):166103, 2004.

¹⁰⁹ I. Cabria, M. J. Lopez, and J. A. Alonso. Enhancement of hydrogen physisorption on graphene and carbon nanotubes by Li doping. *J. Chem. Phys.*, 123:204721, 2005.

effectively reduces the in-plane carrier density. Charge back-donation from the conducting π bands to the hydrogen σ^* anti-bonding orbital seems unlikely and has not been conclusively demonstrated^{93,94}.

Synthesis of KC_{24} samples

Samples of KC_{24} used in this work were synthesized using a modified single-temperature zone technique. The starting materials were thermally purified natural flake graphite (Superior Graphite Co., 99.95-99.99% purity, 50 mesh) and potassium metal (Alfa Aesar, 99.9%). Since the starting graphite had already been subject to a high-temperature purification process, it was not necessary to pursue further purification. Stoichiometric amounts of graphite and potassium were weighed out inside an argon glovebox, transferred to a glass ampoule, and connected to a threaded glass vacuum valve with an O-ring sealed Teflon plug. The ampoule was then evacuated to 60 Torr and sealed with an oxygen torch. Samples were heated at 300 °C for 24 h to 48 h and shaken occasionally to ensure homogeneity. This last step was required to make sure that a homogenous stage-2 compound was produced instead of a mixture of stage-1 and higher-stage compounds. Samples produced with this method are pictured in Figure 38.

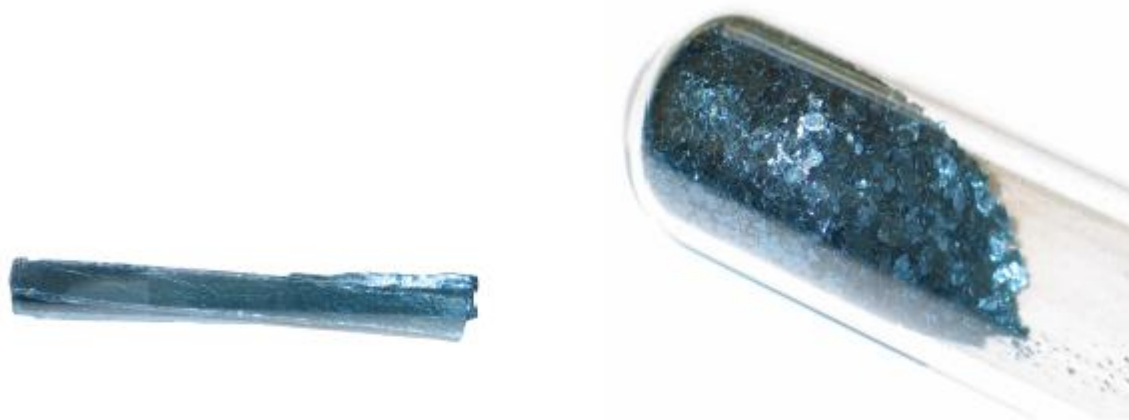


Figure 38. Samples of KC_{24} synthesized from Grafoil and natural flake graphite.

An additional KC_{24} sample was synthesized from a nuclear grade Grafoil® (99.5% graphite, 0.152 cm thickness) starting material used without further purification. The Grafoil-based sample had a stoichiometry of $KC_{21.7}$ and a helium density of 2.03(6) g ml⁻¹.

Characterization of KC_{24} samples

Powder X-ray diffraction

Powder X-ray diffraction (XRD) measurements verified the phase purity of KC_{24} samples synthesized from natural flake graphite. Rubidium and cesium GIC samples were also characterized. The XRD patterns were collected on a PANalytical X'pert PRO X'celerator diffractometer using Cu $K\alpha$ radiation ($\lambda = 1.5418$ Å). Samples were sealed within an argon atmosphere inside 1.5 mm ID glass capillary tubes using a low vapor pressure vacuum epoxy (TorrSeal, Varian Inc.), and mounted onto a specialized capillary goniometer. All measurements were collected at room temperature. An XRD pattern for KC_{24} is shown in Figure 39. The dominant features in the KC_{24} diffraction pattern are the [001] basal-plane

reflections, which indicate a repeat distance of 8.76 ± 0.02 Å. This gives an interlayer spacing of $d = 8.76 - 3.35 = 5.41$ Å, compared to the literature value of 5.40 Å⁸⁴. The higher order reflections follow the expected d_{001}/l spacing. Reflections with non-zero h and k are not visible in the powder diffraction pattern.

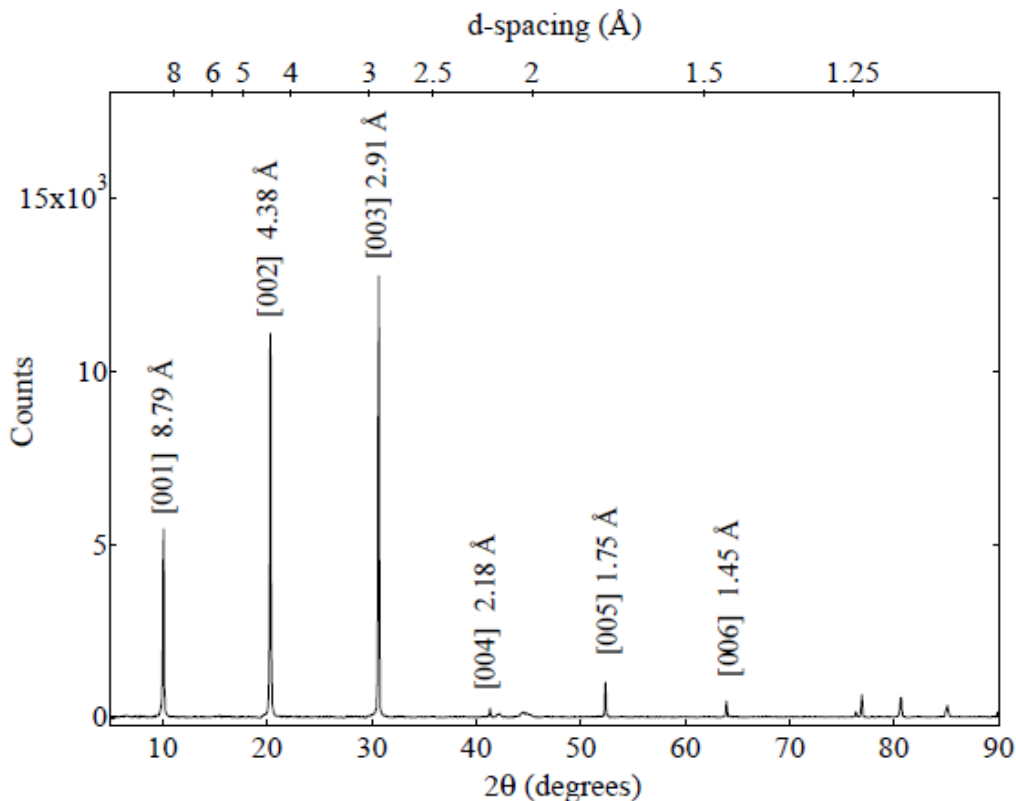


Figure 39. Powder XRD pattern of KC_{24} at room temperature.

For comparison, additional powder XRD patterns were collected for the stage-1 and stage-3 potassium GICs. This data is pictured in Figure 40. As desired, there are no Bragg peaks from either the stage-1 or stage-3 impurities in the prepared KC_{24} sample. The presence of a fine structure in the diffraction peaks of KC_8 and KC_{36} is very likely to be an artifact from the large diameter of the XRD capillary tubes. If two graphite flakes meet the same diffraction condition but are separated by a distance of 1.5 mm, the resulting diffraction peaks could easily be shifted by about 1° , producing the observed fine structure. Further, the capillary tubes were usually not aligned perfectly on the goniometer head (alignment was done “by eye”), creating a second, perhaps larger, source of error. Admittedly, using wide diameter capillary tubes are not the most accurate way to determine lattice parameters. Graphite flakes do not fit into smaller diameter capillary tubes without first being ground up (which would result in other artifacts). Nevertheless, powder XRD provided us the qualitative information we needed: that KC_{24} samples were synthesized correctly and were not contaminated by impurities from stage-1 or stage-3. Additional powder XRD patterns were collected for RbC_{24} and CsC_{24} samples, as illustrated in Figure 41. A summary of lattice parameter data for all of the synthesized alkali metal GIC’s is provided in **Table 5**.

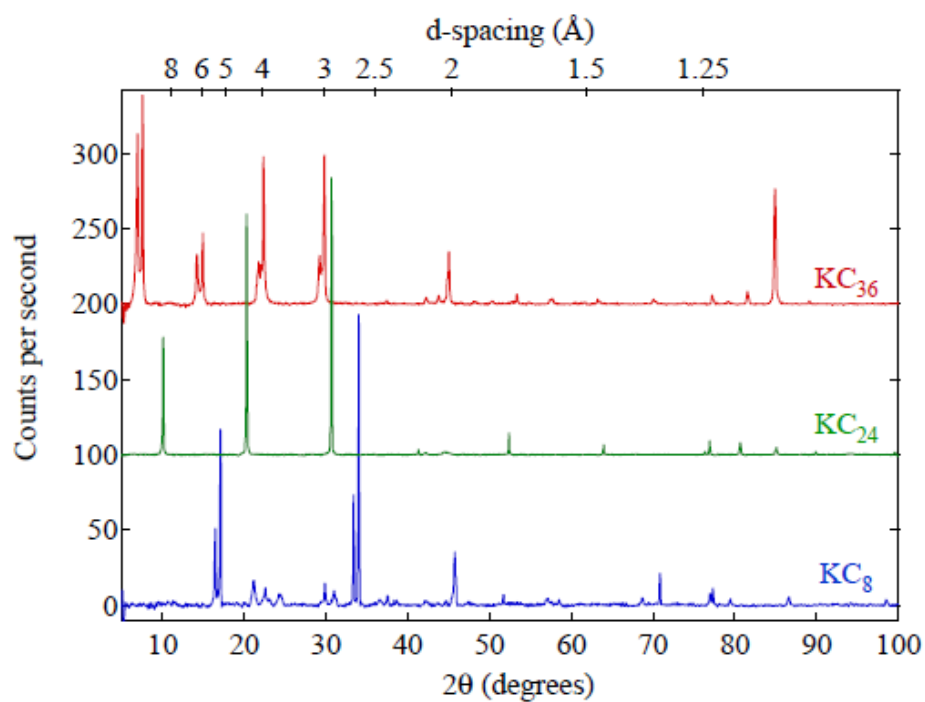


Figure 40. Comparison of the powder XRD patterns of stage-1, stage-2, and stage-3 potassium graphite intercalation compounds.

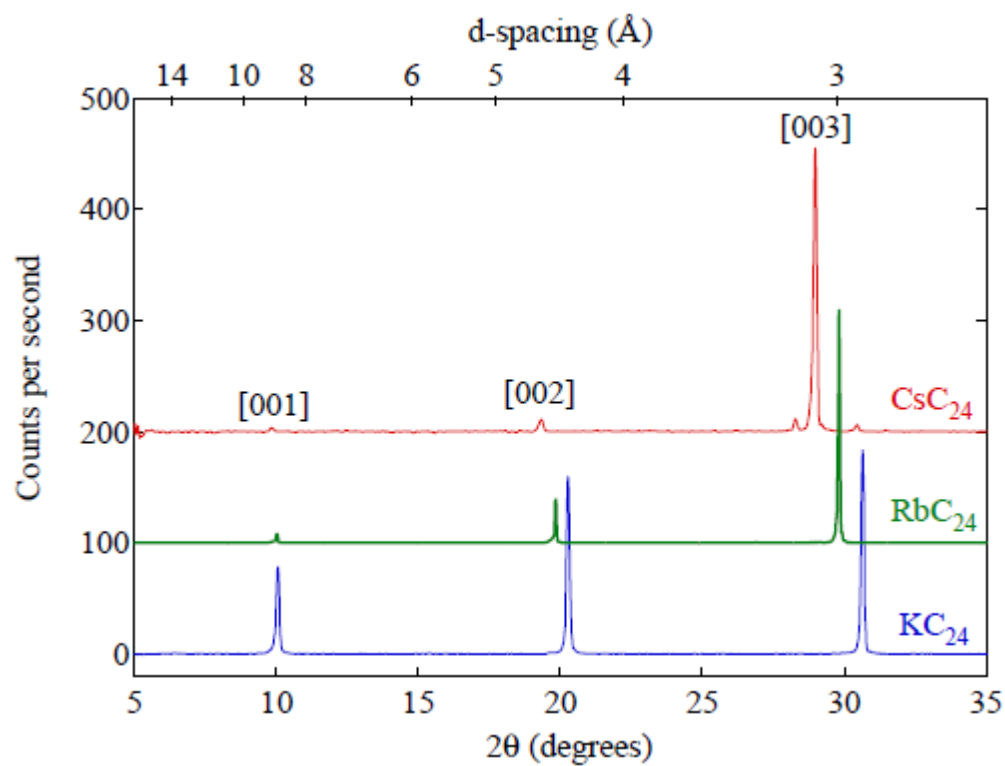


Figure 41. Comparison of the powder XRD patterns of KC_{24} , RbC_{24} , and CsC_{24} graphite intercalation compounds.

Table 5. Lattice parameters of synthesized graphite intercalation compounds

Sample	Lattice parameter(\AA) ¹¹⁰	Interlayer spacing (\AA) ¹¹¹
KC ₂₄	8.76 ± 0.02	5.41 ± 0.02
KC ₃₆	12.1 ± 0.30	5.40 ± 0.30
RbC ₂₄	8.95 ± 0.08	5.60 ± 0.08
CsC ₂₄	9.25 ± 0.05	5.90 ± 0.05

Raman spectroscopy

Raman spectroscopy was used as an alternative method of verifying the phase purity of prepared KC₂₄ samples. Measurements were collected on Renishaw M1000 Micro-Raman spectrometer, operating at 1 cm⁻¹ spectral resolution with a 514.5 nm argon laser. Samples were sealed in 1.5mm glass capillary tubes and data was collected at room temperature.

Data for KC₈, KC₂₄, and KC₃₆ are displayed in Figure 42. The peak at around 1600 cm⁻¹ is typically assigned to the E_{2g2} mode of graphite where the graphite layer is bounded by an intercalant layer on one side and a graphite layer on the other side¹¹². The peak near 1580 cm⁻¹ is typically assigned to an E_{2g2} mode where the layer is bounded on both sides by a graphite plane. As expected, the 1580 cm⁻¹ mode is present for pristine graphite and for KC₃₆ (which contains an intercalant layer in every third gallery). The 1600 cm⁻¹ mode is present as expected in both the KC₂₄ and KC₃₆ spectra, though it is unclear why it is also present in KC₈ (which contains an intercalant in every layer).

Hydrogen adsorption by graphite intercalation compounds

Understanding the thermodynamics of H₂ adsorption in chemically modified carbons remains a critical area of research. One reason is that physisorption of H₂ by carbons is significantly influenced by dispersion forces, which are notoriously difficult to calculate by first-principles methods. Further, most high-surface-area carbons have disordered structures which are difficult to model by simulations. As discussed earlier, graphite intercalation compounds provide a model system for systematically studying and assessing the effects of chemical modification and slit pore spacing on hydrogen adsorption thermodynamics.

In this section, measurements of the isosteric heat of H₂ adsorption in KC₂₄, RbC₂₄, and CsC₂₄ are presented. The effects of alkali-metal doping and graphite interlayer spacing on the adsorption enthalpy are discussed. The effect of adsorption kinetics is also investigated.

Hydrogen adsorption isotherms of KC₂₄

Hydrogen adsorption isotherms were measured for a 0.787 g sample of KC₂₄ synthesized

¹¹⁰ This c-axis lattice parameter gives the combined interlayer width of an AB|B sequence for a stage-2 compound (or an ABA|A sequence for a stage-3 compound). Values were averaged from the 001, 002, and 003 reflections.

¹¹¹ The interlayer spacing refers to the width of a metal-containing layer. It is equal to the c-axis lattice parameter minus the widths of the non-intercalated layers (e.g., 3.35_Å for a single non-intercalated layer.)

¹¹² K. Ichimura, E. Takamura, and M. Sano. Hydrogen in alkali-metal-graphite intercalation compounds. Synth. Met., 40:355-368, 1991.

from flake graphite. Loading was done in an argon glovebox so that the sample was not exposed to air at any stage of the experiment. Adsorption isotherms were collected at 77K

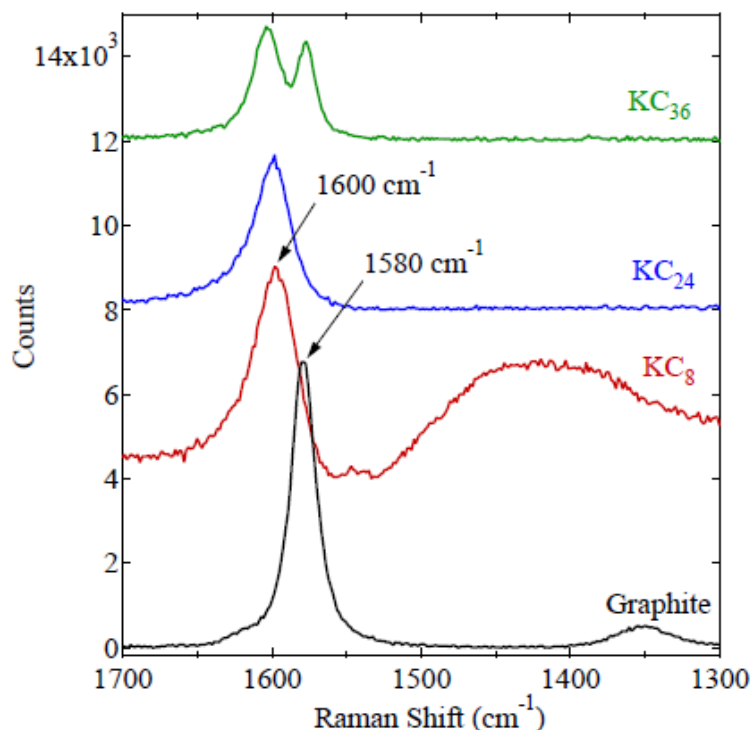


Figure 42. Raman scattering spectra of the potassium graphite intercalation compounds at room temperature. Measured scattering was from individual flakes.

and 87 K, and are displayed in Figure 43. The isotherms are steep, and a magnified view of the low-pressure region is provided in the inset. For this sample, the maximum hydrogen composition after adsorption was $\text{KC}_{24}(\text{H}_2)_{2.03}$, which is equivalent to 1.24 wt%. Both the 77K and 87K isotherms reached the same maximum capacity, which is not typically observed for supercritical adsorption in porous carbons¹¹³.

As explained further later, adsorption is kinetically limited at a hydrogen composition greater than $\text{KC}_{24}(\text{H}_2)_{1.6}$, which means that isotherm points in this region do not necessarily correspond to true equilibrium states. At 77 K and 87 K the hydrogen adsorption was fully reversible, and there was not any evidence of dissociation or reaction. Further, there was no reduction in adsorption capacity during three consecutive adsorption/desorption cycles at 77 K. Hydrogen adsorption at 195 K, however, was not completely reversible. When measured after 195 K isotherms, the 77K isotherms displayed a greatly reduced maximum adsorption capacity. It is very likely that the hydrogen chemically reacted with the potassium intercalant at 195 K⁹⁴. A full characterization of the reaction products was not pursued. It is known that KC_{24} chemisorbs a small amount of hydrogen at elevated temperatures to form a $\text{KC}_{24}\text{H}_{0.25}$ stoichiometry⁸⁶.

¹¹³ L. Zhou. Adsorption isotherms for the supercritical region. In Jozsef Toth, editor, *Adsorption: Theory, Modeling, and Analysis*, volume 107 of Surfactant Science Series, page 211. Marcel Dekker, Inc., 2002.

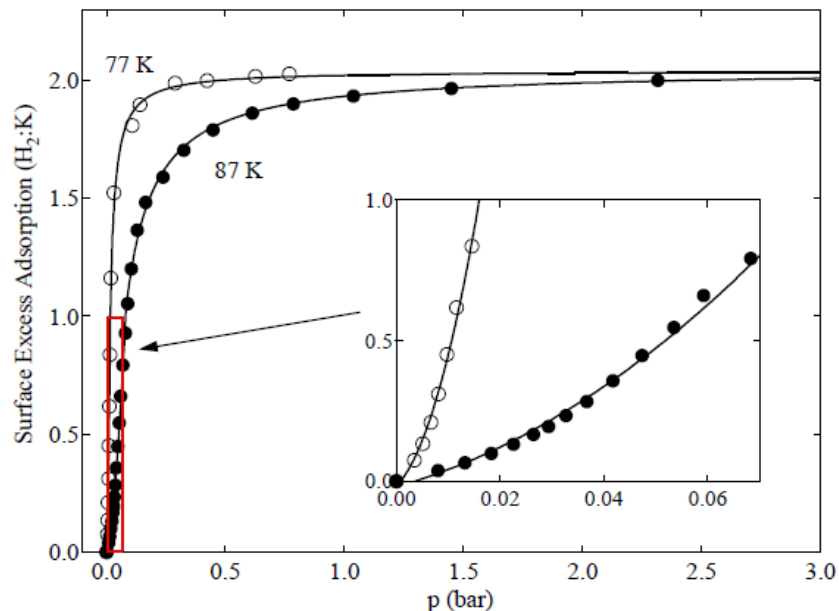


Figure 43. Hydrogen adsorption isotherms of KC_{24} at 77 K and 87 K. Inset shows a magnified view of the low-pressure portion of the isotherm contained within the red box. Lines are only a guide for the eye.

The isosteric heat for KC_{24} was calculated from fits of the virial-type thermal equation (Equation 14) to the isotherm data, following the procedure explained earlier. The isotherms, fits, and calculated isosteric heat are displayed in Figure 44. The zero coverage limit of the isosteric heat is 7.3 kJ mol^{-1} . The average value of the isosteric heat for $\text{KC}_{24}(\text{H}_2)_x$ in the range of $0.25 < x < 1.5$ is equal to 9.2 kJ mol^{-1} . The detailed shape of the isosteric heat is probably influenced by systematic instrument errors, among other things. The unique “S” shaped curve of the KC_{24} isotherms has been remarked upon previously¹¹⁴ and is thought to originate from the expansion of the c -axis spacing with H_2 adsorption. Energy losses from mechanical work associated with lattice expansion can be used to explain the anomalous positive slope of the isosteric heat.

Hydrogen adsorption isotherms were also measured for a Grafoil-based KC_{24} sample. The hydrogen adsorption behavior for this sample was markedly different than for the flake graphite sample. Measurements were only taken up to a pressure of about 1100 Torr, where the maximum hydrogen composition was $\text{KC}_{24}(\text{H}_2)_{1.82}$. Adsorption kinetics were much slower at all compositions compared to the flake graphite sample. The adsorption isotherms and calculated isosteric heat are displayed in Figure 45. The isosteric heat follows a physically intuitive pattern. There is an initial increase due to the energy losses in the lattice expansion, followed by a decrease due to the filling of the optimal adsorption sites. The zero coverage enthalpy is only 6.8 kJ mol^{-1} , while the average isosteric heat between $0.25 < x < 1.5$ is given by 8.5 kJ mol^{-1} . Interestingly, the average isosteric heat of the Grafoil sample is about 1 kJ mol^{-1} smaller than that of the flake graphite sample. The Grafoil used for the synthesis probably had a lower purity than the natural flake graphite. It

¹¹⁴ K. Watanabe, T. Kondow, M. Soma, T. Onishi, and K. Tamaru. Molecular-sieve type sorption on alkali graphite intercalation compounds. *Proc. R. Soc. London, Ser. A*, 333:51-67, 1973.

is possible that surface impurities may have hindered the hydrogen adsorption. Flake graphite GIC samples were used for all future experimental work.

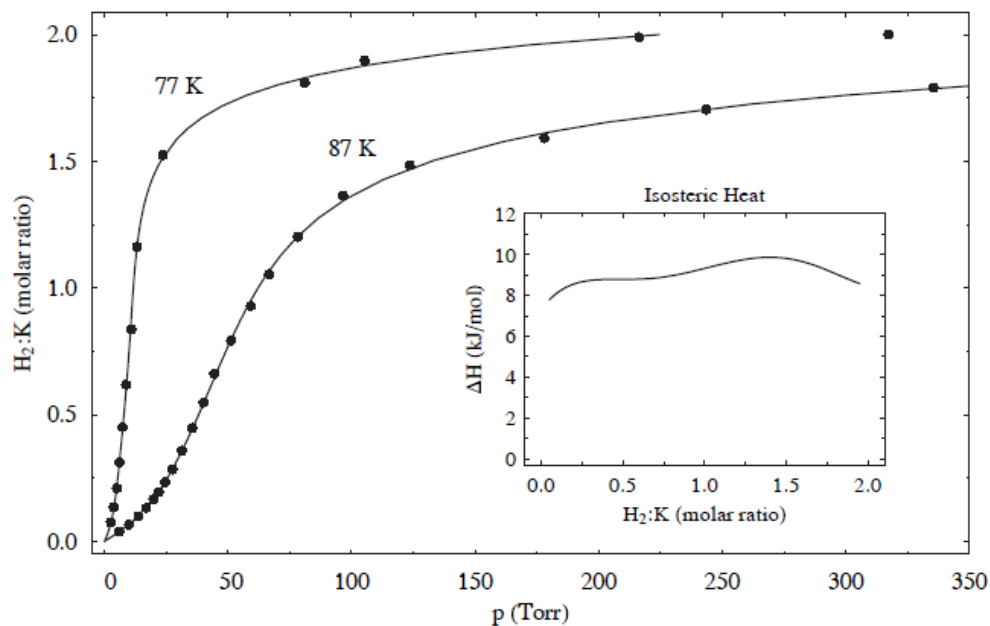


Figure 44. Adsorption isotherms of KC_{24} at 77K and 87K fitted to a virial-type thermal equation. Inset: Isosteric heat as a function of adsorption amount.

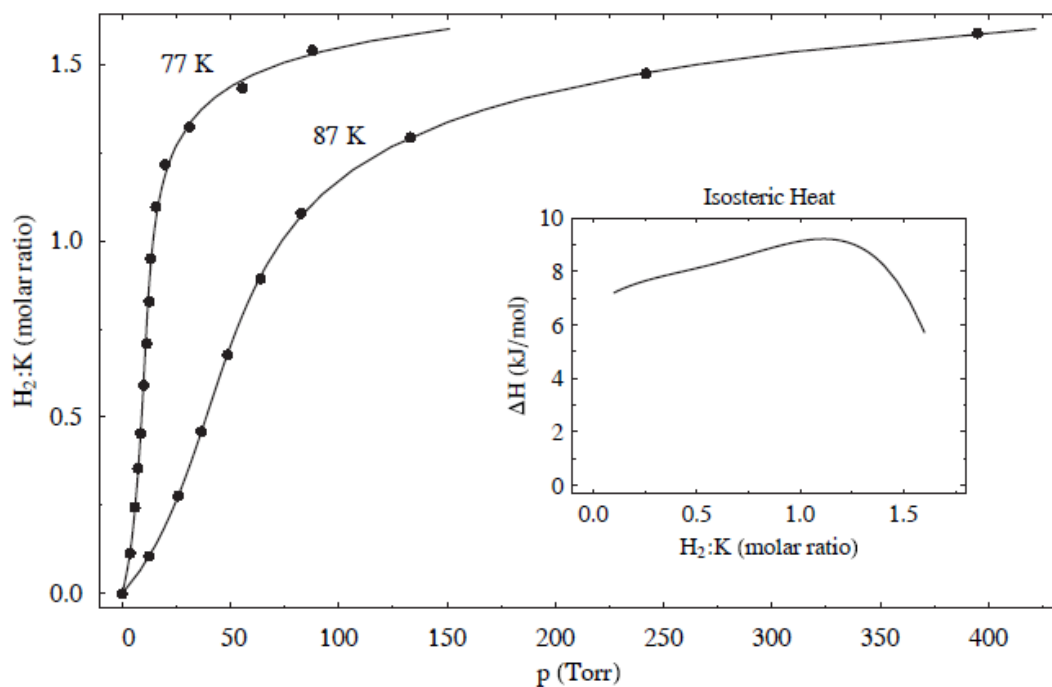


Figure 45. Adsorption isotherms of Grafoil-based KC_{24} at 77K and 87K fitted to a virial-type thermal equation. Inset: Isosteric heat as a function of adsorption amount.

Hydrogen adsorption isotherms of RbC₂₄ and CsC₂₄

Hydrogen adsorption isotherms were collected for RbC₂₄ and CsC₂₄ samples. These measurements were performed on a Sieverts instrument at NCNR¹¹⁵. Temperature control was provided by a closed-cycle helium refrigeration unit, which enabled data to be collected at temperatures different than the standard 77 K and 87 K. The collection time for each isotherm point was 15 min, regardless of whether equilibrium was reached within that duration. Isotherms for RbC₂₄ and CsC₂₄ are presented in Figure 46 and Figure 47, respectively. The RbC₂₄ and CsC₂₄ isotherms have the classic Langmuir isotherm shape. This reflects the fact that there is apparently no lattice expansion in RbC₂₄ or CsC₂₄ in response to hydrogen adsorption. For both samples, the largest adsorption amounts were actually obtained at a sample temperature of 120 K. Adsorption at lower temperatures appeared to be reduced due to sluggish kinetics. Isostatic heats for RbC₂₄ and CsC₂₄, averaged over $0.25 < x < 1.5$, are an astonishing 12.6 kJ mol^{-1} and 14.9 kJ mol^{-1} , respectively. This is close to the optimal adsorption enthalpy of $\Delta H = 18 \text{ kJ mol}^{-1}$ for engineering applications. Of course, it would have been very interesting to measure the adsorption at room temperature to determine the delivery between 3 bar and 100 bar. Unfortunately, the RbC₂₄ and CsC₂₄ samples also appear to react with hydrogen at 195 K and higher temperatures. Experimentally, we observe a reduction in the maximum 77 K hydrogen adsorption capacity following adsorption at 195 K. A summary of maximum H₂ adsorption capacities and average isosteric heats for KC₂₄, RbC₂₄, and CsC₂₄ is listed in Table 6.

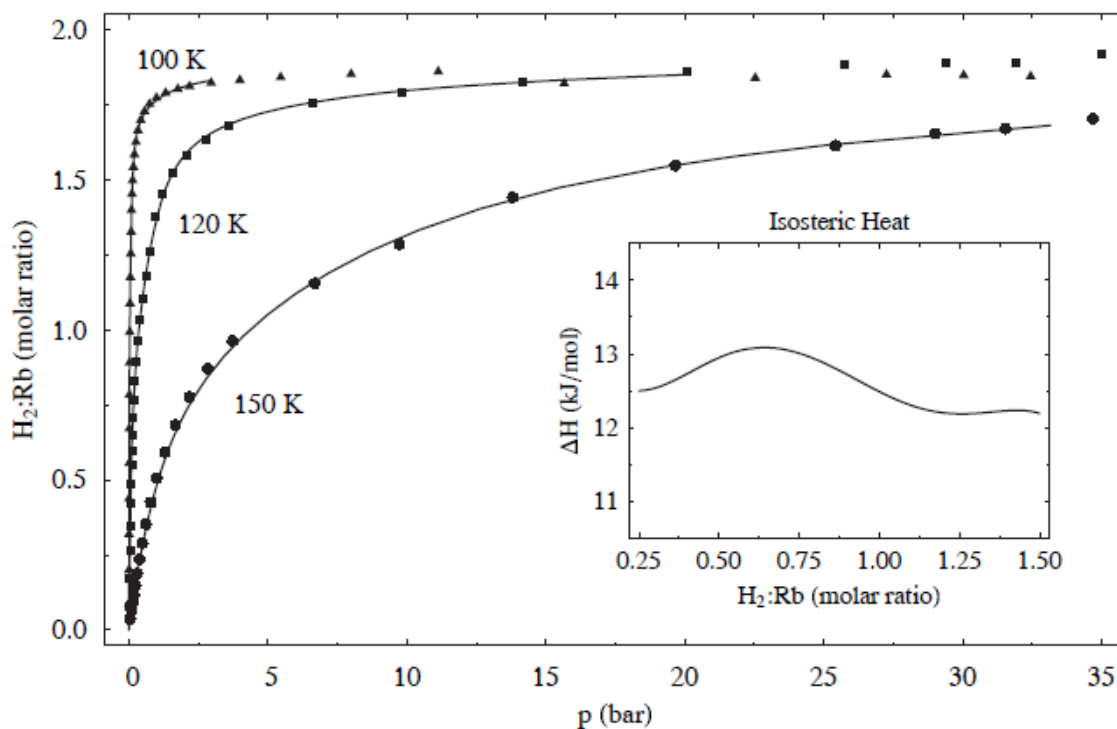


Figure 46. Adsorption isotherms of RbC₂₄ at 100, 120 and 150 K_fitted to a virial-type thermal equation. Inset: Isosteric heat as a function of adsorption amount.

¹¹⁵ W. Zhou, H.Wu, M. R. Hartman, and T. Yildirim. Hydrogen and methane adsorption in metal-organic frameworks: A high-pressure volumetric study. *J. Phys. Chem. C*, 111(44):16131-16137, 2007.

Table 6. Hydrogen adsorption by alkali metal graphite intercalation compounds.

	Max. adsorption		
Sample	wt%	H ₂ :M	Isosteric heat (kJ mol ⁻¹)
KC ₂₄	1.24	2.03	9.2
RbC ₂₄	1.03	1.92	12.6
CsC ₂₄	0.85	1.79	14.9

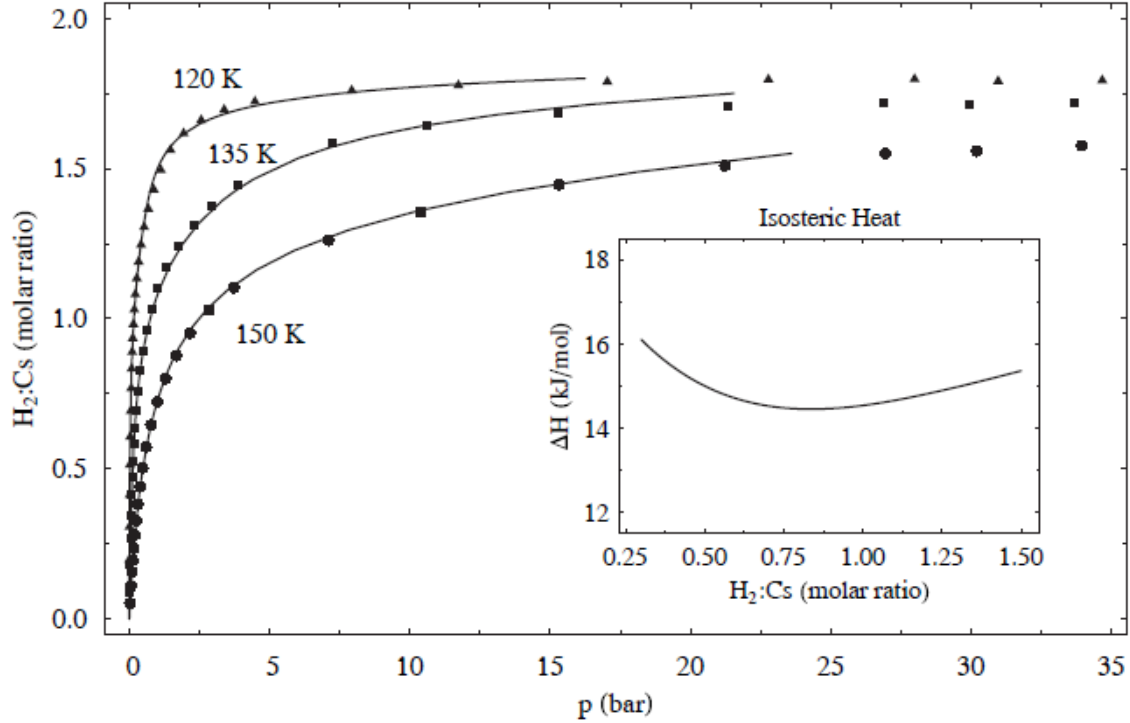


Figure 47. Adsorption isotherms of CsC₂₄ at 120, 135, and 150 K fitted to a virial-type thermal equation. Inset: Isosteric heat as a function of adsorption amount.

Hydrogen adsorption kinetics of intercalation compounds

Kinetic limitation of adsorption appears to be significant in KC₂₄ (as well as in RbC₂₄ and CsC₂₄) at hydrogen compositions greater than $x = 1.5$. There are few vacant adsorption sites for the H₂ molecules to diffuse through, leading to site-blocking and correlation effects. Combined with the small jump attempt frequency that exists at these low temperatures, the result is a reduction in the transport-diffusivity of the adsorbed hydrogen phase.

Adsorption kinetics were measured for RbC₂₄ at 77 K at various hydrogen compositions, as illustrated in Figure 48a. The manifold pressure is plotted versus time for several different final compositions. At low H₂ compositions (e.g., $x = 0.5$) the adsorption is rapid, and the equilibrium pressure is reached within a minute or two. At higher H₂ compositions (e.g., $x = 1.6$) the adsorption is extremely sluggish, and equilibrium is still not reached after an hour. Diffusion-limited adsorption is more significant at low temperatures due to the lower jump attempt frequency. This is evident in Figure 48b, where the 77 K isotherm actually drops

below the 100 K isotherm near $x = 1.7$ because the slower adsorption kinetics reduces the adsorption amount that is measured within a specific time (15 min in this case).

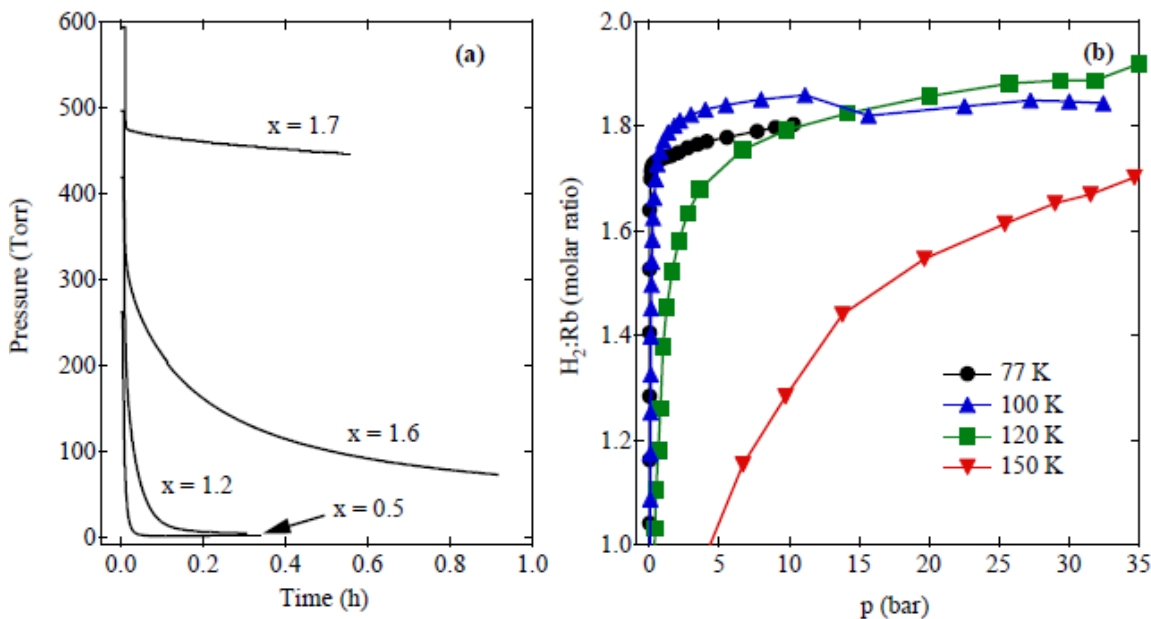


Figure 48. Hydrogen adsorption kinetics of RbC_{24} . (a) Manifold pressure is plotted versus time for several compositions at 77 K. Traces are identified by their final composition $\text{RbC}_{24}(\text{H}_2)_x$. Pressure decreases versus time due to adsorption. (b) Plateau regions of the H_2 adsorption isotherms of RbC_{24} at 77, 100, 120, and 150 K.

Discussion of intercalation compounds

Comprehensive measurements of the adsorption enthalpies and adsorption kinetics of the MC_{24} compounds (for $M = \text{K}, \text{Rb}, \text{Cs}$) were collected over the entire H_2 composition range. The H_2 binding enthalpies for all three compounds are summarized in Figure 49. Compared to activated carbons, there appears to be less energetic heterogeneity in the adsorption potentials of the MC_{24} compounds. The isosteric heats are relatively flat, in contrast to the monotonically decreasing isosteric heats for activated carbons. Because the MC_{24} compounds have more long-range order than activated carbons, it is intuitive that they would have fewer distinct adsorption sites. In addition, the interlayer spacing is wide enough to accept only a single layer of H_2 molecules, further restricting the distribution of distinct adsorption sites. A positive correlation between the adsorption enthalpy and the interlayer spacing is clearly illustrated in Figure 49. The wider 5.9 Å slit pores of CsC_{24} have a stronger adsorption potential than the narrower 5.4 Å slit pores of KC_{24} . However, this trend may also be affected by differences in the electrostatic interaction, due to varying degrees of charge transfer between the graphite and alkali metals. As listed in Table 6, there is also a negative correlation between alkali metal size and adsorption capacity. This is expected, due to the decrease in free volume within the interlayer galleries that occurs with larger alkali metal atoms.

Geometry appears to play a significant role in the sluggish adsorption kinetics observed at large H_2 compositions. Intra-crystalline diffusion in KC_{24} is two-dimensional,

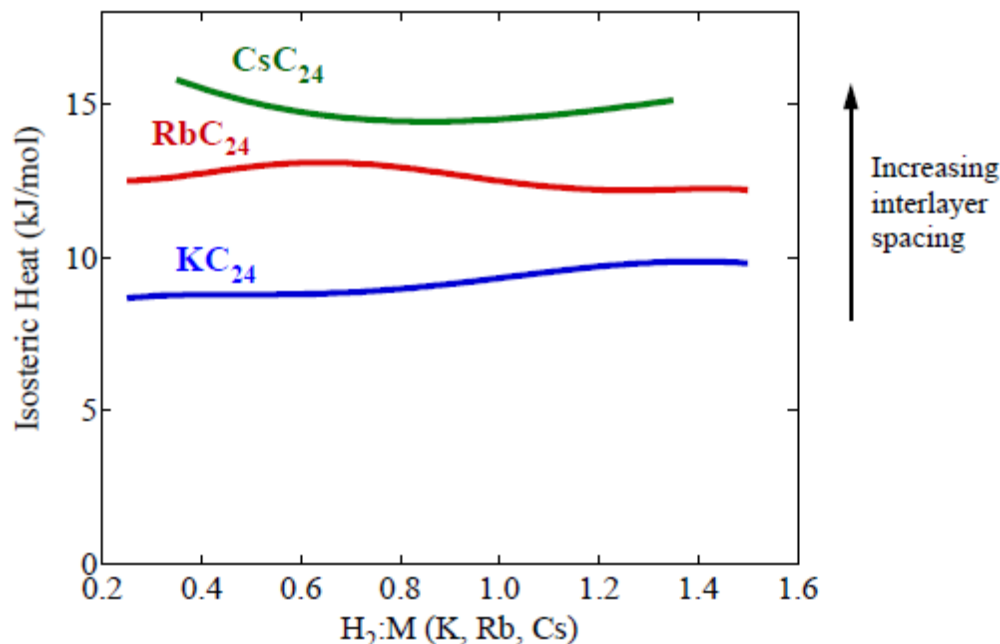


Figure 49. Comparison of hydrogen adsorption enthalpies for KC₂₄, RbC₂₄ and CsC₂₄, plotted as a function of composition.

which means that site-blocking and correlation effects can be even greater due to the reduction in the number of nearest-neighbor sites. Adsorption kinetics, however, is a macroscopic transport phenomenon which can depend on both inter- and intra-crystalline diffusion as well as surface impurities. It is possible that using flake graphite starting material with smaller particle sizes may improve kinetics, but this was not investigated. It was found that Grafoil-based KC₂₄ samples had significantly slower adsorption rates than the flake graphite samples. This may have been due to surface impurities blocking H₂ entry at the crystallite surface.

Conclusion of work on intercalation compounds

Pressure-composition-temperature diagrams were measured for hydrogen adsorption in the intercalated graphite samples KC₂₄, RbC₂₄, and CsC₂₄. Adsorption capacities and isosteric heats were determined and are summarized in Table 6. A model-independent, virial-type thermal equation was used to calculate isosteric heats from the experimental isotherms. Consistent with the literature, the KC₂₄ isotherm has an “S” shape due to lattice expansion associated with H₂ adsorption [48, 49]. The isosteric heat is positively correlated with the size of the alkali metal intercalant. Hydrogen adsorption is kinetically-limited at large H₂ compositions.

Zeolite-Templated Carbon: Characterization and Hydrogen Adsorption

Background

As noted earlier, carbons with remarkably high surface areas (up to ~3000 m² g⁻¹) can be made by conventional chemical activation, among other methods. However, weak hydrogen

binding interactions (typically 4-6 kJ (mol H₂)⁻¹) limit the effective use of carbon materials to cryogenic temperatures and it is predicted that an ideal heat of adsorption for effective storage near ambient conditions is ~15 kJ mol⁻¹.¹¹⁶ At 77 K, the Gibbs excess hydrogen uptake in carbon sorbents increases until a maximum value is reached, typically between 1-4 MPa; this value correlates linearly with the specific surface area of the material. “Chahine’s rule” predicts ~2 wt% excess uptake of hydrogen, and is valid for a large number of different materials^{117,118}. This capacity is consistent with the theoretical value expected for hydrogen adsorbed in a $\sqrt{3}$ configuration on double-sided graphene sheets. Deviations from this trend are usually explained by increased or decreased surface binding interactions for a given surface chemistry or pore character, or by inaccuracies in measurement techniques¹¹⁹.

High-Pressure Hydrogen Storage

Significant hydrogen sorption capacity at or near room temperature is an important target for candidate storage materials, and numerous strategies to enhance adsorption in carbons have been proposed (e.g., “spillover,” light-atom doping, etc.), but as noted from some of our earlier work, none has yet proven to be a viable technology. Since adsorption of hydrogen at room temperature is very weak, excess uptake in physisorbent materials at modest pressures (<10 MPa) is usually below 1 wt%. There is no general rule relating specific surface area to excess hydrogen uptake capacity at 298 K because a Gibbs surface excess maximum is not achieved at these pressures. However, hydrogen uptake at a given pressure and 298 K is indeed known to be linearly correlated with specific surface area: ~0.2 wt% excess uptake of hydrogen per 1000 m² g⁻¹ at 6.5 MPa¹¹⁸, for example, an order of magnitude lower than at 77 K.

Zeolite-Templated Carbons

Template carbonization, among other methods of structural control, has also been explored as a technique to produce carbonaceous materials with exceptionally large specific surface area and finely tuned porosity^{120,121,122,123,124,125,126,127}. It was reported in 2009 that a particular class of templated materials, zeolite-templated carbons (ZTCs), exhibits remarkable hydrogen storage capacities at room temperature under high-pressure

¹¹⁶ J. Purewal, J. Keith, C. Ahn, B. Fultz, C. Brown, and M. Tyagi, 'Adsorption and melting of hydrogen in potassium-intercalated graphite', *Phys. Rev. B*, **79** (2009).

¹¹⁷ E. Poirier, R. Chahine, and T. K. Bose, 'Hydrogen adsorption in carbon nanostructures', *Int. J. Hydrogen Energy*, **26**, 831-835 (2001).

¹¹⁸ B. Panella, M. Hirscher, and S. Roth, 'Hydrogen adsorption in different carbon nanostructures', *Carbon*, **43**, 2209-2214 (2005).

¹¹⁹ R. Ströbel, J. Garche, P. T. Moseley, L. Jörissen, and G. Wolf, 'Hydrogen storage by carbon materials', *J. Power Sources*, **159**, 781-801 (2006).

¹²⁰ T. Kyotani, 'Control of pore structure in carbon', *Carbon*, **38**, 269-286 (2000).

¹²¹ T. Kyotani, T. Nagai, S. Inoue, and A. Tomita, 'Formation of new type of porous carbon by carbonization in zeolite nanochannels', *Chem. Mater.*, **9**, 609-615 (1997).

¹²² H. Nishihara, P. X. Hou, L. X. Li, M. Ito, M. Uchiyama, T. Kaburagi, A. Ikura, J. Katamura, T. Kawarada, K. Mizuuchi, and T. Kyotani, 'High-pressure hydrogen storage in zeolite-templated carbon', *J. Phys. Chem. C*, **113**, 3189-3196 (2009).

¹²³ M. A. de la Casa-Lillo, F. Lamari-Darkrim, D. Cazorla-Amorós, and A. Linares-Solano, 'Hydrogen storage in activated carbons and activated carbon fibers', *J. Phys. Chem. B*, **106**, 10930-10934 (2002).

¹²⁴ B. Liu, H. Shioyama, T. Akita, and Q. Xu, 'Metal-organic framework as a template for porous carbon synthesis', *J. Am. Chem. Soc.*, **130**, 5390-5391 (2008).

¹²⁵ B. Liu, H. Shioyama, H. Jiang, X. Zhang, and Q. Xu, 'Metal-organic framework (MOF) as a template for syntheses of nanoporous carbons as electrode materials for supercapacitors', *Carbon*, **48**, 456-463 (2010).

¹²⁶ H.-L. Jiang, B. Liu, Y. Q. Lan, K. Kuratani, T. Akita, H. Shioyama, F. Zong, and Q. Xu, 'From metalorganic framework to nanoporous carbon: toward a very high surface area and hydrogen uptake', *J. Am. Chem. Soc.*, **133**, 11854-11857 (2011).

¹²⁷ H. Nishihara and T. Kyotani, 'Templated nanocarbons for energy storage', *Adv. Mater.*, **24**, 4473- 4498 (2012).

conditions (10-34 MPa)¹²². This result was promising for applications of hydrogen storage at room temperature where modestly high pressures are not a barring limitation, and was highly relevant for mobile vehicle applications since hydrogen delivery has already been established up to 70 MPa on the public market (e.g., at the UC Irvine hydrogen station, since 2006). The reported substantial increase of hydrogen uptake in ZTC “P7(2)-H” could not be explained by surface area alone; the uptake in ZTCs exceeded that of commercially available superactivated carbon of similar surface area, Maxsorb® MSC-30, by nearly 100% at 34 MPa. Extremely narrow microporosity in ZTCs was credited with the improvement, exhibiting optimal pore size for the accommodation of two layers of hydrogen in each pore¹²³. However, heats of adsorption in these ZTCs did not show an increase, remaining below 8 kJ mol⁻¹, and the lack of any substantial changes to the thermodynamics is consistent with this explanation. Additionally, BET surface area is notoriously susceptible to error in highly microporous materials such as ZTCs, and may be a significant source of error in the characterization of uptake capacity per surface area at room temperature.

4.1.4 Further Investigation

Measurements of hydrogen adsorption in sorbent materials beyond 15 MPa are few, and most tend towards a plateau beyond 10 MPa at room temperature, while ZTCs are reported to continually increase in this high-pressure regime¹²². Further investigation of this effect was undertaken to ascertain the nature of this anomalous behavior. In the present study, high surface area carbon sorbents were prepared by the zeolite templating method; materials with BET surface areas of up to 3600 m² g⁻¹ were produced in multi-gram quantities. Hydrogen uptake measurements of these materials at 77, 87, and 298 K were performed with multiple instruments to assess the viability of ZTCs as hydrogen storage materials for room temperature applications. A specially designed volumetric apparatus was constructed for this work and commissioned for measurements up to 70 MPa.

4.2 Materials Synthesis

To characterize the potentially unique hydrogen adsorption in ZTCs, materials which had properties meeting or exceeding those used in the previous report were necessary. It was found that synthesis of materials up to ~3000 m² g⁻¹ was readily accomplished with simple laboratory infrastructure, but a limit was reached. High template fidelity was fully realized when experiments were performed together with HRL Laboratories using a converted CVD apparatus which could perform heating under high vacuum or in high purity inert gas conditions: materials with surface areas up to 3600 m² g⁻¹ were synthesized. The method was readily scalable in both cases, yielding multi-gram quantities of product with ease.

Raw Materials

Zeolum® zeolite molecular sieve materials were obtained from Tosoh Corporation, specifically, HSZ-320NAA (faujasite structure, Na cation, SiO₂/Al₂O₃ = 5.5 mol/mol) (NaY) and HSZ-930NHA (beta structure, NH₄ cation, SiO₂/Al₂O₃ = 27 mol/mol) (NHβ). Maxsorb MSC-30 superactivated carbon was obtained from Kansai Coke & Chemicals Company, Ltd. Activated carbon CNS-201 was obtained from A. C. Carbons Canada Inc. These materials were stored at 150°C under vacuum in a Buchi glass oven before use. Zeolite templated carbon (ZTC) materials were prepared at HRL and Caltech by previously established methods (a representative schematic is shown in Figure 50)¹²².

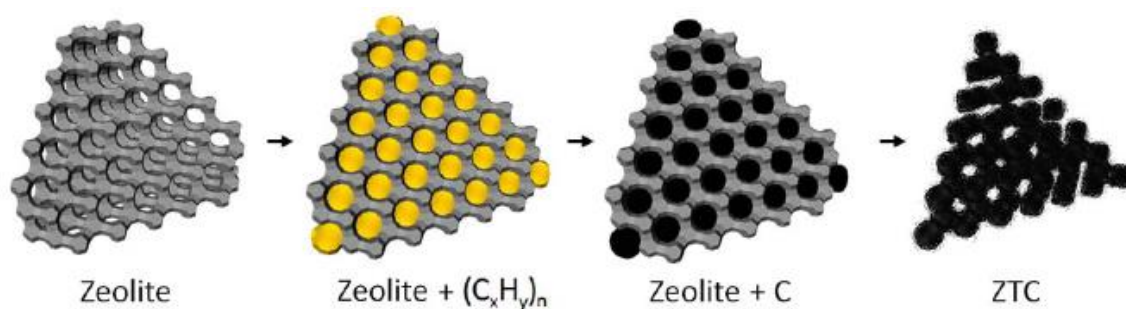


Figure 50. A schematic of template-carbonization in a porous zeolite framework, to produce zeolite-templated carbon (ZTC).

Caltech Experiments

At Caltech, dried zeolite (<1 wt% H₂O) and furfuryl alcohol (98%, Sigma Aldrich) were combined at room temperature under reduced pressure. In the largest batches, 3 g of dried zeolite were added to 60 mL of furfuryl alcohol and magnetically stirred for 24 h. The zeolite-furfuryl alcohol mixture was collected by vacuum filtration and washed with excess mesitylene (99.0%, Sigma Aldrich) yielding 3.5 g of a white-gray powder. The dry powder was transferred to ceramic boats and placed in N₂ flow inside a horizontal alumina tube furnace, pre-heated to 80°C. Polymerization was performed under N₂ flow at 150°C for 12 h. Temperature was increased at 2°C min⁻¹ to 700°C, and gas flow was then switched to a propylene/N₂ mixture (7% propylene) for 2 h. Gas flow was switched back to pure N₂ and temperature was increased at 10°C min⁻¹ to 900°C. Carbonization at 900°C was performed for 3 h. The product, referred to as Z-C, was cooled to room temperature and transferred to a PTFE beaker, yielding 2.5 g. A 3 mL aqueous solution of HF (48%, EM Industries) was added dropwise to the Z-C, stirred, and allowed to dissolve for 2 h. The aqueous solution was further diluted in a large flask to 1200 mL. The remaining solid product, ZTC, was collected by vacuum filtration and washed with water. The ZTC was dried and stored at 150°C under vacuum in a Buchi glass oven. HF treatment was repeated until no zeolite peaks remained in the x-ray diffraction (XRD) pattern, yielding 1 g of final product. By this method, two different ZTC samples were prepared: ZTC-1 from zeolite NH β and ZTC-2 from zeolite NaY. Experiments at Caltech lasted approximately 12 months until it was clear that limitations in control of inert atmosphere conditions during the synthetic process proved to be a barrier to achieving ultra-high surface areas. We reached ~2900 m² g⁻¹, but could not proceed to higher surface area or greater template fidelity. Further synthetic efforts were undertaken at HRL Laboratories, described below.

HRL Experiments

At HRL, 6.0 g of zeolite NaY was further dried at 450°C under vacuum for 8 h to <0.02 wt% H₂O. After cooling to room temperature, 12 mL of furfuryl alcohol (98%, Sigma Aldrich) was added by injection and the mixture was stirred under Ar atmosphere for 24 h. The zeolite-furfuryl alcohol mixture was collected via vacuum filtration and washed 4 times with 100 mL aliquots of xylenes. The washed powder was placed in a 8×8 cm shallow quartz boat and loaded into a 10 cm diameter quartz tube furnace/CVD reactor. The reactor was purged with Ar at room temperature, and was held at 80°C under Ar flow (2 L min⁻¹) for 24 h. Polymerization was performed at 150°C under Ar flow (2 L min⁻¹) for 8

h. Temperature was increased at $5^{\circ}\text{C min}^{-1}$ to 700°C under Ar flow (2 L min^{-1}), and gas flow was then switched to a propylene/ N_2 mixture (7% propylene, 3.2 L min^{-1}) for 4 h. Holding the temperature at 700°C , the reactor was purged under Ar flow (4 L min^{-1}) for 10 min. Temperature was increased to 900°C under Ar flow (2 L min^{-1}) and held for 3 h. The NaY-C product was cooled to room temperature and transferred to a PTFE beaker where 200 mL of aqueous HF (48%, Sigma-Aldrich) were added. After 16 h, the ZTC was collected by vacuum filtration and washed 10 times with 50 mL aliquots of water. The ZTC was dried and stored at 150°C under vacuum in a Buchi glass oven, yielding 1.4 g of final product. A TGA measurement conducted in air up to 1000°C yielded a residual mass of $\sim 2\%$, indicating nearly complete dissolution of the zeolite template. By this method, samples such as ZTC-3 were prepared. By improving inert atmosphere conditions during combination of raw materials, polymerization, and carbonization, such as for ZTC-3, significant improvements in templating fidelity were observed. Careful control of inert atmosphere as well as thorough drying of the zeolite precursor was found to be critical for obtaining a product with surface area beyond $3000\text{ m}^2\text{ g}^{-1}$.

Materials Characterization

Nitrogen Adsorption

Nitrogen isotherms were measured at 77 K with a BELSORP-max volumetric instrument (BEL-Japan Inc.) and surface areas were calculated using the BET method¹²⁸. Equilibrium adsorption isotherms of N_2 at 77 K are shown in Figure 51. Pore-size distributions were calculated by the non-local density functional theory (NLDFT) method¹²⁹ from high-resolution data collected on a Micromeritics ASAP 2020, using a carbon slit pore model and software provided by Micromeritics. Other geometrical models were also explored, notably a unique carbon cylindrical pore model, but none showed a better fit to the data. Pore-size distributions of ZTC-3 and MSC-30 calculated by the DFT method are shown in Figure 52. Distinct regularity of pore-size, centered at a width of 1.5 nm, can be seen for ZTC-3, which is consistent with other reports¹²⁷. MSC-30 shows a broader and larger pore size distribution with significant pore volume in pores up to 3.5 nm wide. The BET surface area and Dubinin-Radushkevich (DR) micropore volume of each of the materials studied are summarized in Table 8. MSC-30 and CNS-201 were measured to have $3240\text{ m}^2\text{ g}^{-1}$ and $1100\text{ m}^2\text{ g}^{-1}$ BET surface areas, respectively. The BET surface area of MSC-30 was calculated in the region $0.0005 < P/P_0 < 0.35$, and is discussed further elsewhere¹³⁰. All materials measured show high BET surface area and high relative uptake of N_2 in the linear region of the isotherm, among the highest known for carbonaceous materials. The DR calculations were found to be susceptible to similar pitfalls as the BET method, especially for MSC-30 which shows multiple stages of different slopes in the DR curve.

Skeletal Density Measurements

Helium pycnometry measurements were performed using a standard Sieverts apparatus at pressures between 0.1-3.0 MPa at 298 K. Ten to thirty measurements were performed and the average skeletal densities of the materials studied are summarized in Table 8. ZTC-1 and ZTC-2 were measured to be 1.9 g mL^{-1} , while ZTC-3 was measured to be 1.8 g mL^{-1} , a significant difference from the activated carbons studied (both 2.1 g mL^{-1}); the standard

¹²⁸ S. J. Gregg and K. S. W. Sing, *Adsorption, surface area, and porosity*, Academic Press, London (1982)

¹²⁹ P. Tarazona, U. M. B. Marconi, and R. Evans, 'Phase equilibria of fluid interfaces and confined fluids', *Mol. Phys.*, **60**, 573-595 (1987).

¹³⁰ N. P. Stadie, J. J. Vajo, R. W. Cumberland, A. A. Wilson, C. C. Ahn, and B. Fultz, 'Zeolite-templated carbon materials for high-pressure hydrogen storage', *Langmuir*, **28**, 10057-10063 (2012).

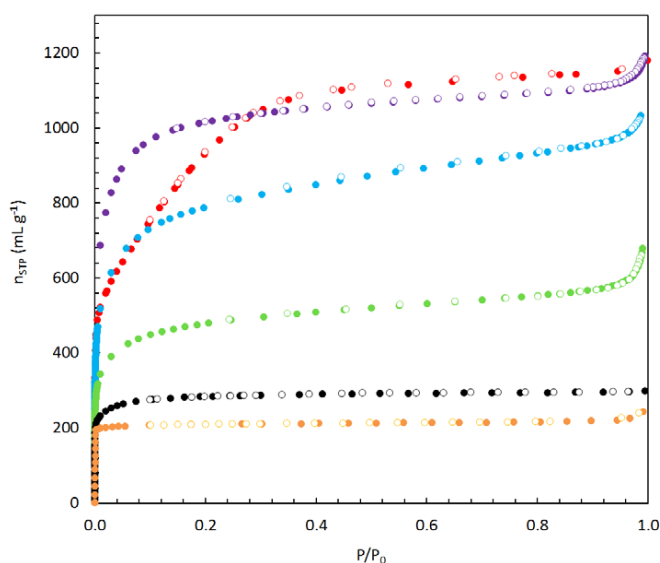


Figure 51. Equilibrium adsorption (closed) and desorption (open) isotherms of N₂ at 77 K on MSC-30 (red), ZTC-1 (green), ZTC-2 (blue), ZTC-3 (purple), CNS-201 (black), and zeolite NaY (orange). Uptake is expressed in units of volume of N₂ (at STP) per unit mass.

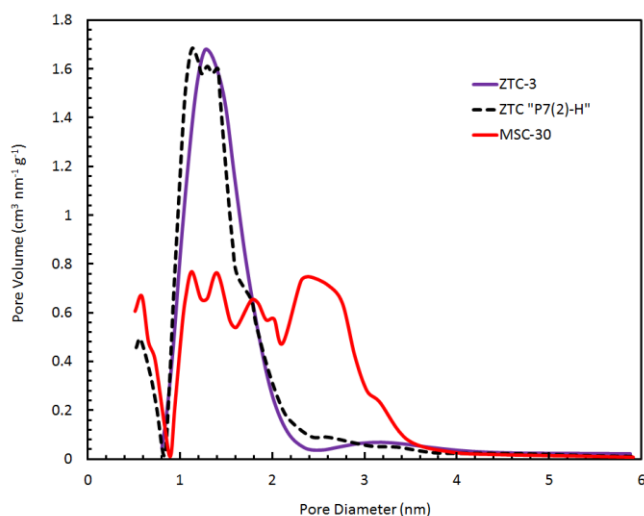


Figure 52. DFT pore-size distribution of ZTC-3 (purple) compared to MSC-30 (red) and ZTC "P7(2)-H" (dashed black), an equivalent reference material.⁷

error was $\pm 0.06 \text{ g mL}^{-1}$ between samples. Previous measurements of carbon materials in our laboratory gave values of $2.12 \pm 0.05 \text{ g mL}^{-1}$ over numerous different carbon types, including MSC-30. The significantly lower skeletal densities in ZTCs result in $\sim 1 \text{ mmol g}^{-1}$ difference in the calculated excess hydrogen uptake at 30 MPa and 298 K. This significant difference must be taken into account for uptake calculations, and seems to be unique to ZTCs as discussed later.

X-Ray Diffraction

X-ray diffraction (XRD) experiments were performed using a PANalytical X'Pert Pro powder diffractometer with Cu $K\alpha_{1,2}$ radiation. Diffraction patterns of ZTC-2 and ZTC-3 are shown in Figure 53, compared to the pure zeolite NaY precursor and the composite NaY-C material before HF treatment. Also shown is the calculated crystal structure of the faujasite (FAU) framework.

Table 7. Material properties of activated carbons CNS-201, MSC-30 and zeolite templated carbon ZTC-3.

Material	Skeletal Density ϕ (g mL ⁻¹)	Bulk Density $\phi\phi$ (g mL ⁻¹)	BET Surface Area (m ² g ⁻¹)	DR Micropore Volume (mL g ⁻¹)
CNS-201	2.1	0.5	1095 \pm 8	0.45
MSC-30	2.1	0.27	3244 \pm 2	1.54
ZTC-3	1.8	0.18	3591 \pm 60	1.66

Table 8. BET surface area (SA) and hydrogen uptake capacity reported for carbonaceous sorbent materials: CNS-201, MSC-30, and ZTCs.

Material	Density (g mL ⁻¹)	BET SA (m ² g ⁻¹)	H ₂ Capacity [†] (mmol g ⁻¹)	High P H ₂ Uptake [‡] (mmol g ⁻¹)	- ΔH_0 (kJ mol ⁻¹)
CNS-201	2.1	1095 \pm 8	12.7	2.48	8.6
MSC-30	2.1	3244 \pm 28	27.9	7.66	6.7
ZTC-1	1.9	1691 \pm 21	18.5	3.99	-
ZTC-2	1.9	2964 \pm 18	26.1	6.45	6.6
ZTC-3	1.8	3591 \pm 60	28.6	8.27	6.5
CNS-201	2.2	1440	12.9	-	-
MSC-30	2.2	3000	26.5	-	-
MSC-30	2.1	2680	-	5.5	7.3
P7(2)-H	1.9	3800	-	10.7	8

The sharp peak centered at $2\theta = 6^\circ$ is the (111) reflection of the cubic zeolite structure. In the final products, ZTC-2 and ZTC-3, no zeolite peaks were detected except this longest periodicity corresponding to the channel-to-channel structure of the template (14 Å), suggesting complete removal of the template from the sample; the remaining peak verifies successful templating of the zeolitic framework in the ZTC. From the width of this diffraction peak, the length scale of the zeolitic order was calculated with the Scherrer equation to be 24 nm (using the Scherrer constant $K = 0.83$ for spherical particles) for ZTC-3.¹³¹ The absence of other peaks confirms the amorphous nature of C-C bonding in ZTCs, and suggests the likelihood of a turbostratic microstructure between regions of pore-to-pore periodicity.

XPS spectrometry

X-ray photoelectron spectroscopy (XPS) was performed to compare ZTCs to MSC-30, but no appreciable difference was found (see Figure 54). XPS studies were performed on a Kratos AXIS Ultra DLD spectrometer with a monochromatic Al-K α source operating at 150 W, with a 20 eV pass energy, and 0.1 eV step (after brief survey spectra were collected). The binding energy was corrected to the most intense peak, which is from sp² hybridized carbon, at 285.0 eV. The intensity was not rescaled since identical instrumental conditions

¹³¹ J. I. Langford and A. J. C. Wilson, 'Scherrer after sixty years: a survey and some new results in the determination of crystallite size', *J. Appl. Crystallogr.*, **11**, 102-113 (1978).

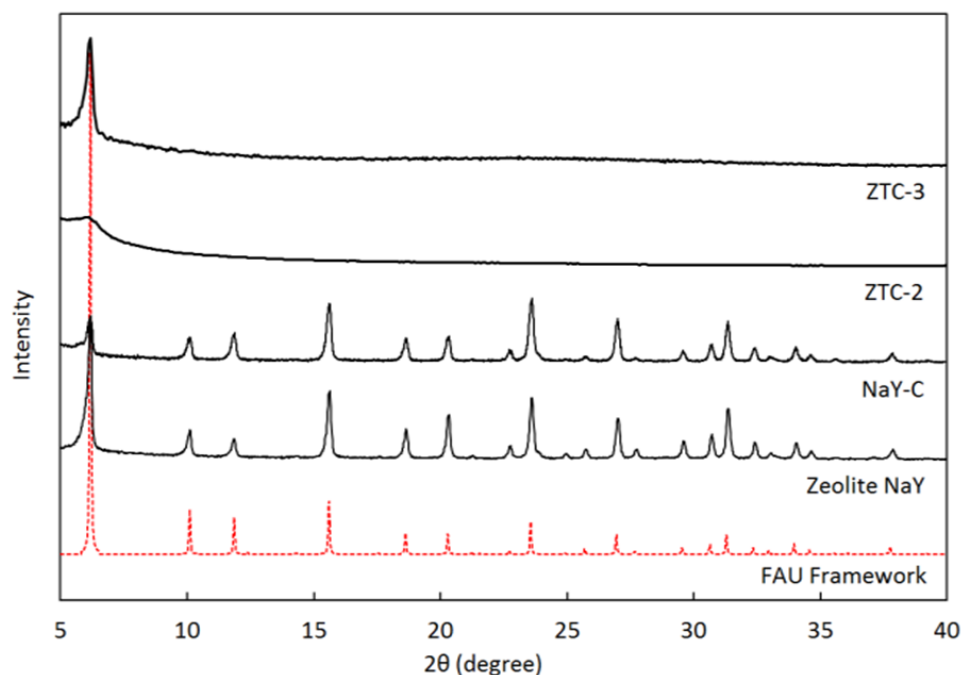


Figure 53. XRD patterns of final products ZTC-2 and ZTC-3, a composite zeolite-carbon intermediate product (NaY-C), pure zeolite NaY (as received), and the FAU zeolitic framework (calculated).

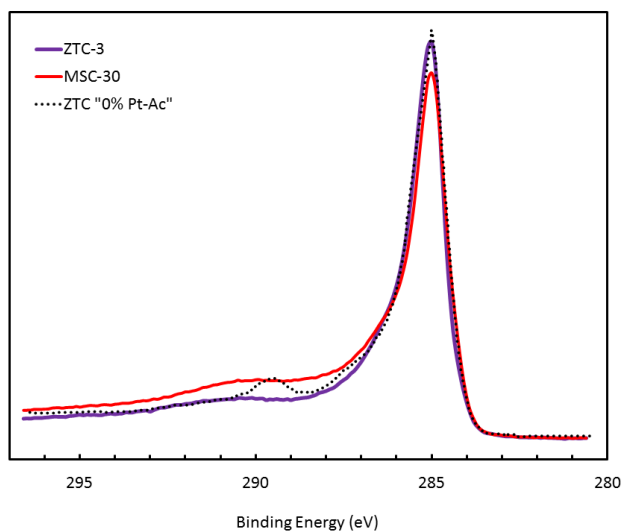


Figure 54. XPS data comparing ZTC-3, MSC-30, and an equivalent reference material, ZTC "0% Pt-Ac."¹³¹

were used across all samples. For peak fitting analysis, a Shirley type background was subtracted and 8 component peaks were fitted, following a previously reported procedure¹³². An example of peak fits is shown in **Figure 55**. The results are summarized

¹³² Y. Yang, C. M. Brown, C. Zhao, A. L. Chaffee, B. Nick, D. Zhao, P. A. Webley, J. Schalch, J. M. Simmons, Y. Liu, J.-H. Her, C. E. Buckley, and D. A. Sheppard, 'Micro-channel development and hydrogen adsorption properties in templated microporous carbons containing platinum nanoparticles', *Carbon*, **49**, 1305-1317 (2011).

in Table 9, indicating 18% and 19% sp³ hybridized carbon in ZTC-3 and MSC-30, respectively.

Table 9. Summary of the XPS analysis results for ZTC-3 and MSC-30.

	Component Fraction (at%)							
Peak Position (eV)	285.0	285.7	286.4	287.3	288.1	289.4	290.2	291.5
Component	C-C sp ²	C-C sp ³	C-OR	C-O-C	C=O	COOR		
ZTC-3	53.4	18.0	8.6	6.0	1.1	4.2	1.0	7.7
MSC-30	48.0	18.8	6.8	4.8	6.1	4.2	3.6	7.7

Electron Microscopy

SEM studies were performed on a Hitachi S-4800 instrument operated at 4.0 keV. Samples were prepared for SEM by dispersing in isopropanol on a holey carbon grid. Evidence can be seen of the superficial likeness between particles of ZTC and the zeolite template from which they were synthesized (shown in Figure 56), similar to that reported by Ma et al¹³³.

TEM studies were performed on a FEI Tecnai F20 instrument operated at 200 keV. Samples were prepared for TEM by dispersing a finely ground mixture of ZTC and isopropanol on a holey carbon grid. Low magnification TEM studies were consistent with the SEM data. A high magnification micrograph of a thin region of ZTC-3 is shown in Figure 57, with an inset showing the Fourier transform of the image. The spots in the transformed image confirm the periodicity of the porous structure. The pore-to-pore spacing of 1.0 nm is consistent with that calculated from DFT treatment of the N₂ adsorption isotherms at 77 K (see Figure 52), and with data reported by Ma et al¹³³.

Electron Energy-Loss Spectroscopy

Electron energy-loss spectroscopy (EELS) was performed to compare ZTCs to MSC-30 and other carbon materials, shown in Figure 58. EELS measurements were performed on a FEI Tecnai F20 instrument operated at 200 keV and equipped with a Gatan Imaging Filter system. To acquire these spectra, the aperture size was 0.6 mm, the dispersion was 0.2 eV pixel⁻¹, and the energy shift was 175 eV. Samples were prepared by dispersing a finely ground mixture of sample material and isopropanol on a holey carbon grid. The pre-edge peak was calibrated to 285.0 eV in all samples, a power-law background was subtracted, and the signal intensity was normalized to the same value at high loss. The ratio of the areas of the pre-edge peak to the main carbon 1s edge (>289 eV) was used to determine the relative content of sp² and sp³ hybridized carbon (see Figure 59). This study also shows only a small difference in the amount of sp² and sp³ hybridized carbon between ZTC-3 and MSC-30: approximately 18% and 16% sp³ content, respectively.

¹³³ Z. Ma, T. Kyotani, and A. Tomita, 'Synthesis methods for preparing microporous carbons with a structural regularity of zeolite Y', *Carbon*, **40**, 2367-2374 (2002).

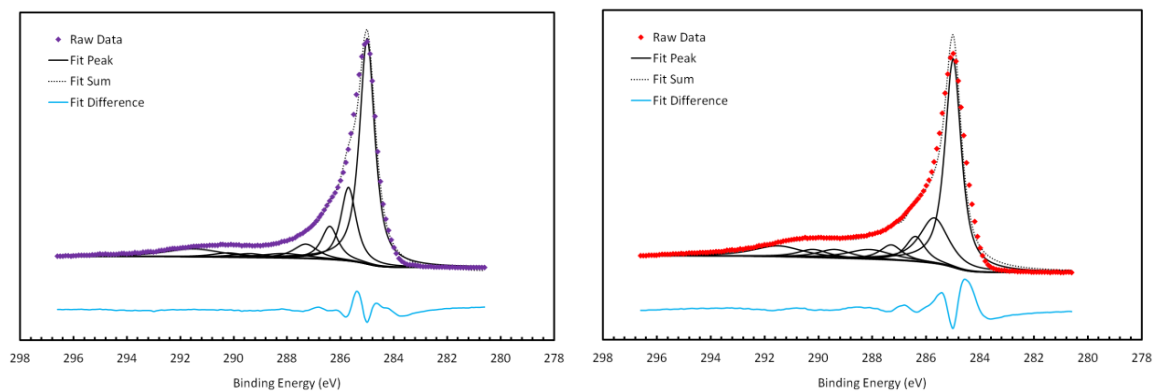


Figure 55. XPS analyses for the carbon 1s regions in ZTC-3 (left) and MSC-30 (right).

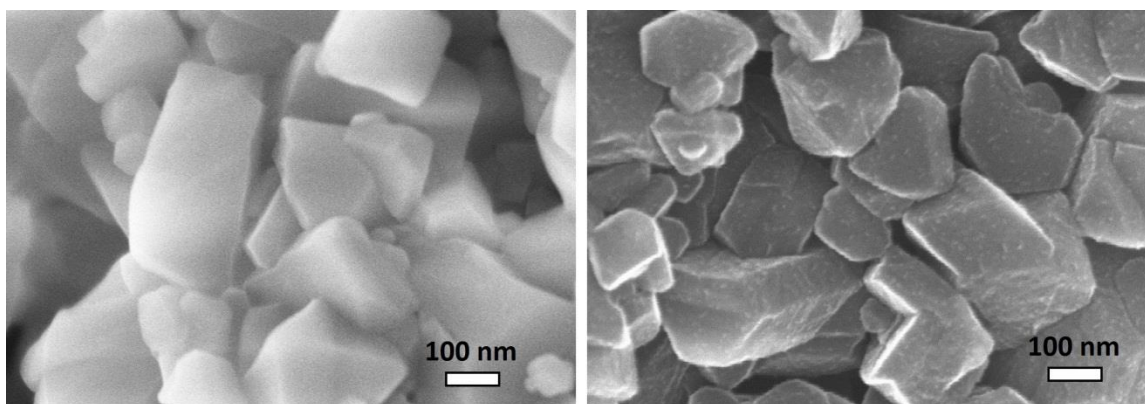
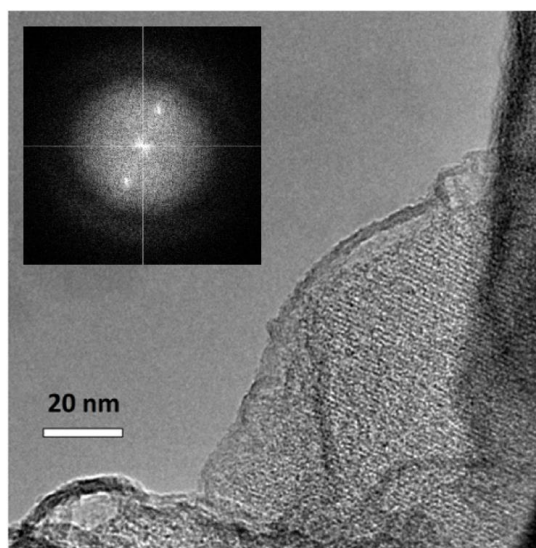


Figure 56. SEM micrographs of zeolite precursor (left) and ZTC product (right), showing similar particle size and shape.

Figure 57. TEM micrograph of ZTC-3 showing pore-to-pore periodicity of 1.0 nm, and the Fourier transform of the image (inset).



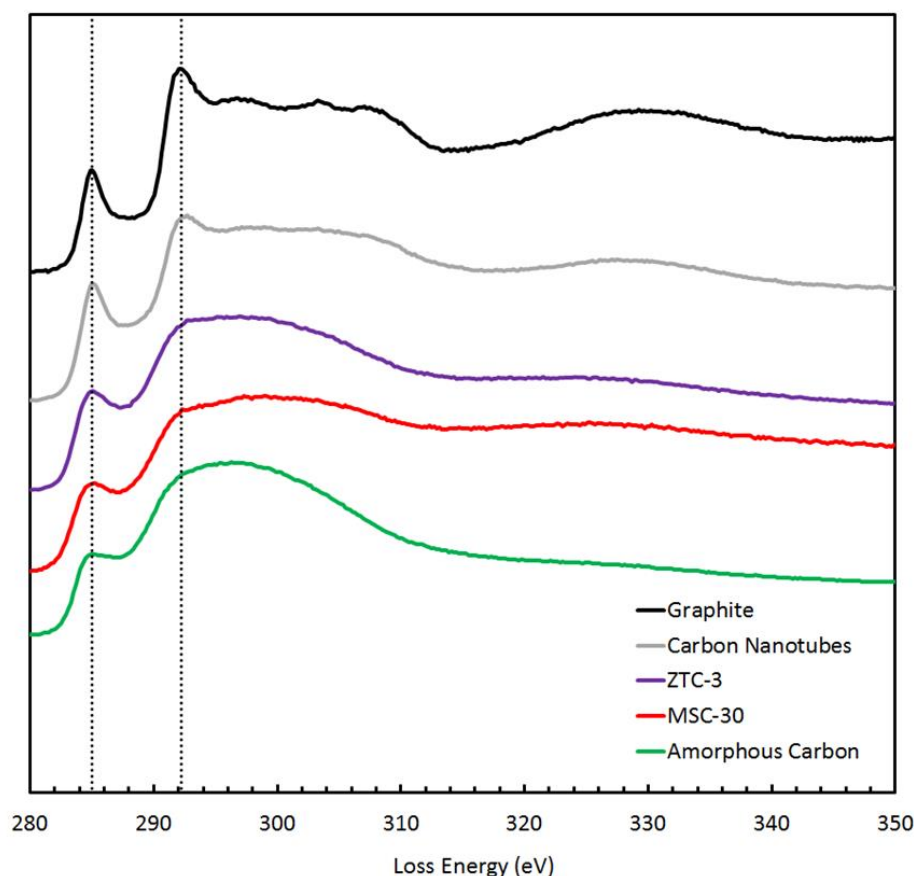
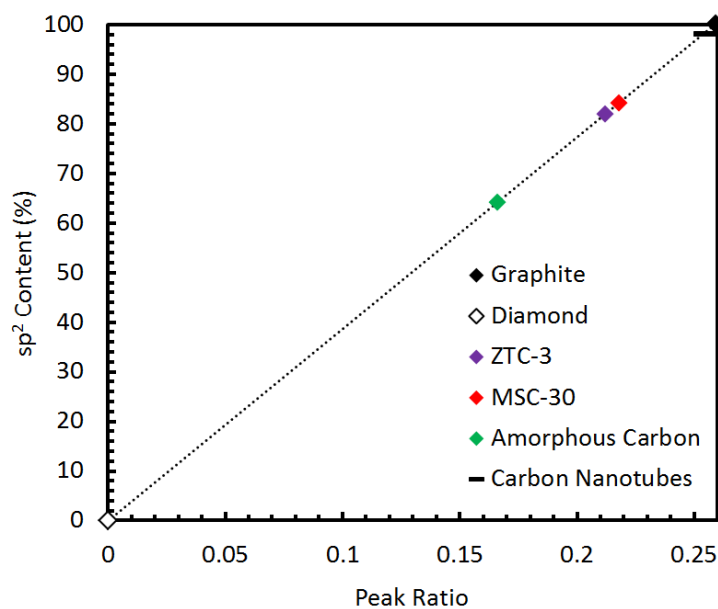


Figure 58. EELS spectra showing the carbon 1s edge in ZTC-3 compared to MSC-30, graphite, carbon nanotubes, and the amorphous holey carbon grid.

Solid-State Nuclear Magnetic Resonance

Solid-state ^{13}C NMR experiments were performed on ZTC-3 and MSC-30 using a Bruker DSX-500 spectrometer equipped with a Bruker 4 mm MAS probe (see Figure 4.11). The sample spinning rates were 12 kHz and 5 kHz for MAS and CPMAS, respectively, performed at room temperature under dry nitrogen gas. CPMAS measurements were performed with a RF field of 62.5 kHz during the CP contact period (0.1 ms). The chemical shifts are given in parts per million (ppm) externally referenced to tetramethylsilane. No significant sp^3 hybridized carbon (10-50 ppm region) in either ZTC-3 or MSC-30 was detected, consistent with previous measurements.¹³⁴ A cross-polarization ^{13}C MAS (CPMAS) study was also carried out, and compared to the MAS data, shown in Figure 60. The results are consistent with a previous report.¹³⁴ A peak fitting analysis was performed to determine the protonated content of carbon in the sp^2 peak. By deconvolution of the main peak into 3 components, it is calculated that ~89% of carbon ZTC-3 is protonated, from the contribution of the fit peak centered at 138 ppm. While an overestimate, this is consistent with results confirming high H content in ZTCs by elemental analysis experiments.

¹³⁴ Z. Ma, T. Kyotani, Z. Liu, O. Terasaki, and A. Tomita, 'Very high surface area microporous carbon with a three-dimensional nano-array structure: synthesis and its molecular structure', *Chem. Mater.*, **13**, 4413-4415 (2001).









						
P1 Area = I_{π^*}	1.54	0	1.96	1.95	1.55	2.08
P2 Area = I_{σ^*}	4.41	1	7.30	6.97	7.75	6.09
P1/P2	0.35	0	0.27	0.28	0.20	0.34
$I_{\pi^*}/(I_{\pi^*} + I_{\sigma^*})$	0.26	0	0.21	0.22	0.17	0.25
Normalized	1	0	0.82	0.84	0.64	0.98
sp ² Content (%)	100	0	81.8	84.2	64.2	98.3

Figure 59. Summary of sp² content in carbon materials studied by EELS, based on the integrated peak areas of the 1s→ π^* peak at ~285 eV to the 1s→ σ^* peak at ~292 eV, and fit to a calibration curve established by graphite and diamond.

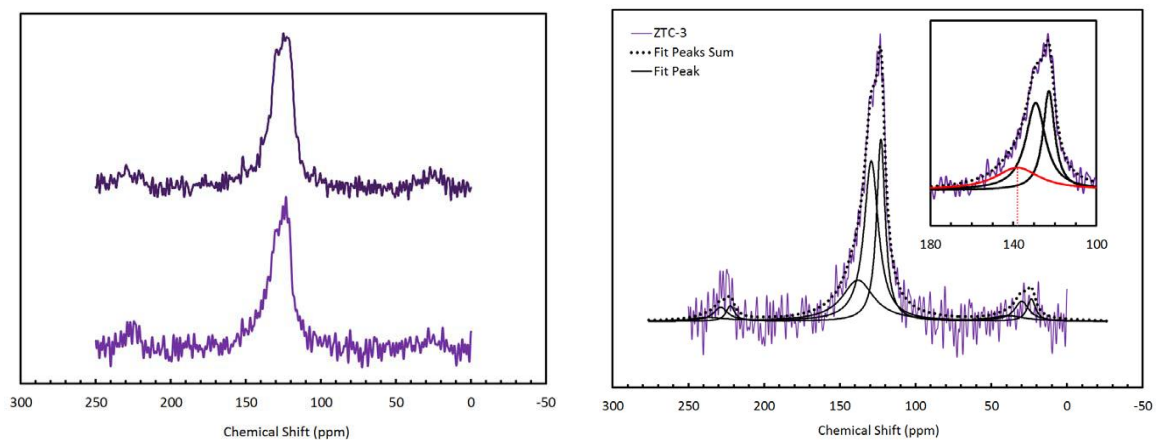


Figure 60. Solid-state ¹³C MAS NMR spectrum of ZTC-3, fitted to three peaks (centered at 130, 136, and 138 ppm). The peak at 138 ppm was not present in CPMAS spectra, and is attributed to non-protonated sp² hybridized carbon, accounting for ~11% of the area of the total signal.

Hydrogen Adsorption

Standard-Pressure Experiments

Hydrogen adsorption isotherms were measured at 77 and 87 K from 0-7 MPa on the Sieverts I apparatus. Temperature baths of liquid nitrogen (77 K) and liquid argon (87 K) were continually filled throughout experiments to maintain low temperature conditions in the sample cell if necessary. The system was leak checked up to 7 MPa and showed a maximum leak rate of 6.0×10^{-7} mol h⁻¹ of H₂. If fitted to an exponential decay function where k is the leak rate, this will correspond to a maximum leak of $k \sim 10^{-9}$ s⁻¹, well within the acceptable limit for accurate measurements.¹³⁵ During measurements, the system was not returned to vacuum between steps, and the measured hydrogen uptake was cumulative.

High-Pressure Experiments

Hydrogen adsorption isotherms at 298 K were measured up to 30 MPa on the Sieverts II apparatus. The temperature of the sample was not controlled, but remained within ± 0.3 K. High pressures were achieved by gas densification in a coil submerged in a liquid nitrogen bath that was removed to allow the coil to return to ambient temperature. Hydrogen uptake was determined in cumulative steps, as described earlier. The system was leak tested up to 45 MPa and showed a maximum leak rate of 2.2×10^{-7} mol h⁻¹ of H₂. This corresponds to a maximum leak of $k \sim 10^{-8}$ s⁻¹. Hydrogen uptake isotherms measured on MSC-30 using Sieverts II were compared to isotherms collected on Sieverts I and the gravimetric balance at EMPA, and were consistent from 0-10 MPa.

Hydrogen Adsorption Results

The complete set of equilibrium adsorption isotherms of hydrogen on CNS-201, MSC-30, ZTC-2, and ZTC-3 is shown in Figure 61. Hydrogen adsorption at all temperatures and pressures was fully reversible in all materials studied after numerous cycles. The Gibbs surface excess maximum hydrogen capacities of the materials are summarized in Table 8. The highest measured was for ZTC-3: 28.6 mmol g⁻¹ (5.5 wt%) at 2.4 MPa. Maximum uptake was higher in ZTC-3 than MSC-30 despite a more gradual initial increase at low pressure. Equilibrium adsorption isotherms of H₂ on ZTCs, MSC-30, and CNS-201 were measured up to 30 MPa at room temperature, and are shown in Figure 62 (the same data as in Figure 61, isolated for clarity). Excess hydrogen capacities of the materials were calculated by extrapolation of the data to 30 MPa and are summarized in Table 8. The highest measured was for ZTC-3: 8.3 mmol g⁻¹ (1.6 wt%) at 30 MPa and 298 K. Verification of the calibration of our high-pressure volumetric apparatus was by measurements of commercial materials MSC-30 and CNS-201. However, comparison of standard materials to references was found to be reliable only in some instances. The superactivated carbon MSC-30, a material processed similarly to Anderson AX-21, is reported to have a BET surface area ranging from 2600-3400 m² g⁻¹.^{136,137,138,139,140}

¹³⁵ L. Schlapbach, 'Hydrogen as a fuel and its storage for mobility and transport', *MRS Bull.*, **27**, 675-679 (2002).

¹³⁶ E. Poirier, R. Chahine, and T. K. Bose, 'Hydrogen adsorption in carbon nanostructures', *Int. J. Hydrogen Energ.*, **26**, 831-835 (2001).

¹³⁷ H. Nishihara, P. X. Hou, L. X. Li, M. Ito, M. Uchiyama, T. Kaburagi, A. Ikura, J. Katamura, T. Kawarada, K. Mizuuchi, and T. Kyotani, 'High-pressure hydrogen storage in zeolite-templated carbon', *J. Phys. Chem. C*, **113**, 3189-3196 (2009).

¹³⁸ M.-A. Richard, D. Cossement, P.-A. Chandonia, R. Chahine, D. Mori, and K. Hirose, 'Preliminary evaluation of the performance of an adsorption-based hydrogen storage system', *AIChE J.*, **55**, 2985-2996 (2009).

¹³⁹ Y. Li and R. T. Yang, 'Hydrogen storage on platinum nanoparticles doped on superactivated carbon', *J. Phys. Chem. C*, **111**, 11086-11094 (2007).

¹⁴⁰ N. P. Stadie, J. J. Purewal, C. C. Ahn, and B. Fultz, 'Measurements of hydrogen spillover in platinum doped superactivated carbon', *Langmuir*, **26**, 15481-15485 (2010).

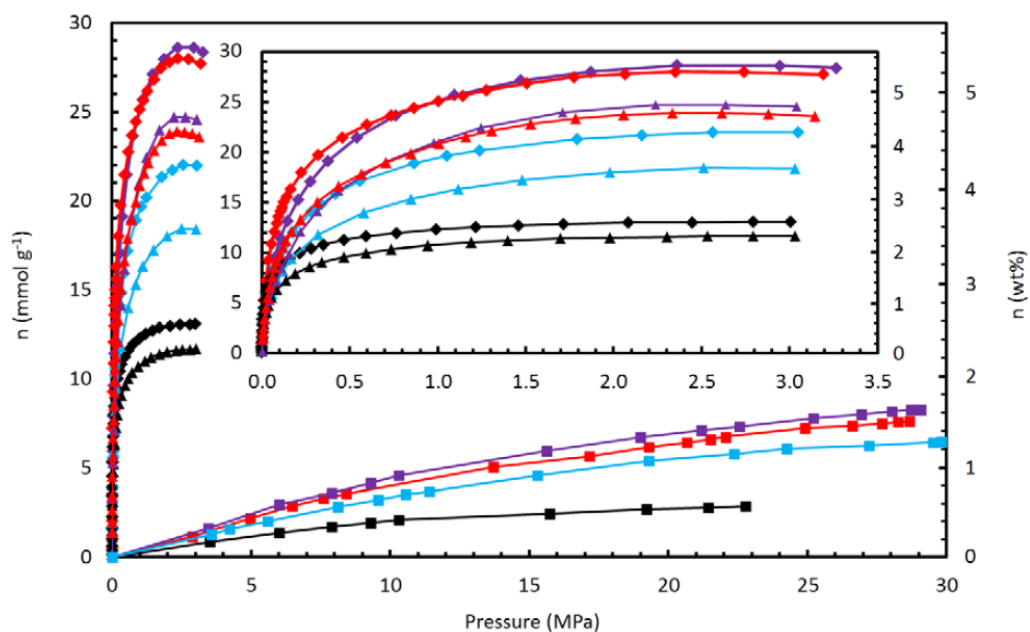


Figure 61. Equilibrium adsorption isotherms of hydrogen on MSC-30 (red), ZTC-2 (blue), ZTC-3 (purple), and CNS-201 (black) at 77 K (diamond), 87 K (triangle), and 298 K (square) between 0-30 MPa (inset shows detail between 0-3.5 MPa).

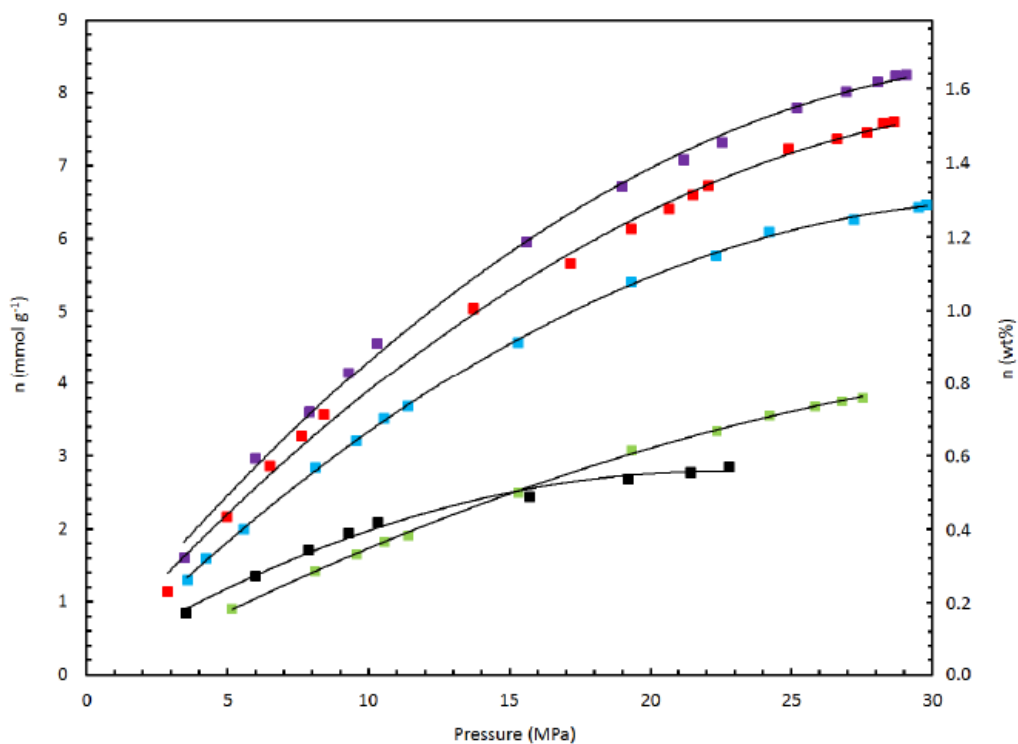


Figure 62. Equilibrium adsorption isotherms of H_2 on MSC-30 (red), ZTC-1 (green), ZTC-2 (blue), ZTC-3 (purple), and CNS-201 (black) at 298 K between 0-30 MPa.

This variation is not only due to differences in the analysis of the N_2 adsorption isotherms at 77 K, but is also reflected in differences in hydrogen adsorption isotherms at temperatures

from 77-298 K, implying that different batches of MSC-30 have different properties. Hydrogen capacities of MSC-30 at 298 K range from 3-4 mmol g⁻¹ (0.6-0.8 wt%) at 10 MPa; in this report, it was measured to be 3.9 mmol g⁻¹ which is consistent with the upper end of this range. Hydrogen uptake in CNS-201 was 2.0 mmol g⁻¹, compared to a reference value of 2.1 mmol g⁻¹.¹³⁸

Enthalpy of Adsorption

The equilibrium excess hydrogen adsorption data for ZTC-3, MSC-30, and CNS-201 were fitted in two ways: using a typical “isoexcess” model-independent virial-type fitting equation (to 3rd order terms), and using a generalized double-Langmuir fitting equation which allows the determination of the absolute adsorption quantity. The enthalpy of adsorption was calculated by the isoexcess and isosteric method, respectively. Plots of the isoexcess enthalpy of adsorption of hydrogen on CNS-201, MSC-30, ZTC-2 and ZTC-3 are shown in Figure 63.

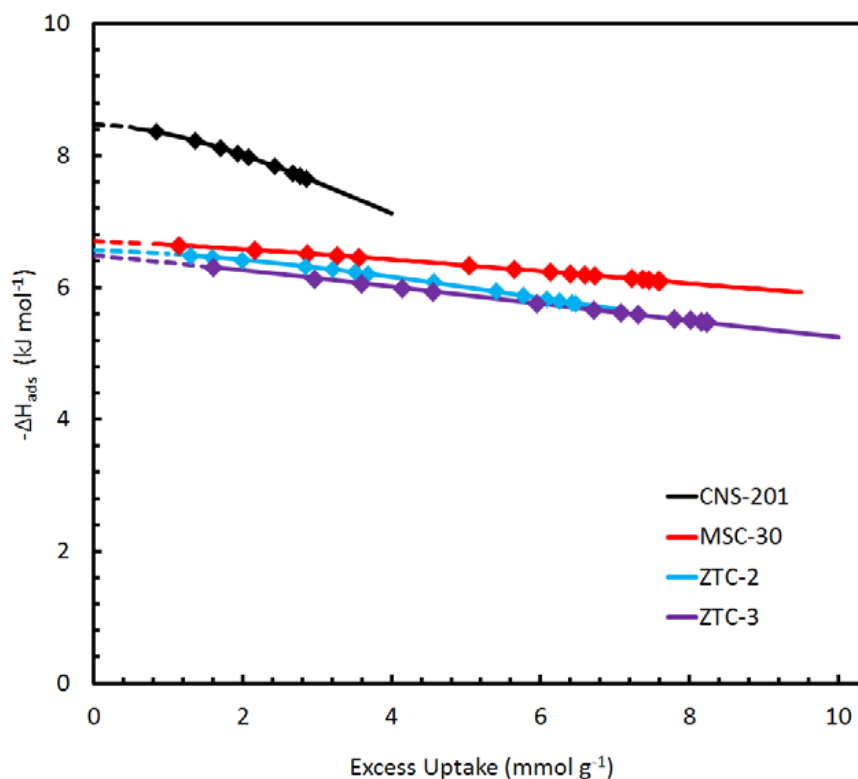


Figure 63. Average isoexcess enthalpy of adsorption of hydrogen on CNS-201 (black), MSC-30 (red), and ZTC-3 (purple) as a function of excess uptake between 77-298 K.

The isosteric enthalpy of adsorption calculated using the real gas density of hydrogen on CNS-201, MSC-30, and ZTC-3 is shown in Figure 64. In both cases, the calculations were performed by fitting the data from the entire range of temperature between 77-298 K. For the isoexcess method, only an average enthalpy was accessible while the isosteric enthalpy could be calculated at arbitrary temperatures within the temperature range measured. The average Henry’s law values, $-\Delta H_0$, for the materials studied are summarized in Table 8. Similar results are found using both methods due to the near-ideal properties of hydrogen

in the temperature and pressure range measured. The highest value reported is for CNS-201 which is known to have an exceptionally high binding energy for hydrogen.¹⁴¹ It decreases substantially as uptake increases, which is also reflected in the shape of the hydrogen uptake curves for CNS-201 at all temperatures. The adsorption enthalpy calculated for ZTCs and MSC-30 decreases only slightly and is relatively constant as uptake increases; the continued increase in uptake at 30 MPa compared to CNS-201 can be attributed to this characteristic of the higher surface area materials.

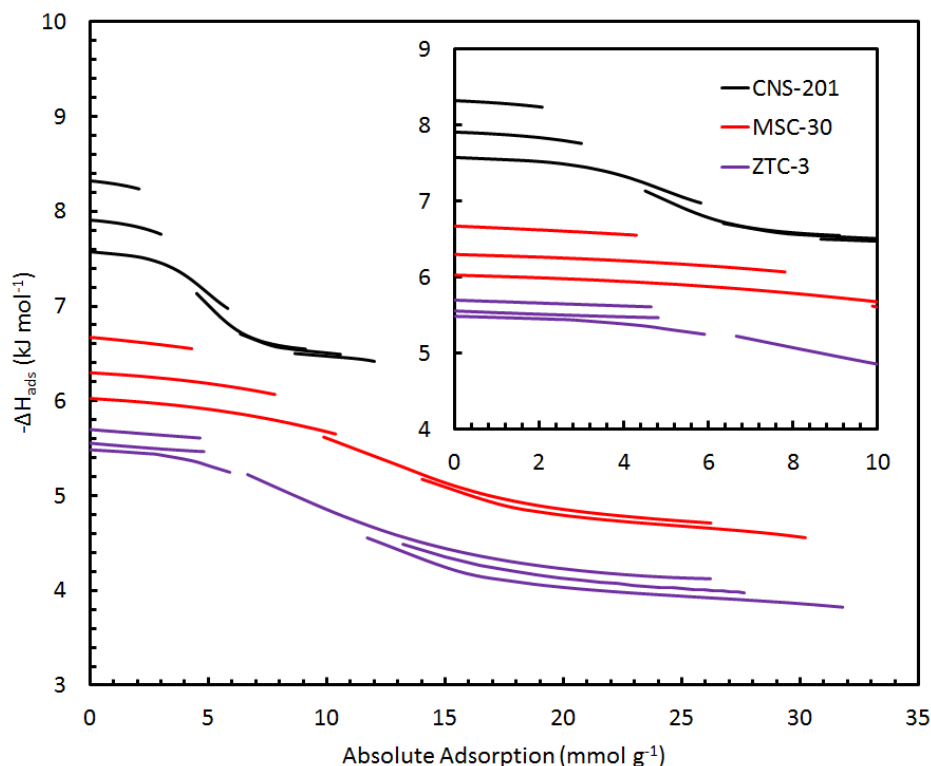


Figure 64. Isosteric enthalpy of adsorption of hydrogen on CNS-201 (black), MSC-30 (red), and ZTC-3 (purple) as a function of absolute uptake, at temperatures from 77-298 K.

Discussion

The addition of sorbent material to a storage tank has two consequences: the volume available for gaseous storage is decreased (by the material's skeletal density) and the surface available for van der Waals interactions is increased (by the material's specific surface area). With enthalpy of adsorption in the range of 4-9 kJ mol⁻¹, as is observed for carbon materials, careful measurements of sample density and surface area are critical for characterizing sorption capacity and can be used together to readily predict material performance in the temperature and pressure conditions studied: 77- 298 K and 0-30 MPa.

Skeletal Density

Skeletal density is the only material specific variable required, and therefore the most important variable in accurate determination of excess hydrogen uptake in adsorption

¹⁴¹ J. J. Purewal, H. Kabbour, J. J. Vajo, C. C. Ahn, and B. Fultz, 'Pore size distribution and supercritical hydrogen adsorption in activated carbon fibers', *Nanotechnology*, **20**, 204012 (2009).

measurements. Carbonaceous materials often have a similar skeletal density to graphite, 2.1-2.2 g mL⁻¹.¹³⁸ However, skeletal densities in ZTCs are significantly lower, 1.8 g mL⁻¹. This indicates a less graphitic nature of ZTCs, but is not easily explained since ZTCs are predominantly sp² carbon.^{132,133} Distortions such as bond stretching or vacancy defects which could alter the ratio of sp² to sp³ bonding of carbon atoms would have to be large to account for this difference. However, the fractions of sp² and sp³ bonding were found to be similar through auxiliary measurements by x-ray photoelectron spectroscopy (XPS), electron energy-loss spectroscopy (EELS), and solid-state ¹³C NMR. One explanation of the significantly lower skeletal density of ZTCs can be given by recent results from elemental analysis experiments. Elemental composition (CHN) of MSC-30 and ZTC-3 was determined by triplicate combustion experiments, using the Dumas method.¹⁴² Samples were prepared by degassing at 250°C and sealed in foil packets in an argon glovebox with < 1 ppm H₂O, a critical step for obtaining an accurate estimate of the H content since any adsorbed H₂O would contribute to detected H. Average hydrogen content in ZTC-3 was 2.4 wt% H, approximately twice that in MSC-30: 1.2 wt% H. If each atomic site where carbon is substituted for hydrogen retains its original skeletal volume, the difference in skeletal density would be 11%, a decrease from 2.1 to 1.9 g mL⁻¹. Additional decrease in skeletal density could be due to the presence of hanging C-H groups which have a larger atomic volume than a pair of sp² hybridized carbon atoms. This approximation gives a representative figure for the significance of increased H content to the skeletal density, an effect that is large enough to account for the difference between MSC-30 and ZTC-3.

Surface Area

Hydrogen uptake at 77 K and 298 K is generally proportional to surface area in the materials studied, as shown in Figure 65. The relationship for ZTCs at 77 K is ~9 mmol g⁻¹ (1.8 wt%) Gibbs surface excess maximum hydrogen capacity per 1000 m² g⁻¹ BET surface area, the same as for other carbonaceous materials.¹¹⁸ This corresponds to 5.4 molecules of H₂ per nm² of BET surface area. The relationship for ZTCs at 30 MPa and 298 K is 2.3 mmol g⁻¹ (0.46 wt%) excess hydrogen uptake per 1000 m² g⁻¹ BET surface area, the same as for other carbonaceous materials in this study. Importantly, this result is contrary to a previous result¹³⁷ which reports higher uptake in ZTCs at 303 K: 2.8 mmol g⁻¹ (0.55 wt%) excess hydrogen uptake per 1000 m² g⁻¹ BET surface area in “P7(2)-H,” compared to 2.0 mmol g⁻¹ (0.41 wt%) per 1000 m² g⁻¹ in MSC-30. In this previous report, a 100% increase in uptake was measured for ZTCs compared to MSC-30, and it could not be explained by surface area. Compared to the results in this study, the measurement of uptake in ZTC “P7(2)-H” was erroneously high, while uptake in MSC-30 was underestimated, contributing to a large apparent enhancement in hydrogen capacity of ZTC compared to MSC-30. While ZTCs measured in the present study show increased uptake compared to MSC-30, this was consistent with their larger specific surface area. These relationships are critically dependent on the accurate and consistent determination of specific surface area of the sorbent material and the assumptions inherent to BET theory. The known shortcomings of this method for microporous materials are thought to be approximately equal in the nitrogen isotherms at 77 K; assumption of a standard pressure range over which to fit the BET equation is not appropriate. The region from low pressure up to the knee of the isotherm (“point B” for a type II isotherm) must be included as this pressure range is different for each material. For MSC-30, the calculation is especially sensitive to the range chosen because the knee is rounded and there are two nearly linear regions in the isotherm

¹⁴² J. B. Dumas, 'A method of estimating nitrogen in organic material', *Ann. Chim. et Phys.*, **58**, 171 (1833).

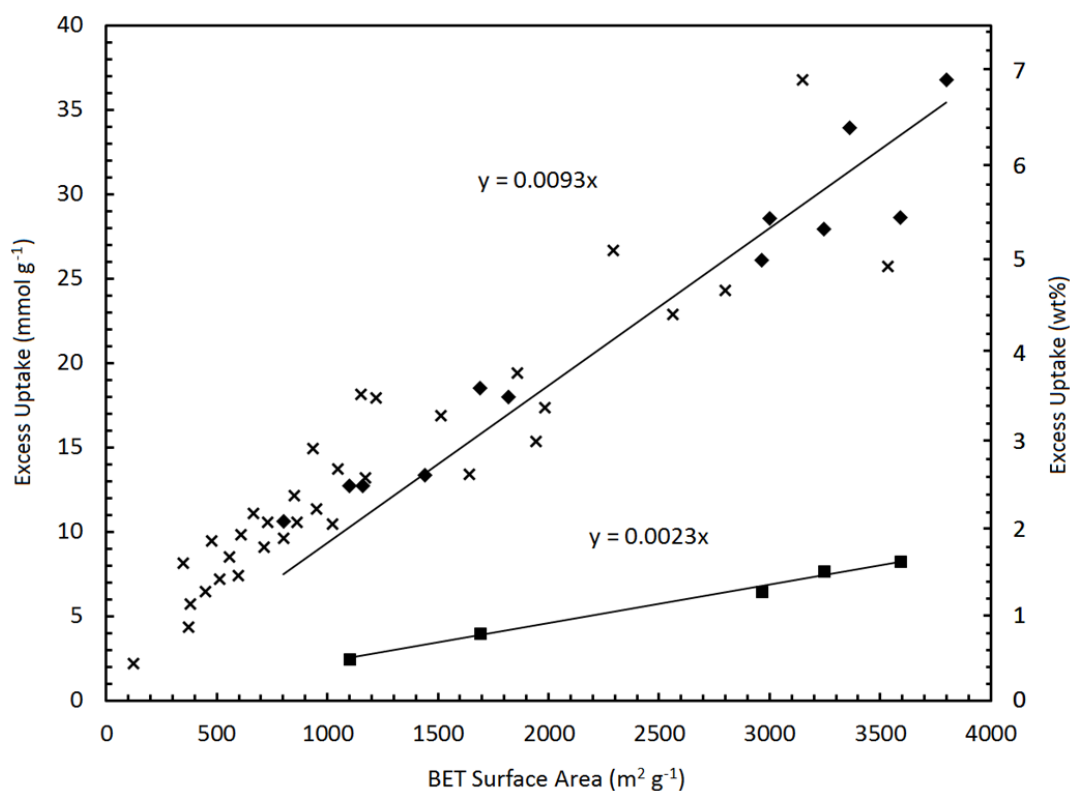


Figure 65. Equilibrium excess adsorption uptake of hydrogen as a function of BET surface area at 77 K (Gibbs excess surface maximum capacity: diamond) and 298 K (at 30 MPa: square). An \times indicates a reported value from the literature, at 77 K.

(type IV like character). Even for classic type II isotherms, BET surface area is often miscalculated: in “CB850h,” a ZTC which was reported to have a maximum excess hydrogen capacity of 8.33 wt% at 77K, the BET surface area is calculated to be $3150 \text{ m}^2 \text{ g}^{-1}$.¹⁴³ This value would represent an extreme outlier on a plot of hydrogen capacity at 77K as a function of surface area; however, our analysis of the reported N_2 isotherm data gives a BET surface area of $3800 \text{ m}^2 \text{ g}^{-1}$, much closer to the expected value for such a high capacity sorbent. Similarly, “P7(2)-H” was reported to have a BET surface area of 3800 (while our analysis yields a value of $3538 \pm 50 \text{ m}^2 \text{ g}^{-1}$).¹³⁷ Another method of ranking similar sorbents of the same material class is by comparing the nitrogen uptake capacity at 77 K and an intermediate pressure, say $P/P_0 = 0.5$. This analysis also shows “CB850h” to be among the highest performance sorbent materials and explains the large excess hydrogen capacity at 77 K. ZTC-3 was found to be nearly identical to “P7(2)-H” in this comparison and explains the similar surface area when a consistent calculation method is used.

4.5.3 Enthalpy of Adsorption

The similarity of isoexcess enthalpies of adsorption between ZTCs and MSC-30 in Figure 63 and Figure 64 implies that there are no significant differences in the dispersion forces responsible for hydrogen physisorption. The high-pressure data at 298 K allows the unique

¹⁴³ Z. Yang, Y. Xia, and R. Mokaya, 'Enhanced hydrogen storage capacity of high surface area zeolite-like carbon materials', *J. Am. Chem. Soc.*, **129**, 1673-1679 (2007).

contribution of high temperature data to the calculation of isoexcess enthalpy of adsorption. However, dispersion forces are known to have a significant temperature dependence.^{144,145} For instance, the heat of adsorption of hydrogen on MOF-5 is reported to increase by up to 1 kJ mol⁻¹ between cryogenic and room temperatures.¹⁴⁴ Therefore, the values given in Table 8 are to be understood as averages over the whole temperature range for the given material. Indeed, when a more sophisticated method was used to determine isosteric enthalpy of adsorption, the double-Langmuir fitted results shown in Figure 64, a similar temperature dependence of the enthalpy was calculated between all materials: 2-4 J mol⁻¹ K⁻¹. It is important to note that this analysis method works best on data sets with numerous isotherms in a close temperature range, preferably spaced by 10-20 K. The three temperatures collected in this study were much further apart, and the fits were difficult to optimize; the data plotted in a narrow range for each temperature (as in Figure 64) was the best representation of the dependence of enthalpy with uptake.

The hydrogen uptake character in ZTCs at 77 K, especially ZTC-3, is slightly different from MSC-30 because the uptake is lower between 0-1.0 MPa, but exceeds MSC-30 between 1.0-2.4 MPa. For effective hydrogen delivery by a sorbent material between two finite pressures, $P_f - P_i$, it is favorable to have an excess uptake slope that is gradual below P_f and steep in the cycled region of uptake/delivery; the quantity of hydrogen delivered is the difference between the amount in the initial (fully charged) state at P_i and the final (considered “empty”) state at P_f . For delivery to a fuel cell, P_f is often taken to be 0.3 MPa.¹⁴⁶ Therefore, ZTCs used for this purpose at 77 K exhibit higher hydrogen delivery than MSC-30 by 15% when cycled between 0.3-2.4 MPa.

Conclusions on ZTC's

Equilibrium hydrogen uptake capacities of ZTCs at room temperature are among the highest of known physisorbent materials due to their large specific surface area. Hydrogen adsorption capacity in ZTCs is approximately proportional to surface area at 298 K between 0-30 MPa, and is consistent with a large variety of carbonaceous materials, including activated carbons, carbon fibers, graphite, aerogels, and nanotubes. That is, a “Chahine’s rule” type of trend is observed at room temperature and fixed pressure for carbon-based materials, including ZTCs. This trend is found to be 2.3 mmol g⁻¹ (0.46 wt%) excess hydrogen uptake per 1000 m² g⁻¹ BET surface area at 298K and 30 MPa. ZTCs were found to have an isoexcess enthalpy of adsorption comparable to MSC-30 when measured between 77-298 K: 6.5 kJ mol⁻¹ in the Henry’s law limit. This implies that there are no significant differences in the dispersion forces responsible for hydrogen physisorption in ZTCs compared to MSC-30. Unlike other carbons, ZTCs were measured to have significantly lower skeletal density; this has the effect of increasing calculated uptake and straightening the uptake curve with increasing pressure. This is beneficial for gravimetric hydrogen delivery by ZTCs during cycling between two finite pressures in an engineering application, especially at 77 K.

¹⁴⁴ F. O. Mertens, 'Determination of absolute adsorption in highly ordered porous media', *Surf. Sci.*, **603**, 1979-1984 (2009).

¹⁴⁵ J. M. Obrecht, R. J. Wild, M. Antezza, L. P. Pitaevskii, S. Stringari, and E. A. Cornell, 'Measurement of the temperature dependence of the Casimir-Polder force', *Phys. Rev. Lett.*, **98**, 063201 (2007).

¹⁴⁶ J. Purewal, D. Liu, A. Sudik, M. Veenstra, J. Yang, S. Maurer, U. Müller, and D. J. Siegel, 'Improved hydrogen storage and thermal conductivity in high-density MOF-5 composites', *J. Phys. Chem. C*, **116**, 20199-20212 (2012).

Project Summary

The work at Caltech has concentrated in developing and evaluating materials necessary to fulfill the engineering requirements of a sorbent tank that are best served by an adiabatic system with thermodynamic properties that minimize the level of insulation required for a tank that operates at lower than ambient temperatures. To this end, our initial efforts evaluated the necessary physico-chemical properties of ideal sorbents and then progressed to synthesizing and/or coordinating the development of high surface area materials. At the onset of the Program, there was in fact no general consensus on the part of the PI's that were a part of the Sorbent Center of the required properties. While the goal of producing a high surface area material with a high constant heat of adsorption partially fulfills engineering requirements, there is to this day confusion as to how best to satisfy the initial criteria set by DOE. Moreover, it now appears that the sensitivity to volumetric density is the most critical property that needs to be addressed.

During the course of the Center activity, we encouraged the use of, not a single value for defining the heat of adsorption is often reported (termed the differential enthalpy of adsorption at zero coverage, or the "Henry's Law" value), but to instead report on the entire isosteric enthalpy of adsorption. The differential enthalpy of adsorption at zero coverage is often used as a metric in evaluating the utility of sorbents, however, the use of this quantity is problematic as virtually all adsorbents have high initial values of differential enthalpy. Because these initially high values decay as a function of loading, the engineering requirements of a tank are then complicated by requiring both pressure and temperature excursions in order to operate with such a sorbent. The isosteric enthalpy of adsorption, which plots the sorption enthalpy as a function of hydrogen loading is the value of relevance to an engineering design, as it gives an indication of the behavior of a sorbent material as hydrogen is added or released from a tank. This data is especially valuable to report as the nature of the surface excess isotherm with a high initial adsorption enthalpy, results in a sharp uptake below pressures of the 3 bar delivery requirement for a fuel cell. Under most conditions at low temperature, given a high sorption enthalpy, much of the hydrogen that has adsorbed, will be retained by the sorbent unless added heat is used to desorb this bound hydrogen. If a reasonably constant isosteric heat of adsorption is possible for a hydrogen sorbent then, higher-than-77K storage is possible, without the need for tank heating schemes that would complicate the engineering design requirements. Through our work on intercalated graphites, we were in fact able to determine that the maximum uptake values obtained at low temperature could be attained at much higher temperatures (at higher pressures), validating the goal we set of identifying a high constant isosteric heat as a property of relevance.

Systems Investigated:

Over the course of our five-year effort, we investigated a number of adsorbent systems based on our own syntheses and the syntheses of HSCoE member partners. The more compelling systems that we investigated are as follows:

- High surface area carbon aerogels synthesized by LLNL.
- Carbon nanohorns synthesized by ORNL.
- Microporous commercial carbons including ACF1603-10, ACF1603-20 and CNS-201.
- An AX-21 type, high surface area carbon MSC-30 from Kansai Coke and Chemical Co.

- MOF-177 synthesized at Caltech.
- MOF-74 synthesized at Caltech.
- Stage 2 graphites intercalated with K, Rb and Cs synthesized at Caltech.
- PEEK based microporous carbon synthesized at Duke University.
- N, B and P substituted graphitic carbons synthesized at Rice University.
- Pt doped MSC-30 synthesized at Caltech.

Analyses Performed:

In addition to our synthesis capabilities at Caltech we were able to employ a number of characterization tools in order to identify the extent to which we were able to produce successfully, the materials of interest, and the extent to which these materials could take up or release hydrogen. These analyses included:

- Sieverts equilibrium and kinetics analyses for hydrogen uptake and desorption assessment. Moreover, we performed thermodynamic analyses of the differential enthalpy of adsorption at zero coverage and isosteric enthalpy of adsorption analyses using temperatures of 77, 87, 198 and 298K.
- Transmission electron microscopy for microstructural and phase distribution determination.
- BET surface area analysis performed on campus using a Micromeritics ASAP2000.
- X-ray diffraction for crystallographic and phase formation analysis.

Bibliography: Papers acknowledging the HSCoE:

Z. Jin, Z. Sun, L. Simpson, K. O'Neill, P. Parilla, Y. Li, N. Stadie, C. Ahn, C. Kittrell, J. Tour, "Solution-Phase Synthesis of Heteroatom-Substituted Carbon Scaffolds for Hydrogen Storage," *JACS* 2010, accepted for publication.

T. P. McNicholas, A. M. Wang, K. O'Neill, R. J. Anderson, N. P. Stadie, A. Kleinhammes, P. Parilla, L. Simpson, C. C. Ahn, Y. Q. Wang, Y. Wu, and J. Liu. "H₂ storage in microporous carbons from PEEK precursors," *J. Phys. Chem. C*, 114(32): 13902–13908, Aug 2010.

N. P. Stadie, J. J. Purewal, C. C. Ahn, and B. Fultz, "Measurements of Hydrogen Spillover in Platinum Doped Superactivated Carbon," *Langmuir* 2010, DOI: 10.1021/la9046758.

J. J. Purewal, H. Kabbour, J. J. Vajo, C. C. Ahn, and B. Fultz. "Pore size distribution and supercritical hydrogen adsorption in activated carbon fibers," *Nanotechnology*, 20(20), May 20 2009.

J. J. Purewal, J. B. Keith, C. C. Ahn, B. Fultz, C. M. Brown, and M. Tyagi, "Adsorption and melting of hydrogen in potassium-intercalated graphite," *Physical Review B*, 79(5), Feb 2009.

Y. Liu, H. Kabbour, C. M. Brown, D. A. Neumann, and C. C. Ahn. "Increasing the density of

adsorbed hydrogen with coordinatively unsaturated metal centers in metal-organic frameworks". *Langmuir*, 24(9):4772–4777, May 6 2008.

H. Kabbour, T. F. Baumann, J. H. Satcher, A. Saulnier, and C. C. Ahn. "Toward new candidates for hydrogen storage: High-surface-area carbon aerogels". *Chemistry of Materials*, 18(26):6085–6087, Dec 2006.

Ph.D. Theses supported through the HSCoE:

Justin Purewal, "Hydrogen Adsorption by Alkali Metal Graphite Intercalation Compounds," Ph.D. Thesis, California Institute of Technology, 2010.

Nicholas Stadie, "Synthesis and Thermodynamic Studies of Physisorptive Energy Storage Materials, Ph.D. Thesis, California Institute of Technology, 2012.

Invited oral presentations acknowledging HSCoE support:

American Physical Society, "*Vehicular Hydrogen Storage with ad(ab)sorbent Materials*," APS Energy Workshop, March Meeting 2009, Pittsburgh, PA.

International Symposium on Hydrogen Energy, "Henry's Law and Isosteric Heats," Richmond, VA 2007.

MH2006, "H₂ Physisorption in Carbons and Metal Organic Frameworks," 2006, Maui, Hawaii.

American Physical Society, "Hydrogen cryo-adsorption; comparing low pressure and isosteric heats," March Meeting 2006, Baltimore, Md.

Postdoctoral Support:

Houria Kabbour, now at CNRS Lille.

Graduate student support:

Nicholas Stadie, 2007 – 2010, now at EMPA, Switzerland.

Justin Purewal, 2006 – 2010, now at HRL Laboratories

Angelique Saulnier, 2005 – 2006.

Undergraduate support via HSCoE:

Jenny Wang, 2009, "Supercritical Activation of Cu-BTC and MIL-101," Summer Undergraduate Research Fellowship report 2009, now pursuing a Ph.D. at MIT

Willa Freedman, 2010, "Impact of Synthesis and Processing on the Hydrogen Storage Properties of Metal Organic Frameworks and Zeolite-Templated Carbons," Summer Undergraduate Research Fellowship report 2010.